Stony Brook University

Nonlinear and Nonstationary Data Analysis of the Renal Autoregulatory Dynamics in Normotensive and Hypertensive Rats

A Dissertation Presented

by

Kin Lung Siu

to

The Graduate School

in Partial Fulfillment of the

Requirements

for the Degree of

Doctor of Philosophy

in

Biomedical Engineering

Stony Brook University

May 2009

Stony Brook University

The Graduate School

Kin Lung Siu

We, the dissertation committee for the above candidate for the

Doctor of Philosophy degree,

Hereby recommend acceptance of this dissertation.

Dr. Ki H. Chon, Department of Biomedical Engineering, Dissertation Advisor

Dr. Leon C. Moore, Department of Physiology and Biophysics, Committee Chair

Dr. Emilia Entcheva, Department of Physiology and Biophysics

Dr. William A. Cupples, Department of Biology, University of Victoria, Outside Member

This dissertation is accepted by the Graduate School

Lawrence Martin
Dean of the Graduate School

Abstract of the Dissertation

Nonlinear and Nonstationary Data Analysis of the Renal Autoregulatory Dynamics in Normotensive and Hypertensive Rats

By

Kin Lung Siu

Doctor of Philosophy

in

Biomedical Engineering

Stony Brook University

2009

Physiological systems are inherently nonlinear and nonstationary. Traditional analysis techniques that assume linearity and stationarity in the data may miss subtle transitional dynamic characteristics of the signal. This dissertation seeks to develop novel analysis techniques that explore the nonlinear and nonstationary characteristics of physiological signals. Specifically, these algorithms will be used to discern and quantify differences in dynamics of the renal autoregulatory (RA) mechanisms from normotensive and hypertensive rats. This work is separated into four specific aims. The first aim seeks to distinguish if the higher degree of variability in renal blood flow in hypertensive rats is due to deterministic chaos (DC) or time-varying characteristics of renal autoregulation. The results show that the Lyapunov exponent, which is used to quantify the degree of DC, can give erroneous results when the analyzed system has time-varying dynamics. To overcome this limitation, an algorithm was developed to specifically detect switching dynamics in RA. The second aim seeks to detect intra- and inter-nephron coupling via the auto- and cross-bispectra. The results show that nonlinear interactions in the form of phase coupling are in general less pronounced in hypertensive animals. The third aim seeks to detect very low frequency oscillations (~0.01 Hz) in the form of amplitude modulation of renal autoregulatory mechanisms. The results show that amplitude modulation is reduced in hypertensive animals and also animals anesthetized with Inactin. The fourth aim seeks to develop and test a blood pressure control system based

on the proportional-integral design. The main impetus for this aim stems from the observation from the third aim that anesthetics exert a depressive effect on RA. Therefore, this aim seeks to develop a control system to induce step changes in blood pressure to determine the step response from the kidney. In summary, various algorithms developed in this dissertation work were able to show nonlinear and nonstationary characteristics in RA not seen or misinterpreted from previous time-invariant studies. The algorithms presented are general algorithms and therefore can be applied to other physiological systems.

DEDICATIONS

This work is dedicated to God, who has taken great care of me my whole life, even when I denied him.

Table of Contents

List of Figures

List of Tables

Acknowledgements

I would like to first thank my advisor, Dr. Ki H. Chon, for everything he has done for me. Thank you for giving me a chance so long ago when I first came to this lab. You have given me the best guidance that any student can hope for and have taught me more than I can mention. I have nothing but the highest respect for you as a mentor, as a scientist, and as a person. I feel truly honored and blessed to have had the chance to work for you.

I would also like to thank my committee chair, Dr. Leon C. Moore. Thank you for always taking your time to give me guidance and advice. You have helped me in my research so much that I often call you my unofficial second advisor.

To my outside committee member, Dr. William A. Cupples, thank you coming all this way to help me. I want to also thank you for all the conversations we have had through the years, as they have been immensely helpful for me.

To my committee member, Dr. Emilia Entcheva, thank you for taking your taking time out of your busy schedule to help me. I still remember taking your class when I was an undergraduate, and it has helped me greatly in letting my interest in research grow.

To the animal queen of Stony Brook, Aija Birzgalis, thank you so much for all your help through the years. You taught me everything that I know about doing animal research. I will never forget all the times we spent working together. You have also taught me how to not only work hard, but to have fun while doing it. I can not thank you enough and I will truly miss all of our time together.

To my lab mates, both past and present: Biin Sung, thank you for putting up with me for all these years. I know that sometimes I can be hard to work with, but you still showed patience. We worked so closely together than sometimes I still see you as my student. Thank you for always helping me when I need it and I will always keep you in my prayers. Shishir Dash, thank you for all the intellectual conversations we had. I respect you for your brilliance in research as well as not being afraid to argue your ideas, even to your boss. I hope that you keep up your enthusiasm for your work and never be afraid to express your ideas to anyone. Dr. Xinnian Chen, you have already graduated, but I still want to thank you for all the help you have given me while you were here.

Thank you for always being a good friend to me and helping me see how bright life can be. Bufan Yang, it has been great to know you. You always manage to make any lab gather much more fun. Yan Bai, we have not interacted much, but I still want to thank you for being there for me. To all the lab mates in the past: He Zhao, Yuru Zhong, Hengliang Wang, Sheng Lu and Lei Feng, it was a pleasure to work with all of you.

I also thank my family members, parents Chee Keung Siu and Wai Kum Lam, and my sister Ann Kim Siu. Thank you so much for all of your unconditional support all these years. I could never have made it this far without you all.

Finally, I want to thank my wife HyunHye Chun. Thank you for always being there to brighten up my day. I could not be happier knowing that we will be spending our life together. Thank you for all the love that you have given me.

The text of this dissertation in part is a reprint of the materials as it appears in *IEEE Trans Biomed Eng* 55: 1512-1520, 2008. The co-authors listed in the publication directed and supervised the research that forms the basis for this dissertation. Permission has been grated for the use of this material in the form of letters.

Chapter 1
Introduction

1.1 Overview and significance of the kidney

The kidney is a major organ of homeostasis in the body. Some of its major functions are the maintenance of body fluid volume, release of hormones, and the filtration of metabolic wastes (110). While the heart is often associated with the short term control of systemic blood pressure (SBP), it is the kidney that is ultimately responsible for the level of SBP in the long term (110). Therefore, kidney function is extremely important in dysfunctions of the SBP, such as in hypertension. Many studies show that hypertension can lead to kidney damage (107, 132). But conversely, kidney damage can also lead to hypertension (1). Taken together, this means that having either one of these conditions will lead to the other in a positive feedback cycle that can ultimately lead to kidney failure (20, 73, 132). With hypertension being one of the most prevalent diseases in this nation, with an estimated 29% of adults in the United State in 2006 (91), the complete understanding of the mechanisms that underlie this damage is of the extreme importance.

1.2 Renal autoregulation

1.2.1 Overview and significance

The functional unit of the kidney is the nephron. Blood flow into the kidney eventually gets diverted down into approximately 3 million different nephrons in the adult human kidney. Blood flow into the each nephron enters via the glomerulus, where fluid then enters the various tubules and gets either reabsorbed back into the blood or exits the tubules and forms urine. The rate of fluid entry into the tubules, the glomerular filtration rate (GFR), is one way that the kidney can control the fluid and ion balance in the body, as an increase in GFR will lead to an increase in urine production and the decrease in ions and fluid in the body. In the absence of any regulation mechanisms, GFR

will be proportional to incoming renal blood flow (RBF). This would make fluid balance in the body essentially impossible as SBP inherently fluctuates on large time scales (8). However, experimental evidence shows that RBF remains relatively constant under different perfusion pressures (2, 43). Further, this phenomenon has been observed in isolated nephrons (15, 18, 97), which suggests that this regulation is accomplished independent of extra-renal control. This mechanism of stabilization of the RBF has been terms renal autoregulation (RA). Many past studies have shown that the site of RA is at the level of the afferent arterioles (15, 18, 37, 39, 55, 97, 119), and to a lesser degree at some upstream segments (42). This location allows the regulation of both the RBF and the GFR to be in parallel (109), as the site of activity lies upstream to the glomerular capillary bed.

Besides the important role of regulating GFR for proper fluid and ion balance, RA has also been associated with the role of protecting the microvasculature in the kidney (6, 7, 72). This stems from the observation that systemic hypertension has been linked to glomerular injury (10, 11, 35, 124). Further, studies show that impaired RA has been linked to the progression of hypertensive renal diseases (10, 11, 52, 66, 120, 124). Taken together, this suggests that RA is essential in the maintenance of physical health of the kidney.

1.2.2 Tubuloglomerular feedback

Traditionally, RA has been thought to be mediated by at least two mechanisms. The first mechanism is the slower tubuloglomerular feedback (TGF) mechanism (25, 139). This mechanism is unique to the kidney and is thought to be accomplished by a chloride ion sensor at the macular densa in the early distal tubule (13, 67, 105), which then signals for a change in conductance in the afferent arteriole. This action is possible due to the close physical proximity of the macula densa to its own arterioles (38, 123), allowing signaling to occur due to the small distance. This mechanism works on the principle that since salt reabsorption at the ascending loop of Henle is dependent on the rate of tubular flow, changes in the distal tubular ion concentration will generally indicate changes in tubular flow. Hence, raises in ion concentration at the level of the macula

densa will signal for vasoconstriction, which will ultimately restore filtration and renal function to steady levels.

Mechanistically, the general consensus is that the initial NaCl detection at the macula densa is via the furosemide-sensitive Na^+-K^+-$2Cl^-$ cotransporter (16, 32, 81, 100, 135), which then releases ATP from the macula densa cells (67, 103). At the present, there are two competing hypotheses to the exact mechanism of how ATP induces vascular changes in the preglomerular vascular bed. One line of evidence suggests that the released ATP gets converted into adenosine, which then in activates the A_1 receptors from the P1 family of purinoceptors on the afferent arteriole to induce vasoconstriction (90, 122, 125, 126). The second hypothesis suggests that the released ATP directly stimulates the autoregulatory response via activation of the ATP specific P2X1 receptors on the afferent arteriole (50, 51, 74). Further research is necessary to resolve this debate to the signaling mechanism of the TGF.

The kinetic properties of the TGF system are dependent upon many factors, such as the movement of fluid via the loop of Henle to the macula densa and the transduction of the signal from the macula densa to the proglomerular vasculature. Experimentally, the TGF response has a response time of ~30 seconds and takes ~40-60 seconds to completion in rats (30, 46). Due to the relatively long delays and slow response times, limit cycle oscillations , from 0.02 to 0.05 Hz, are observed in experimental data (9, 28, 69, 94). Experimental evidence has shown that TGF accounts for roughly 20-50% of autoregulation under normal conditions (25, 29, 57, 58).

1.2.3 Myogenic response

The second traditional mechanism of RA is the faster myogenic MYO response. This mechanism is the response of the vascular smooth muscle in response to changes to wall tension elicited by changes in transmural pressure (31, 54, 55, 83). Studies using the *in vitro* hydronephrotic kidney model (27, 39), which essentially lacks any tubules and therefore TGF, shows constriction of the afferent arterioles from changing pressure. Further, in isolated afferent arterioles (55) or in preparations where tubular flow is interrupted (127), a clear response of the vessel was observed in response to changes in

pressure. This suggests a mechanism separate from the TGF, and is contained in the vascular portions of the kidney.

Mechanistically, the membrane potential of the vascular smooth muscle cells of the afferent arteriole undergoes depolarization after an initial transmural pressure increase (36, 71). The nature of the initiation of the depolarization is as of yet unclear. Possible candidates include mechanosensitive ion channels and stretch induced activation of phospholipase C (56). What is clear is that following the initial depolarization, L-type calcium channels are activated (71), leading to an influx of calcium into the smooth muscle cells. This influx of calcium will ultimately initiate a series of intracellular events that ultimately lead to activation of myosin light chain kinase for contraction or myosin light chain phosphatase for relaxation (113). Due to the difference in the mechanisms for contraction and relaxation, the dynamics properties of the two are different in that the delay to contraction is much faster at ~0.3 second than dilation, which was shown to be at ~1 second (70). Complete response times are typically less than 10 seconds (70, 127). Frequency domain methods have further shown a resonate peak in the 0.1 to 0.2 Hz range (21, 75).

1.2.4 Third mechanism

Recently, there has been experimental evidence supporting the presence of a third component to RA (57, 58, 60). The reported contribution from this mechanism under normal conditions is relatively low at less than 12 percent (57). The original observation of the third mechanism was made using step response experiments, which induces a rapid step increase in arterial pressure to the kidney. This type of experiment takes advantage of the fact that the different RA mechanisms have varying response times. Therefore, sudden change in pressure will elicit changes in the renal vascular resistance (RVR) first in the faster MYO response, followed by the slower TGF response. In a study by Just et al. (63), the investigators observed that a very slow, third change in RVR occurred start at ~50 seconds and completing in 2 minutes in rats. In subsequent studies, similar experiments were carried out while inhibiting TGF either pharmacologically or via genetically manipulated animals to show that in the absence of the TGF response, a

mechanism other than the MYO participates in the total RA response (59). Taken together, these results suggest a third, very slow component that participates in the renal autoregulation of blood flow.

The existence of this third mechanism of RA has been of some debate. A previous study using measurements at the level of the juxtamedullary afferent arterioles failed to show any slow compensation from step changes in perfusion pressure (127). Further, previous experiments utilizing broadband blood pressure perturbations failed to reveal any such low frequency components (75, 76).

Experimental evidence for the mechanistic explanation of the punitive third mechanism has so far been scarce and sometimes conflicting. Experimental evidence suggests that this third mechanism was resistant to conditions that traditionally affect the other RA mechanisms, such as inhibition of nitric oxide synthase and angiotensin converting enzyme, as well as decapsulation of the kidney (60). In contrast, another study shows that angiotensin II receptor inhibition was able to abolish a slow component in RA (25). It is unclear at the moment the reason for the conflicting results. A recent study using genetic A1 adenosine receptor knockout mice, which has been shown to lack a TGF response, shows that this third mechanism is independent of the A1 adenosine receptor and is sensitive to furosemide (59).

1.2.5 Interactions

Given that the goal and the ultimate effecter, the afferent arteriole, of the two traditional forms of RA are the same, it is not surprising that constructive interactions exist between the two mechanisms. If the two mechanisms did not interact, destructive interference such as phase cancellations could occur to decrease the overall efficiency of RA. An elegant study by Schnermann and Briggs (101) using single nephon pressure measurements showed that TGF response was dependent on renal perfusion pressure despite interruption to the proximal tubule, which would essentially eliminate the ability for the TGF to sense changes in renal perfusion pressure. This result strongly suggests that the TGF must interact with the MYO in some way other than via tubular pressure to coordinate their activity. Later experiments using various analysis techniques have all

pointed to the interactions between the two traditional RA mechanisms (23, 78, 139). Interactions of RA are not limited to a single nephron, but have been shown to extend to other closely related nephrons. Studies have shown that the activation of the TGF in one nephron will cause a smaller response in an adjacent nephron (19, 64). Adjacent in this case refers to nephrons that share a common cortical radial artery. Further, it has been shown that the TGF and MYO synchronize with each other in adjacent nephrons (118).

At the moment, the physiological cause for the interactions remains unclear. One hypothesis suggests a mechanical cause, where activation of one mechanism induces changes in pressure in an upstream portion of the vasculature, where it would induce a stronger response (85). Another study suggests that this interaction stems from the propagation of depolarization of vascular smooth muscle cells initiated by the TGF (80).

1.3 Analysis techniques

Traditional analysis of RA generally makes use of time domain or linear, time-invariant frequency domain analysis techniques. Although these techniques have been able to give a great wealth of information about the characteristics of RA, it should be noted that the RA is neither time-invariant nor linear. Therefore, using traditional analysis techniques may miss the more subtle but important information that exists in experimental data.

More recent studies have recognized the limitations of the traditional methods and have utilized methods than accounts for the nonlinear or time-variance in RA. For example, the use of time varying spectra (129) and time varying transfer functions (24) have given insight into the non-stationary properties of RA. Nonlinear characteristics have also been shown to exist in RA, such as phase coupling (22, 23), frequency locking (118), amplitude modulation (79, 131), and transition to chaos (137). Although much work has begun on characterizing these nonlinear and non-stationary properties of RA, much work still remains for the complete elucidation of the underlying dynamics of RA.

1.4 Importance and scope of the work presented

Given the aforementioned limitations to the traditional analysis techniques, one of the overall aims of this work was to develop and use sophisticated mathematical techniques to specifically characterize the non-linear and time-variance of the renal autoregulatory mechanisms. Further, it is recognized that anesthetics in general depresses many physiological functions, including RA. Therefore, another aim of this study was to develop methods that can help assess the true nature of RA without the influence of anesthetics. The results from this work will help lay the groundwork for the proper characterization of the true dynamics and behavior of the RA system, which would help give new insight into many disorders, such as hypertensive nephropathy. Further, the methods presented in this work are mostly general methods than can be applied to other systems. Therefore, this work can also help other researchers in different fields, as the properties of non-linearity and time-variance are present in other physiological systems.

Chapter 2

Distinguishing between time variance and deterministic chaos in tubuloglomerular feedback

2.1 Abstract

Past studies have shown that the tubuloglomerular feedback (TGF) of spontaneously hypertensive rats (SHR) have positive maximal Lyapunov exponent (MLE) values, which suggests that it has properties consistent with deterministic chaos. However, calculation of the MLE from normotensive Sprague-Dawley rats (SDR) also shows a positive number, even though the normotensive animals have relatively regular oscillations when compared with SHRs. Therefore, this study seeks to examine whether the general MLE value may be erroneous under the condition of time-variance. Computer simulations using the logistics map shows that when time variance is introduced into the model, the estimated MLE value is larger than when the model was without time variance. Due to this limitation of the MLE, a new algorithm is introduced specifically designed to quantify the frequency mode switching of the TGF. This algorithm was used on single nephron flow data from SHR (n=18) and SDR (n=15) animals. The results show that both the SDR and SHR had statistically significant lower frequency oscillation modes and frequency switching events than the logistics map, as well as being different from each other. The difference between the results from the MLE calculation and the present algorithm is likely due to the time variance that is present in both SDR and SHR. The results suggest that results from the MLE should be carefully interpreted as time variance, which is often present in physiological data, can lead to erroneous results.

2.2 Introduction

Renal blood flow (RBF) remains relatively stable despite changes in systemic blood pressure due to the phenomenon of renal autoregulation. Traditionally, renal autoregulation is thought to be mediated by at least two mechanisms, the slower

tubuloglomerular feedback (TGF) and the faster myogenic (MYO) mechanisms. The TGF operates on a time scale of 20 – 50 seconds (47) and has been shown to be mediated by flow rate dependent concentration changes of the chloride ion at the macula densa (67, 105). The MYO operates on a time scale of 3 – 10 seconds (70) and is thought to be mediated by sensing wall tension changes in the afferent arteriole (31, 54, 55). These two mechanisms have been shown in the past to interact and coordinate their activity to maximize the efficiency to bring RBF to homeostatic levels (23, 78, 101). Recent studies have also shown the possibility of the existence of a third mechanism, which operates on a longer time scale than the traditional mechanisms (57, 60).

Computational analyses of past experimental studies have shown that spontaneously hypertensive rats (SHR) have weaker and broader spectral peaks at the TGF frequency range than normotensive animals (44, 137). Further, the time records of hypertensive animals are more unpredictable and have more irregular oscillations than normotensive animals and have a positive Lyapunov exponent value (137). The Lyapunov exponent estimates the sensitivity of the data to initial conditions, which is the hallmark of deterministic chaos. However, previous studies have shown that the RBF of SHR is highly time varying (95). Given that the Lyapunov exponent value is essentially time invariant, using such a method on time varying data may lead to erroneous results.

The purpose of this study was therefore to revisit the use of the Lyapunov exponent in the study of RBF signals. Computer simulations were used to show that time variance will lead to erroneous values of the Lyapunov exponent, which suggests that the positive Lyapunov exponent present in the SHR may be erroneous. To resolve this issue, a new algorithm specifically designed based on frequency mode switching of the TGF was developed and used on single nephron flow data to assess the complexity of the renal autoregulation system. Computer simulations were used to assess the efficacy of the algorithm. The results show that both the SDR and SHR have lower number of TGF frequency switching and modes than low order deterministic models.

2.3 Methods

2.3.1 Animal preparation

All experimental protocols were approved by the Institutional Animal Care and use Committee at the State University of New York at Stony Brook and The University of South Florida. The data were collected from a previous study (19) and therefore the surgical techniques will only be briefly described. Single nephron stop flow pressure recordings were measured from Sprague-Dawley (SDR, 240-300g, n=15) and spontaneously hypertensive rats (SHR, 12 wk old, n=18). The anesthesia state was achieved using halothane, administered via an oxygen-nitrogen mixture and ventilated artificially after the administration of a muscle relaxant. Tubular pressure was measured using a 1 to 3 um diameter micropipette attached to a servo-nulling pressure circuit inserted into a section of the proximal tubule. Data were recorded on a TEAC R-61 4 channel cassette data recorder for off-line analysis. The data were replayed and sampled digitally at 4 Hz after electronic low-pass filtering at 1.5 Hz.

2.3.2 Deterministic chaos models - Logistic map

The logistic map is a simple non-linear dynamic equation that is often used to show chaotic behavior, described as:

$$x_{n+1} = r x_n (1 - x_n) \qquad \text{(eq. 2.1)}$$

where the parameter r determines the behavior of the system. Generally, when r is greater than 3.57, the system has characteristics of deterministic chaos.

2.3.3 Maximal Lyapunov exponent (MLE) calculation

The MLE is used to quantify deterministic chaos. A positive MLE is an indication of a chaotic system. For example, non-chaotic signals will have a negative MLE while a chaotic system will have a positive MLE and the value increases with higher degree of

complexity. In this work, the calculation of the MLE was done by using the TISEAN 3.0 software package (40).

The first step in the calculation of the MLE involves estimating the time delay and embedding dimension of the time series. Time delay was estimated using the mutual information criteria of the data. The embedding dimension was estimated using the false nearest neighborhood approach. Using this information, the MLE was estimated by the algorithm originally proposed by Kantz (65).

2.3.4 Algorithm for detecting different TGF oscillation states

Collected data was further processed by down sampling to 1 Hz following an anti-alias low-pass filter, removal of linear trend, and normalizing to unit variance to facilitate comparison between data sets. The time-frequency spectrum of the data was calculated using the variable frequency complex demodulation (VFCDM) algorithm, which has been shown to provide one of the highest time-frequency resolutions (128). The frequency region for the TGF mechanism (0.02 – 0.05 Hz) was isolated from the original spectrum, and the frequency at the maximum spectrum power in the TGF frequency band was recorded across time. Switching dynamics were noted when there were large sudden changes in frequency. This was done by comparing each point by the average value of a small window of previous points, hereby term the switching window. Specifically, a switch is registered when the difference between these two values are larger than a threshold, hereby termed the switching threshold. Further, only the first of these switches are registered as a true switch. The frequency of oscillation between two switches is considered to be a preliminary oscillatory mode. This oscillatory mode was then compared with all other modes in the same time trace. If the difference between two preliminary oscillatory modes is less than a threshold, hereby termed the mode threshold, the two modes are then considered to be one unique frequency mode. The number of unique frequency modes as well as the number of true switches is recorded.

A computer generated simulation signal is used to illustrate the algorithm as shown in Fig. 2.1. The test signal is composed of two sinusoidal signals, at 0.02 and 0.04 Hz, spliced together in an alternating manner. Each segment was 200 points, with a total

of 5 segments used. The top panel of Fig. 2.1 shows this test signal. The middle panel of this figure shows the frequency tracking of the maximal power across time done within the TGF frequency range. Note that the correct frequency for each segment in the data was obtained. The bottom panel shows the detected switches from the frequency tracking in panel B. Each vertical line shows the position of a detected switch. This figure further shows the segments that are found to be similar, with similar modes shown as letters A and B. Note that the algorithm was able to correct identify 5 different segments and 2 different modes.

To determine the correct size of the aforementioned switching window, a series of computer generated signals were used. The simulated signal as shown in the top panel of Fig. 2.1 was used. This signal was then contaminated with a varying degree of additive Gaussian white noise, from 20dB to -10 dB. Window size was then varied between 10 to 70 data points. The accuracy was assessed by calculating the standard deviation between the size of the detected segments. Since all 5 segments in the data are of equal length, perfect detection will result in 0 standard deviation. 100 realizations of added Gaussian white noise were used to get an average standard deviation value to assess accuracy. The result of this simulation is shown in Fig. 2.2. Note that this plot is a 3 dimensional plot, with the third dimension of color being the value of the standard deviation. This plot shows that a switching window size greater than 60 points results in large errors. Further, low data points also results in increased error. Therefore, a switching window of 40 data points was chosen for this study as it is shown on this simulation to have the greatest efficacy against increasing noise levels.

2.3.5 Statistical analysis

The statistical software package SigmaStat (Systat Software, Inc., San Jose, CA) was used for all statistical calculation. Significance threshold was set to be alpha = 0.05. The student's t-test was used to compare between 2 groups of data. For comparing between the number of dynamic modes and frequency switches, the Mann-Whiteney rank sum test was used. For the comparison of a single experimental value to simulated data generation, the 5 and 95 percent confidence interval was calculated for the simulated

value and compared with the single experimental value. The experimental value was deemed to be significantly different from the simulations if the experimental value lies outside of the confidence interval.

2.4 Result and Discussion

The top panel of Fig. 2.3 shows two representative traces of the single nephron blood flow time traces. The top left panel shows a time trace of the SDR, while the top right panel shows the time trace of the SHR.

The maximal Lyapunov exponent was estimated to be 0.17 ± 0.02 and 0.37 ± 0.05 for SDR and SHR, respectively. These values are significantly different ($P<=0.05$). These values fit well with past studies that show positive MLE in hypertensive animals (137). While the positive MLE value for SDR is low than SHR, it is different from the previous studies as it has been suggested that RBF dynamics from SDR do not exhibit dynamics of deterministic chaos. Further, the MLE value of 0.17 for SDR is close to some of the low-dimensional deterministic chaos systems such as the logistics and the Henon maps. A possible reason for the positive MLE value for SDR may stem from the fact that time-varying nature of the signal may have led to inaccurate estimate as the LE algorithm assumes stationarity.

To further explore this possibility, a series of computer simulations involving the logistic map was used. The first simulation example examined the effect of data points on the MLE. For this simulation, the parameter r from Eq. 2.1 was chosen to be 3.62. The number of data points was varied between 100 to 5000 in steps of 10 data points. At each data point, 100 different realizations of the logistic map were generated by varying the initial condition from 0.001 to 0.1, in steps of 0.001. The mean MLE values estimated from these 100 realizations was recorded at each data length step. The result from this simulation is shown in Fig. 2.4. It is observed that at low data lengths, the MLE estimation is not accurate. At data lengths larger than ~1000 points, the value plateaus at ~0.22. This implies that 1000 data points are sufficient to accurately estimate the MLE from data.

The second simulation tests the effect of time-variance on MLE estimation. For this experiment, a series of 10 logistic maps with r of 3.62 and data length of 1000 points was spliced together. Each of the 10 logistic map segments was generated with a different initial condition. This will essentially create a logistic map with time-varying parameters. 100 different time-varying logistic maps were created by varying the initial conditions from 0.001 to 0.1 in steps of 0.001. The mean ± standard deviation for each individual segment and for the total spliced signal was 0.22 ± 0.001 and 0.43 ± 0.090, respectively. Nonstationary dynamics results in approximately doubling the actual MLE value. These results clearly show that the time invariant MLE value was not able to correctly capture the true dynamics of the spliced together logistic map signal. Therefore, the MLE values obtained from SDR and SHR are most likely to have been inflated by the inaccurate MLE algorithm for time-varying data.

Therefore, a new algorithm, as described in the methods, was specifically designed to search for switching TGF dynamics in renal autoregulation. This algorithm will generally detect switching dynamic modes in the form of changes in frequency of the dynamics. Typical results from the algorithm are shown on Fig. 2.3. Summarized results are shown on Fig. 2.5. Statistical significance ($P<=0.05$) was found between SDR and SHR for both cases. Our results show that in general, SHR have more frequency switching and more frequency modes than SDR. This is in agreement with previous studies (95, 137) where the TGF system was seen to exhibit more time-varying fluctuations across time. Of particular importance is that the number of frequency modes detected in the SHR is at most 2 or 3, despite a relatively large number of switches. This is in excellent agreement with a modeling study by Layton et al., which suggested that the irregularities seen in the TGF of SHRs were due to the SHRs switching between 2 or 3 different stable oscillatory modes (68). In contrast, the majority of the SDR records show only 1 frequency mode. This demonstrates the stability that is often observed with the TGF in SDR.

Although the number of data length was not statistically different between SDR and SHR records (1543 ± 163 and 1391 ± 82), the frequency switching phenomenon is in general data point dependent. That is, the longer the data set, the more switching would occur if all else is the same. Therefore, to more accurately compare between the

experimental data with the computer generated logistics map, we compared each experimental data record with generated logistics maps with the same data length. This comparison was made by first generating 999 generations of the logistic map with the parameter r set at 3.62 (for a MLE of 0.22) and data length equal to the original data by varying the initial condition from 0.001 to 0.999 in steps of 0.001. The frequency mode detection algorithm was used on each data set. The 5 and 95th percentile of the number of switches and modes were calculated and compared with the numbers calculated for the data. If the values obtained from data lies outside of the 5 and 95th percentile of the simulations, it is then deemed significantly different.

All 15 SDRs had significantly less switching modes than similar length logistic map. For SHRs, only 12 out of 18 SHRs had significantly less switching modes than the logistic map. These distributions were then compared using a 2 x 2 contingency table based on the Chi-squared distribution, and was found to be significantly different ($P<=0.05$). For the number of frequency modes, all 15 out of 15 SDRs had significantly less switches than similar length logistic maps, while for SHRs it was 14 out of 18. Again, using the Chi-squared distribution based a contingency table, the two distributions are found to be significantly different. It should be noted, however, that comparing the number of frequency modes using the logistics simulations may not be the most accurate. This is because the frequency threshold that differentiates two frequency modes was set at 0.01 Hz. Therefore, only a maximum of 6 different frequency modes can be possible given the scanning area of 0.01 to 0.06 Hz. With such a small range of possible modes, and adding the problem of limited data lengths, the frequency resolution becomes a concern.

The frequency mode detection algorithm shows that the SHR have in general less frequency switching events than the logistics map. This is in contrast to the results from the MLE estimation, which showed the SHR to have higher complexity than the logistic map. The difference in the results is likely due to the fact that the current frequency mode detection algorithm was designed to specifically test for the time varying frequency shifts that exists in the TGF of the SHR. The logistics map, being a model for deterministic chaos, will have relatively random shifts in frequency modes, leading to the higher calculated values from this algorithm.

Past studies have shown that the SHR has a positive MLE (137), which suggests that the SHR has properties that make it consistent with deterministic chaos. Not reported in that study was the MLE of SDRs. In this study, we confirm the positive MLE of the SHR of the previous study. Further, we calculated the MLE of the SDR to also be positive, albeit at a lower value. These positive MLE values would put the SDR and the SHR near the same order of chaotic behavior as a low order deterministic model, such as the logistics map. Since this is unlikely to be the case for the SDR, due to the highly regular TGF oscillations seen in the data, this points to some other factor that is influencing the MLE estimation. The simulations in this work suggests that one possible culprit is the time variance present in SHR.

Taken together, this study shows that the general value of the MLE must be used carefully, as time-varying events can lead to erroneous decisions about the complexity of the data. This is especially important in physiological data, as time variance has been found in many physiological systems. A recent computer modeling study of the TGF system by Layton et al. used a model built from physiological measurements in an attempt to discern the origin of these irregular TGF oscillations in SHR (68). In that work, the authors concluded that the seemingly irregular oscillations in the SHR was a result of time varying switches to different dynamic modes due to temporal variations in various TGF parameters in the SHR. This dynamic mode switching was thought to be the source of the multitude of peaks seen in the time invariant frequency spectra of the SHR. The results from the present study fit well with these modeling results, as the TGF of the SHR was shown to switch between several stable frequency modes across time.

In conclusion, this study revisits the notion that the apparent instability of the TGF in the SHR is consistent with a low order deterministic event. Using an algorithm that specifically detects frequency mode switching in the TGF frequency range, the SHR was shown to have statistically lower switching events than a low-order deterministically chaotic logistics map. This suggests that the high value of the MLE calculated for the SHR may have been due to the time variance that inherently exists in the SHR, and illustrates inadequacy of the MLE algorithms for time-varying data.

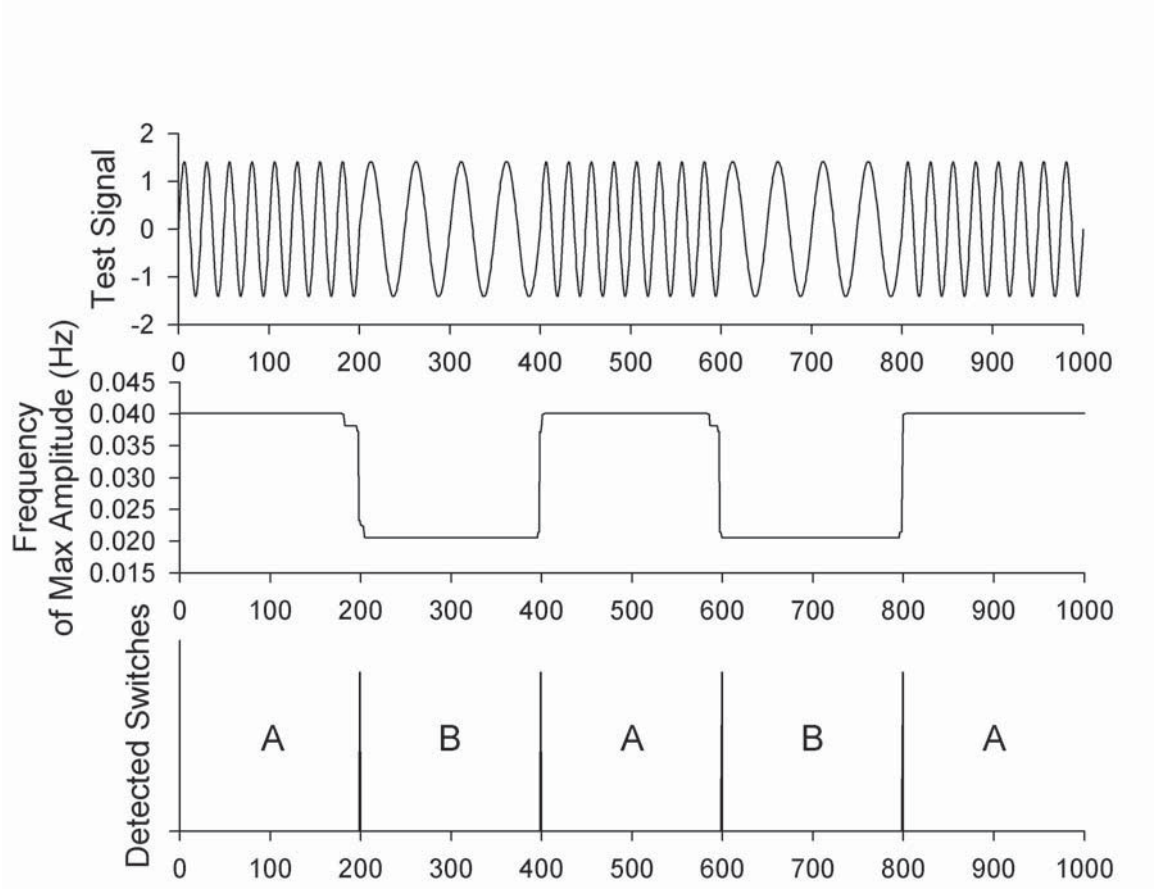

Figure 2.1 – Computer simulated example showing demonstrating the frequency mode detection algorithm. The top panel shows a test signal, which contains two frequency components of 0.04 and 0.02 Hz. The middle panel shows the frequency of the maximal amplitude in the TGF frequency band. The bottom panel shows the time points where frequency switches are detected. The figure further shows the modes that are detected to be the same, marked with the letters A and B in the bottom panel.

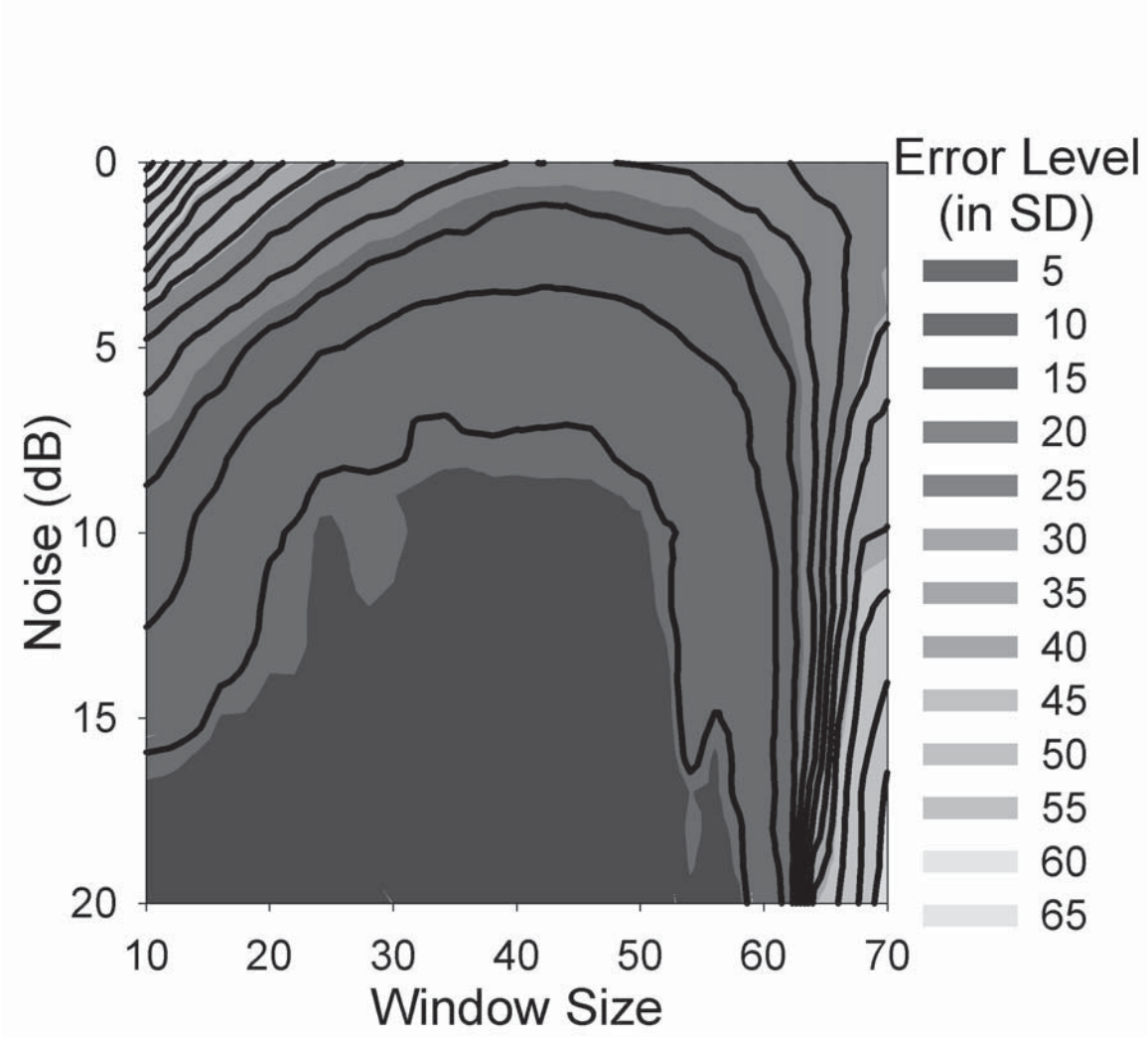

Figure 2.2 – Computer simulation to determine optimal switching window size. Varying window sizes as well as varying amount of Gaussian white noise was used in order to determine the window size that is best able to tolerate noise. The standard deviation of the detection was reported in this figure, as perfect detection should result in 0 standard deviation.

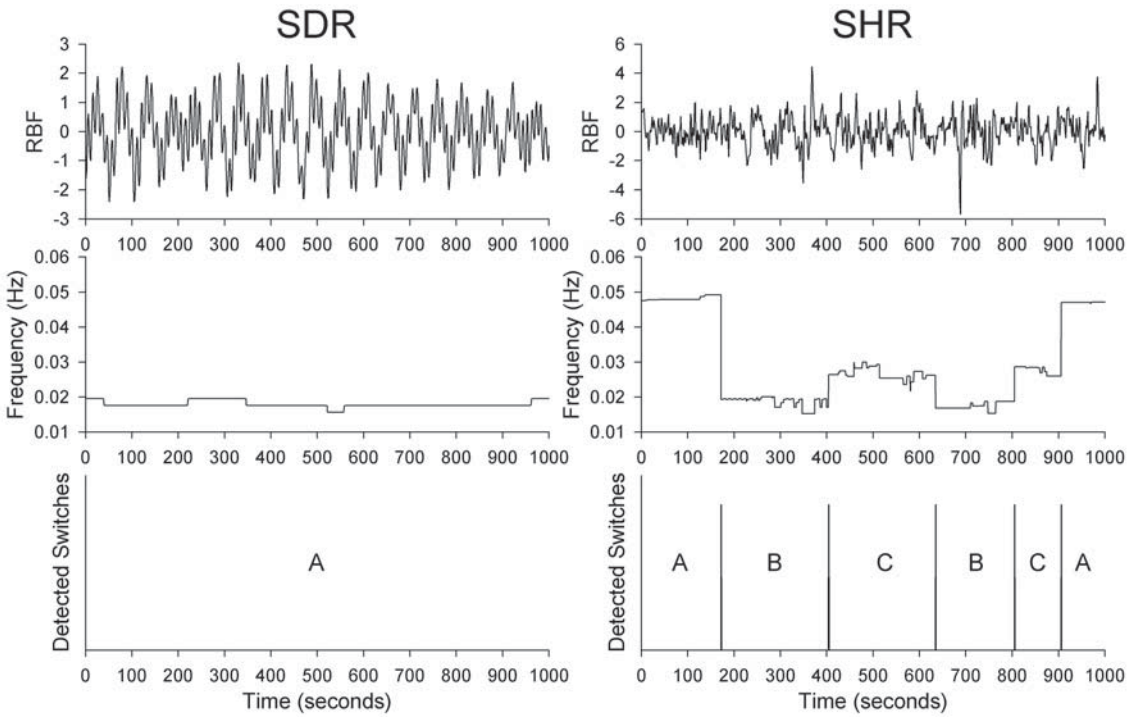

Figure 2.3 – Representative single nephron flow data from both SDR and SHR, shown on the left and right columns, respectively. The top panels show the representative time traces. The middle panels show the frequency of the maximum amplitude tracked across time. The bottom panels show the time location of the detected frequency mode switches. Further, the bottom panels shows which frequency modes are found to be similar, with similar modes indicated by the same letter.

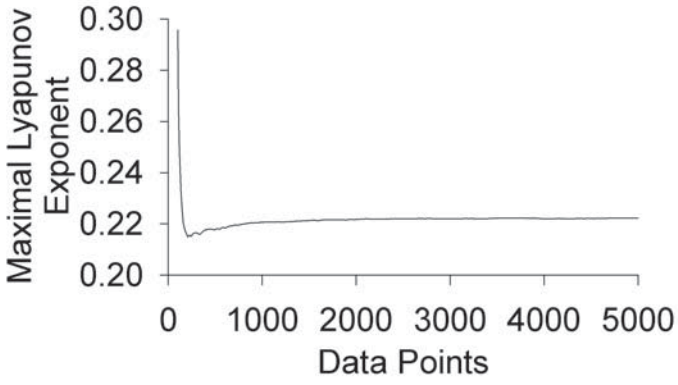

Figure 2.4 – Result of the simulation of the calculation of the maximal Lyapunov exponent (MLE) with increasing data length. The result here is shown as mean of 100 simulations of the MLE of each individual generation of the signal. Note that the curve plateaus at approximately 1000 data points.

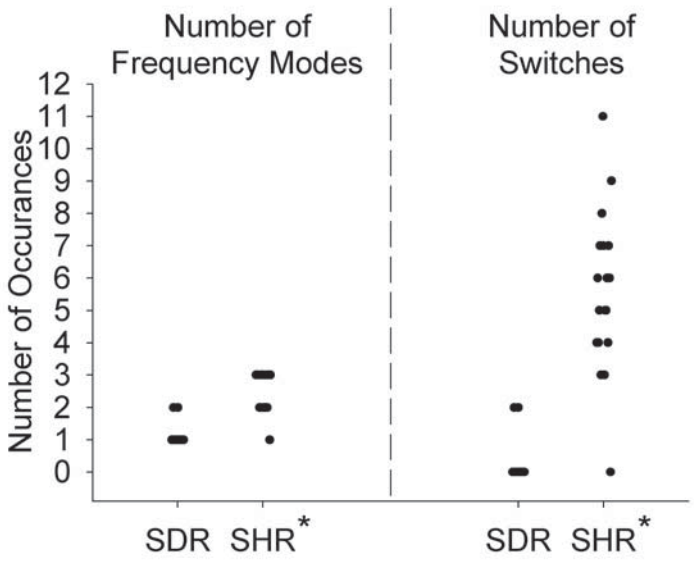

Figure 2.5 – Summary data from the frequency mode detection algorithm. Statistical significance was found between the SDR and SHR in both cases (P<=0.05, shown as "*").

Chapter 3
Statistical Approach to Quantify the Presence of Phase Coupling Using the Bispectrum

3.1 Abstract

The bispectrum is a method to detect the presence of phase coupling between different components in a signal. The traditional way to quantify phase coupling is by means of the bicoherence index, which is essentially a normalized bispectrum. The major drawback of the bicoherence index (BCI) is that determination of significant phase coupling becomes compromised with noise and low coupling strength. To overcome this limitation, a statistical approach which combines the bispectrum with a surrogate data method to determine the statistical significance of the phase coupling is introduced. This method does not rely on the use of the BCI where the normalization procedure of the BCI is the major culprit in its poor specificity. The accuracy of the proposed approach was demonstrated using simulation examples which are designed to test its robustness against noise contamination as well as varying levels of phase coupling. The results show that the proposed approach outperforms the bicoherence index in both sensitivity and specificity and provides an unbiased and statistical approach to determining the presence of quadratic phase coupling. Application of this new method to renal hemodynamic data was applied to renal stop flow pressure data obtained from normotensive (N=7) and hypertensive (N=7) rats. Significant nonlinear interactions were found in both strains of rats with a greater magnitude of coupling and smaller number of interaction peaks in normotensive rats than hypertensive rats.

3.2 INTRODUCTION

The bispectrum is a useful tool for identifying a process that is either non-Gaussian or is generated by nonlinear mechanisms. Application of the bispectrum has

been especially popular in biological systems because of the ubiquity of inherently nonlinear characteristics of biological mechanisms. One such characteristic is the presence of nonlinear interactions which have been detected in neural (48, 92, 98, 106), renal (23, 95) and cardiovascular (5, 53) systems, in particular. Detection of nonlinear interactions has been particularly useful in neural system studies because the bispectrum has been used effectively to detail changes in interactions with the level of anesthesia and sedation (96, 133, 134). Furthermore, it has been used in an attempt to detect and predict epileptic seizure events (14).

While nonlinear interactions can be identified in many forms, including phase coherence, the bispectrum is ideally suited to detecting phase coupling between two components of a process (88). The power spectrum suppresses phase relations, thus, it cannot be used for detection of phase coupling.

Quantification of phase coupling via the bispectrum is obtained by estimating the bicoherence index (BCI) which is essentially a normalized bispectrum obtained by dividing the bispectrum by the power spectra of the signal (88). The theoretical values of the BCI correspond to a range from insignificant to highly significant phase coupled peaks. Phase coupling implies both frequency and phase coupling, in which the third frequency peak and its phase are the sum of the first two frequency peaks and phases. The BCI is designed to consider only phase-coupled components, eliminating bispectral peaks resulting from frequency locking alone that should not be present in a bispectrum but are often represented. However, due to technical considerations such as using an insufficient number of segments to compute the bispectrum, frequency coupled peaks will sometimes appear in the BCI. Further, for finite-length data sets, the high variability present in the bicoherence index will cause theoretically Gaussian processes to have a non-zero value.

To avoid making erroneous decisions about the presence of phase coupling based on the BCI, a method was proposed by Elgar and Guza (33) that is based on modeling the significance level for zero bicoherence. In this work, the level of significance was based primarily on the number of segments used in the calculated bicoherence. We have recently proposed an autoregressive bispectrum combined with surrogate data method to test the statistical significance of the obtained quadratic phase coupled peaks (23). This

approach allows better detection of phase coupled peaks, even with noise contamination. While this approach, known as S-statistics, is certainly an improvement over the BCI itself, the method still suffers from low specificity due to a normalization procedure which can allow insignificant bispectral peaks to become significant. In addition, in certain instances, the BCI values are greater than one when a small amount of time-variance was introduced into the data. This further complicates the interpretation of results, as most physiological data inherently have some degree of time-variance. To compensate for this problem, Pinhas et al. (93) introduced a method that statistically removes these erroneous peaks. However, this method suffers from the fact that it is based on the central limit theorem, which requires a large amount of data which may be difficult to obtain with physiological data.

Given the aforesaid problems associated with the detection of phase coupling with the use of the BCI as well as S-statistics, the aim of the present work is to circumvent the limitations of both methods. The approach we propose does not involve the use of the BCI, rather, it uses bispectrum estimation followed by testing the significance of the results against surrogate data realizations. The goal of the surrogate data transformation is to destroy the nonlinear dynamics in the data. This leaves a time series with only linear properties; thus no phase coupling should be detected. As a result, only bispectral peaks remaining must arise from harmonic components and are insignificant. The efficacy of our new method, based on the use of the bispectrum estimation followed by the use of a surrogate data technique, will be compared to the traditional BCI as well as combination of the BCI and the S-statistics method.

3.3 Methods

3.3.1 Bispectral Analysis

There are two nonparametric approaches, direct and indirect, to compute the bispectrum. The indirect method involves computation of the third-order cumulant followed by the two-dimensional Fourier transform of the third-order cumulant. For our

analysis, we use the direct method which is estimated by taking the average of triple products of the Fourier transform over *K* segments:

$$BS(f_1, f_2) = \frac{1}{K}\sum_{k=1}^{K} X_k(f_1)X_k(f_2)X_k^*(f_1 + f_2) \qquad \text{(eq. 3.1)}$$

where $X_k(f)$ is the Fourier transform of the *k*th segment and * indicates the complex conjugate. Note that as the size of each segment decreases, the frequency resolution will also decrease. Therefore, it is important to choose the proper segment size so that there is sufficient resolution to resolve the dynamics in the signal while retaining enough segments to properly reduce variance in the bispectrum for the detection of phase coupling. This tradeoff between time and frequency resolution also pertains to the indirect method and to a lesser extent to parametric approaches. In addition, while our estimation results are all based on the direct method of computing the bispectrum, our approach of statistically quantifying the presence of phase coupling equally applies to both indirect and parametric (model based) approaches to estimating the bispectrum.

3.3.2 Necessity of Statistical Analysis in Bispectral Analysis

To illustrate the necessity of complementing bispectral estimation with statistical analysis, a simple simulation example is provided. The simulation consists of two test signals, both involving three frequencies, as shown below:

$$y_{1,2}(t) = \sin(2\pi f_1 t + \theta_1) + \sin(2\pi f_2 t + \theta_2) + A\sin(2\pi f_3 t + \theta_3) \qquad \text{(eq. 3.2)}$$

where f_1 and f_2 are set to 0.1 and 0.2 Hz, respectively. For both test signals, the third frequency, f_3, is set to f_1+f_2=0.3Hz in order to achieve the frequency coupling. Phases associated with the first two frequencies (θ_1 and θ_2) are randomly generated between $-\pi$ and π with a uniform distribution. For the first test signal ($y_1(t)$) the third frequency is also phase coupled such that $\theta_3=\theta_1+\theta_2$. The second test signal ($y_2(t)$) is not phase coupled so that θ_3 is also randomly generated to be between $-\pi$ and π. The amplitude A is set to 0.5 for the phase uncoupled signal whereas it is set to 1.5 for the phase coupled signal. The amplitude of the phase uncoupled signal is set to a high value to simulate a condition where high bispectral values can be obtained from frequency matching components alone. Both test signals were generated at 1 Hz sampling rate and contained 2048 data

points. For both test signals, 32 segments, each containing 64 data points, with no overlapping segments, were used to estimate the bispectrum.

The resulting bispectra (middle panels) and the BCI (bottom panels) for the phase coupled and uncoupled signals with their respective power spectra (top panels), are shown in the left and right panels of Fig. 3.1. The power spectra of the phase coupled and uncoupled signals are indistinguishable in terms of frequency information, albeit the amplitude of the phase coupled spectrum is lower especially at 0.3 Hz. Although the phase coupled signal has lower spectral amplitude than the phase uncoupled spectral peak, we observe a similar bispectral peak magnitude at the frequency pair (0.1, 0.2) Hz in these two systems. This example demonstrates an important issue. Due to inherent limitations associated with the bispectrum estimation, it is possible to obtain a bispectral peak for the phase uncoupled signal under certain frequency and amplitude combinations. That is, frequency coupling alone is sufficient to generate peaks in the bispectrum. Hence, a statistical method is needed to distinguish true peaks resulting from frequency and phase coupling from erroneous peaks resulting from frequency coupling alone. The bottom panel shows the bicoherence of the test signals. As shown on the bottom right panel, the BCI was able to correctly eliminate the phase uncoupled peaks as these peaks have values lower than the threshold value of 0.306 as derived by Elgar and Guza (33). However, note the inadequate frequency resolution especially on the bottom left panel as compared to the figure shown on the top left panel. In addition, this simulation is based on noise-free and relatively long data records, conditions which are seldom met with experimental data. The limitations of the BCI will be further illustrated in the Results section.

3.3.3 Traditional Statistical Methods

Traditionally, determination of phase coupled peaks in the bispectrum required the calculation of a normalized bispectrum, called the bicoherence index (BCI). The BCI is calculated by:

$$BCI(f_1, f_2) = \frac{BS(f_1, f_2)}{\sqrt{P(f_1)P(f_2)P(f_1 + f_2)}} \qquad \text{(eq. 3.3)}$$

Where *P(f)* is the power spectrum of the signal.

From the BCI, one would then need a method for determining significance in the peaks observed. The method developed by Elgar and Guza (33) for determining significance in the BCI based on describing the significance levels for zero bicoherence was used here. Specifically, it was found that the 95% significance level for zero bicoherence is approximately $\sqrt{6/2m}$,where *m* is the number of segments. Further, the S-statistical method (23), based on surrogate data, was also used here for comparison While the S-statistics method was developed for use with autoregressive model based bispectral estimation, we adopt this technique to the direct method of computing the bispectrum.

Surrogate data are a modified form of the original data which eliminates nonlinear properties while retaining linear statistical properties. Randomization of phases accomplishes the elimination of nonlinearity and since randomization can be performed in many ways, we can obtain multiple realizations of surrogate data from a single time series. This is useful in the statistical testing of nonlinearity, as one can then use the generated surrogate data as the null condition to be tested against. We chose the iteratively refined surrogate data technique (IRSDT) (133)**.** The IRSDT will destroy any nonlinearity in the signal, and has been shown to be more accurate than the amplitude adjusted Fourier transform technique (121) because it iteratively corrects for deviations in the spectrum as well as maintains the correct distribution of the signal.

The S-statistic approach involves generation of multiple realizations (~100 suffice) of surrogate data. The BCI is calculated for each realization of surrogates as well as for the original data. The S value, which tests for the 95% significance of the detected quadratic phase coupling, is based on the assumption that the distribution of the surrogates follows a normal distribution. In the current work, the threshold for S-statistics is set as the 95th percentile of the distribution of the BCI estimated on the 100 realizations of surrogate data. The threshold value is then subtracted from the BCI value of the original data.. Values above zero are considered significant for the S-statistics.

Simulation examples will be used to show that the BCI and S-statistics lack sensitivity and specificity, respectively. Due to the inherent limitations of these traditional methods, a new approach for evaluating quadratic phase coupling, based on

surrogate data of the bispectral estimate and completely bypassing the computation of the BCI, is described in the following section.

3.3.4 Proposed Approach: Surrogate Data Threshold Method Applied to the Bispectrum and not BCI

The bispectrum with surrogate (BWS) method is similar to S-statistics, being also based on surrogate data. However, a key distinction is the fact that it does not utilize BCI but only the bispectrum estimate, since its statistical determination of the presence of phase coupling uses surrogate data realizations. The procedure involves generating 100 realizations of surrogate data from the original data. The bispectrum of each of the surrogates, as well as the original data, is calculated. The mean and standard deviation of all 100 surrogates' bispectral estimates are calculated. The 95% statistical threshold values are defined as the mean plus 2 standard deviations. Note that the statistical threshold of the BWS, based on the normality assumption, is verified using the Kolmogorov-Smirnov goodness of fit test (140). Any bispectral peaks estimated from the original data that are above these threshold values are considered to have significant frequency and phase coupling. Therefore, the difference between the bispectrum value from the original data and the threshold value is then calculated. Difference values above 0 will indicate a bispectrum value above the threshold, and are therefore considered significant.

3.3.5 Simulation Conditions

The three methods, the BCI, S-statistics, and our proposed approach (BWS) were tested by using simulated data under different conditions. Unless otherwise noted, the test signal used consisted of a phased coupled triplet as described earlier, at a 1 Hz sampling rate with 2048 data points. The frequencies used were f_1=0.1, f_2=0.2, and f_3=0.3. The bispectra was also calculated as described before with segment size of 64, but 128 points were used for the FFT (64 points zero padding), and there were no overlapping segments.

To guard against counting the same bispectral peak twice (especially possible if the frequency resolution is not high), each peak was checked against its 8 nearest neighbors. If the magnitude of a peak was higher than any of its neighbors, it was then considered a peak. We repeated this process for the entire bispectrum. We then tested the peaks for significance of using the three methods.

3.3.6 Application of the BWS to Renal Blood Flow

The BWS was applied to experimental renal hemodynamic data to demonstrate its efficacy. All experiments were performed under protocols approved by The Institutional Animal Care and Use Committee at Stony Brook and The University of South Florida. The data were collected from a previous study in which stop flow pressure (SFP) recordings from a single nephron were measured in Sprague-Dawley (SDR, 240-300g, n=7) and spontaneously hypertensive rats (SHR, 12 wk old, n=7) (19). Surgical preparation and the stop flow pressure measurements are detailed in our previously published study (23), thus, will only be briefly described here. Animals were anesthetized with halothane administered in an oxygen-nitrogen mixture and artificially ventilated after the administration of a muscle relaxant. Tubular flow was interrupted with bone wax in a selected proximal tubule, and intratubular hydraulic pressure proximal to the wax block was measured via a 1 to 3 um diameter micropipette attached to a servo-nulling pressure circuit. Data was recorded on a TEAC R-61 4-channel cassette data recorder for off-line analysis. The recorded data were replayed through an electronic low-pass filter with a roll-off frequency of 1.5 Hz and sampled digitally at 4 Hz. Before bispectral analysis, the data were further filtered by a digital low-pass filter with a cut-off frequency of 0.5 Hz, and down sampled to 1 Hz.

3.4 Results and Discussion

3.4.1 Test for Normality

Our statistical threshold, based on the normality assumption, was verified using the Kolmogorov-Smirnov goodness of fit test (140). The calculated P value was > 0.05, which confirms that this set is drawn from a normally distributed population.

3.4.2 Test of Robustness Against Noise Corruption

We tested the three methods for robustness against noise corrupted data. The generated signal was corrupted by additive Gaussian white noise (AGWN) such that the signal to noise ratio (SNR) ranged from 25 to -25 dB. Ten independent realizations of Gaussian white noise at each noise level were generated to corrupt the signal in order to achieve a statistical result. The bispectrum was then calculated for each realization of the noise corrupted signal to examine how robust each method was in detecting only the true phase coupled peak. To test the sensitivity of each method, the calculated value of each method at the generated frequencies were recorded for each realization and averaged. Further, to test for specificity, the total number of significant detected peaks across the entire bispectrum was also recorded for each realization. The mean of sensitivity and the median of specificity results are reported in the top and bottom panels of Fig. 3.2, respectively. Note that for the BCI, the thresholding method proposed by Elgar and Guza was used (33), while for the S-statistics and the BWS methods, a threshold value of 0 was used as this represents the difference between the bicoherence value of the data and surrogate data results. All of these threshold values are noted as dashed lines.

As shown in the top panels of Fig. 3.2, the BCI is most susceptible to noise corruption as it needs a SNR greater than -11 dB to detect the true peak. The S-statistics method is able to tolerate a greater amount of noise as it remains robust even with SNR at -20 dB (robust in the sense that it always detects the phase coupled peak, even if it also detects extraneous peaks). The performance of the BWS is the best out of the three, being able to detect the frequency peak at a noise level as low as -22 dB.

Comparison of the specificity information for the 3 methods is shown in the bottom panels of Fig. 3.2. We observe that the S-statistics method is non-specific, as it detects an average of 14 additional non-phase coupled peaks over the range of SNR we have used. The BCI and BWS methods have high specificity, detecting only the phase-coupled peak up until the noise level at which these methods fail. This simulation shows that the BWS has the optimal combination of specificity and sensitivity in the case of varying amounts of noise in the data. Further, it should be noted that the degree of coupling in the test signal was not varied. Therefore, ideally the calculated values should not change with noise corruption. The top panel of Fig. 3.2 shows that all three methods' average calculated values decrease with increasing noise. However, the BWS is most resistant to this effect, with a relatively unchanging calculated value up until approximately 0 dB. This suggests that the calculated values from the BWS used to assess coupling strength are the most accurate, as the BWS method is the least affected by noise corruption. Further supporting evidence to this effect is shown in the proceeding sections.

3.4.3 Test of Amount of Phase Coupling

This example was designed to determine each method's fidelity in discriminating uncoupled phases. The amount of phase coupling was varied by injecting a number of data points that had uncoupled phases. The amount of phase coupling varied from 0% to 100% at an increment of 1%. For each level of phase coupling, 100 realizations of the test signals were generated. Each realization of the test signal was corrupted by 0 dB AGWN. For sensitivity testing, the calculated value for each method was recorded at the known phase coupled frequency. For specificity, the total number of significant detected peaks in the entire bispectrum was recorded and the median between the realizations is reported. These values are shown in Fig. 3.3 as a function of varying percent of phase coupling.

As shown in the top panels of Fig. 3.3, the percent of coupling that each method was sensitive to was approximately 50%, 35%, and 18% for the BCI, S-statistics, and the BWS, respectively. The bottom panels show the specificity of the three tests. The trend

here is the same as the prior example, where the specificity for the BCI and BWS is very high, while it is poor for the S-statistics method. This example provides evidence that the BWS has the best combination of sensitivity and specificity in detecting low levels of phase coupling. Further, it should be noted that the calculated value for the BWS linearly increases with increasing coupling percent for values above 18%, thereby suggesting that the BWS method provides a good quantification of the actual amount of phase coupling present in the system. The BCI and the S-statistics, however, show a more sigmoidal relationship with only a small window of linearity from approximately 40 to 70 percent coupling. The problem here is that it would be difficult to distinguish between two signals with high coupling strengths with the BCI and the S-statistics, as they will show up with similar values. This suggests that the BCI and S-statistics are less able to distinguish relative degrees of coupling when signals are strongly coupled.

3.4.4 Effects of Segment Number

Varying the number of segments is tested, as it has been demonstrated that only by having a sufficient number of segments will one detect the presence of phase coupling, if it exists (88). The size of each segment was kept constant at 64 data points. The number of segments was varied from 1 to 32 at an increment of one. For example, 1 segment means there are 64 data points and 32 segments correspond to 2048 data points in total, still 64 in each segment. For each segment, 100 realizations of the test signal were generated. Each realization was corrupted by 0 dB AGWN. Similar to previous simulations, the calculated value of the three tests and the number of detected peaks will be recorded for sensitivity and specificity, respectively. The result of this simulation is shown in Fig. 3.4.

The top panels of Fig. 3.4 show the calculated values of each method as a function of segment number. It should be noted here that the threshold for the BCI, shown as the dashed curve, changes with segment number according to the method by Elgar and Guza (33). It can be seen from the top panels that the minimum number of segments needed to detect significant peaks for the BCI, S-statistics, and BWS are 6, 4 and 3, respectively. This corresponds to 384, 256, and 192 points, respectively. The

specificity analysis in the bottom panel shows a similar trend as in previous tests, where the BCI and the BWS has the highest specificity, while the S-statistics method detects many erroneous peaks. From these results, it could be concluded that the BWS has the best tolerance to small amounts of data.

3.4.5 Test of Small Amount of Time Variance

In this simulation, we test the problem of having a small amount of time variation (nonstationarity) in the data while using the time-invariant bispectrum for analysis. This problem was originally reported by Pinhas et al. (93). The simulated test signal consisted of 2048 data points at a sampling rate of 1 Hz. This signal contains 32 segments of 64 data points each. Two frequency triplets are used in the signal. The first frequency triplet contains frequencies 0.05, 0.1, and 0.15 Hz. The second frequency triplet contains frequencies 0.2, 0.25, and 0.45 Hz. Both frequency triplets are fully phase coupled. The second frequency triplet exists only in the last segment of the data, while the first frequency triplet exists in all data. This simulates a signal where a small portion of it is different from the rest. One hundred realizations of the test signal were generated in this simulation, and the results are averaged. The three methods are compared and the results are summarized in Table 3.1.

As shown in Table 3.1, the calculated values for the BCI and S-statistics show a much higher value for the second triplet compared to the first triplet. This is an erroneous result, as the second triplet only exists in a small amount of data, which should, in theory, lead to a smaller magnitude of coupling. For the BWS, the calculated value of the second triplet is lower than the first. Further, the value of the first triplet is 32.35 times that of the second. This matches very well to the 32:1 ratio (# of segments between the first and the second frequency triplets) between the first and second triplet, which may suggest that the calculated value of the BWS accurately quantifies the degree of coupling that is in the signal. It is important to note here that for the BCI and the S-statistics, the calculated values also show a 32 to 1 ratio, except in the opposite direction (the value for the second triplet is 32 times that of the first). This phenomenon is further investigated in the next section.

3.4.6 Test of the Relative Magnitudes of the Calculated Values

In this simulation, the three methods were tested for their ability to quantify the relative coupling strengths between multiple coupling processes in a signal. The simulation signal used was the additive sum of two different frequency triplets, resulting in a signal with 6 frequency components. Each frequency triplet was generated in the same manner as described in part B of the Methods section. The specific frequencies used were f_1=0.05 Hz, f_2=0.1 Hz, $f_3=f_1+f_2$=0.15 Hz, f_4=0.2 Hz, f_5=0.25 Hz, $f_6=f_4+f_5$=0.45 Hz. The coupling percent of the $f_4f_5f_6$ triplet was varied between 0 to 100 percent at an increment of 1 percent, while the $f_1f_2f_3$ triplet was fully phase coupled. The signal was generated at 1 Hz sampling rate with 2048 data points. One hundred realizations of the test signal were generated, and the averaged results are shown. The calculated values at the two simulated frequency triplets, and the total number of detected peaks in the entire bispectrum, were recorded. Further, the ratio between the calculated values of the two triplets was also calculated. This ratio should ideally change linearly with coupling percent if the calculated values represent the actual strength of coupling.

The top panels of Fig. 3.5 show the plot of the ratio between the calculated values of the two triplets. Similar to the previous simulation, the BCI and S-statistics both have a linear region at the start of their detectable range. However, the ratio quickly saturates to the value of 1. For the BWS, the ratio remains relatively linear over its entire range. Linear regression of the ratio from the BWS yields an R^2 of 0.97. This linear behavior of the ratio is important when multiple components exist in a signal, and one wishes to quantitatively compare the degree of coupling between the mechanisms. For the BCI and the S statistics, this will be difficult at best since the ratio between the calculated values of 70 to 100 percent shows a very similar value. The BWS, on the other hand, shows a linear relationship across its detectable range, allowing for a meaningful quantitative comparison between the different components in the signal.

The bottom panels of Fig. 3.5 show the number of detected peaks from the three methods. The trend in this simulation is similar to all the other examples, where the BCI and the BWS are very sensitive and detect the correct number of peaks for their

detectable range, while the S-statistics method is not specific and detects a high number of peaks over all ranges.

In summary, the two simulations presented in this section show that the BWS is able to correctly determine the relatively magnitude of different coupling components in the same signal. The other two methods, on the other hand, are less effective in quantifying the degree of coupling between dynamics.

3.4.7 Application of the BWS to Renal Data

Our previous data analysis involving autoregressive bispectrum revealed quadratic phase coupling at the prescribed myogenic (MYO: 0.1-0.3 Hz) and tubuloglomerular feedback (TGF: 0.02-0.05 Hz) frequency ranges (23). Thus, the purpose of this section is to demonstrate the presence of such quadratic phase coupling using the BWS method, as well as its ability to discriminate only the significant phase coupling peaks. A typical BWS result is shown in Fig. 3.6. Panel A of Fig. 3.6 shows time series of a typical single nephron stop flow pressure. Note both fast and slow oscillations in the stop flow pressure data which reflect the activity of the two autoregulatory mechanisms. Panel B shows the bispectral estimation without the use of surrogate data on the data shown in panel A. The largest peak is at the prescribed frequency pair (TGF: 0.0234 Hz, MYO: 0.1328 Hz) associated with the TGF and MYO mechanisms. In addition to the largest peak, there are many smaller peaks present in the bispectral plot. It is difficult to discern whether these smaller peaks are the result of true phase coupled peaks or if they simply arise from frequency coupling alone, measurement noise or estimation error. Panel C shows the bispectrum of the same time tracing after using the BWS method to eliminate the erroneous peaks. The smaller peaks shown in panel B have mostly been eliminated, preserving only the phase coupled peak. Summarized results for both SDR (n=7) and SHR (n=7) are shown in Fig. 3.7. As shown in the top panel of Fig. 3.7, we observe nonlinear interactions between MYO and TGF in all SDR and SHR and this result is consistent with past studies (22, 23, 116). In addition, we found that there was a greater number of significant nonlinear interaction peaks with SHR than SDR. However, the strength of interactions is significantly greater in SDR

than SHR ($P < 0.05$) as shown in the bottom panel of Fig. 3.7. The magnitude result is shown in log scale due to the SDR having a BWS magnitude of more than an order of magnitude larger than that of the SHR.

3.5 Discussion

The simulation examples presented generally shows that the BWS offers the best combination of sensitivity and specificity under all of the tested conditions. Further, the BWS in general is more sensitive than the BCI and the S-statistics method in detecting coupling. The S-statistics method detects many spurious peaks; the culprit is the normalization procedure inherent in the computation of the BCI. The S-statistics method is reliable and appropriate to use when there is *a priori* information about the presence of quadratic phase coupling at specific frequencies. Furthermore, the use of S-statistics is more appropriate with parametric approaches to bispectral estimates, as the process of finding the proper number of autoregressive terms limits introduction of spurious peaks (23). Otherwise, the use of S-statistics via the direct method to computing the bispectrum is not advised. Finally, the BWS provides more accurate quantitative measure of the degree of coupling strength than either the BCI or S-statistics methods do, as shown in Figs. 3.3 and 3.5. It should be noted, however, that the BWS does not provide a normalized indicator for coupling strength, thus, the BWS will be more appropriate for comparison between different conditions.

In this work, a statistical method based on surrogate data was introduced to analyze bispectral data. This approach completely bypasses the use of the bicoherence index. As shown in the results, the normalization factor in the computation of the bicoherence index is the main culprit in providing less sensitive and less specific results. The BWS, because it does not use the BCI at all, provides results far superior to either the BCI or S-statistics. It should be noted that the bispectrum detects not only quadratic phase coupled phenomenon but it also provides information regarding nonlinearity and deviation from Gaussian process. Therefore, with the BWS approach, one can obtain statistical quantification regarding the phase coupling, nonlinearity and deviation from normality.

The BWS, BIC and S-statistics were all based on nonparametric bispectral estimation. However, all of the methods are also applicable to parametric bispectral estimation. In fact, the S-statistics method was already used with an autoregressive bispectral approach (23). Given the fact that the BWS outperforms the S-statistics and BIC, we surmise that the BWS will also be applicable as an accurate approach for determining the statistical threshold levels of the parametric bispectrum. The advantages of using the parametric over the nonparametric bispectrum are higher frequency resolution and its ability to retain the accuracy for data with short data records. However, the main disadvantage of the parametric approach is the determination of model order, which can be complex.

As in a previous study (23), consistent phase coupling was observed in tubular pressure recordings from both SDR and SHR with the application of the BWS. The BWS revealed that the SHR has a significantly greater number of MYO and TGF interaction peaks but the strength of coupling is smaller than SDR. This may be due to either more transient behavior or the TGF frequency shifting, both of which we have previously reported (34, 95). These results are also consistent with a recent modeling study (68), which suggests that the TGF mechanism in the SHR switches between different dynamic modes. This shifting of modes can lead to the increased amount of peaks detected in the SHR as each mode would show up as a separate peak. Furthermore, the shifting of modes would decrease the amount of time of each mode in the total time record, leading to a decrease in the magnitude of coupling observed.

The significance of detecting the presence of phase coupling in renal blood flow is that perhaps this can be used as a marker in differentiating normal versus disease conditions that may arise because of autoregulatory dysfunction in kidneys. It can be speculated that with progressive renal autoregulatory dysfunction, the presence of quadratic phase coupling, which is needed for efficient autoregulation in normal conditions, may dissipate. However, further studies are needed to determine if such a scenario occurs.

This work has been published in IEEE Transactions on Biomedical Engineering, 2008.

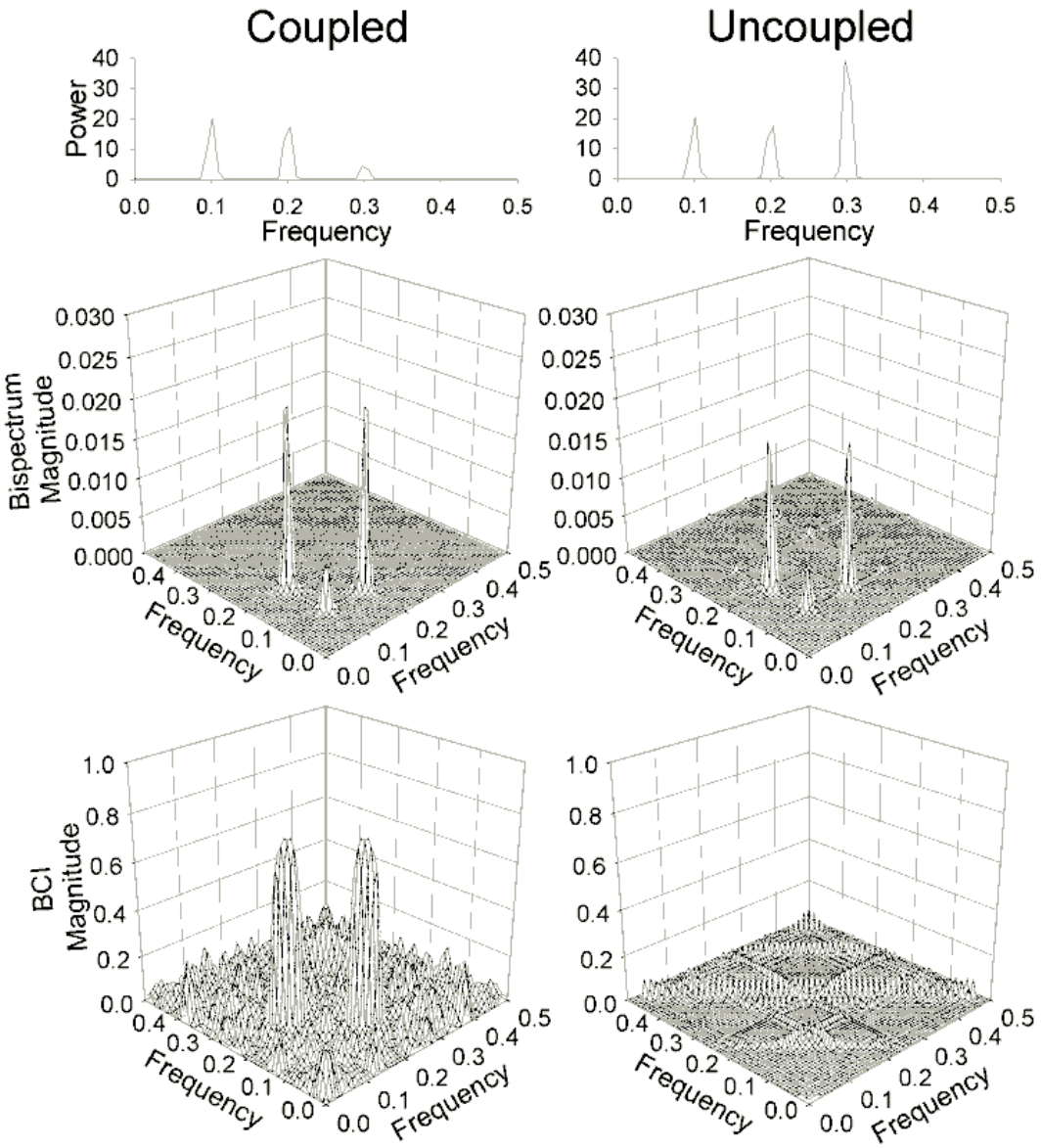

Figure 3.1 - Bispectra (middle panels) and bicoherence (bottom panels) with (left panels) and without (right panels) phase coupling. Note the similar phase coupling magnitudes for both phase uncoupled and coupled system.

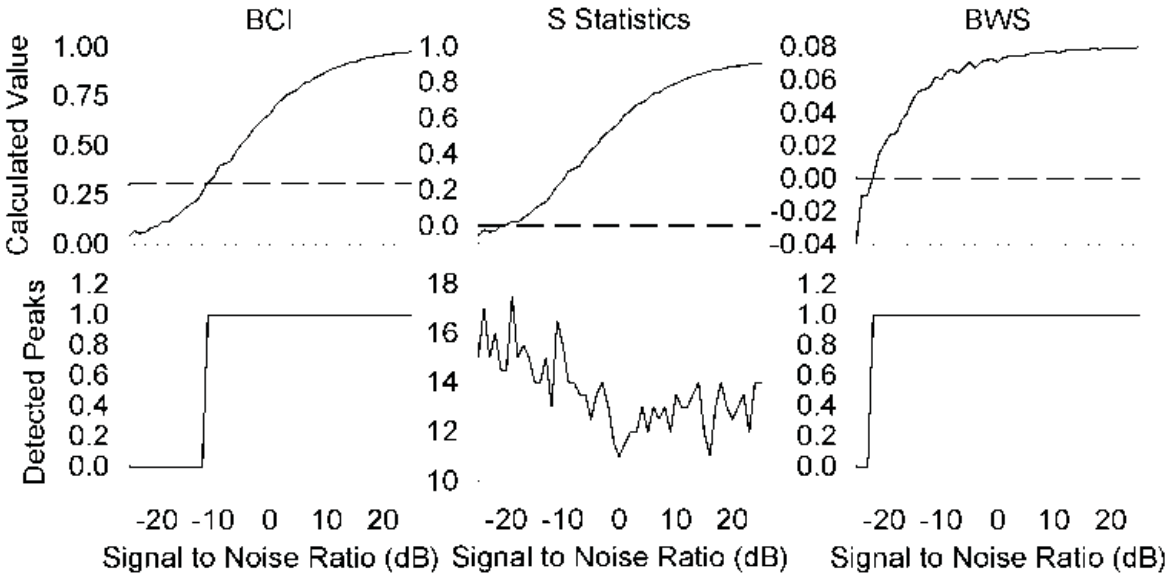

Figure 3.2 – Comparison of three bispectral methods with noise contamination. The data were corrupted by a variable amount of Gaussian white noise. The top panels show the calculated value of each method at the generated frequencies. The bottom panels show the median number of significant peaks detected at each noise level.

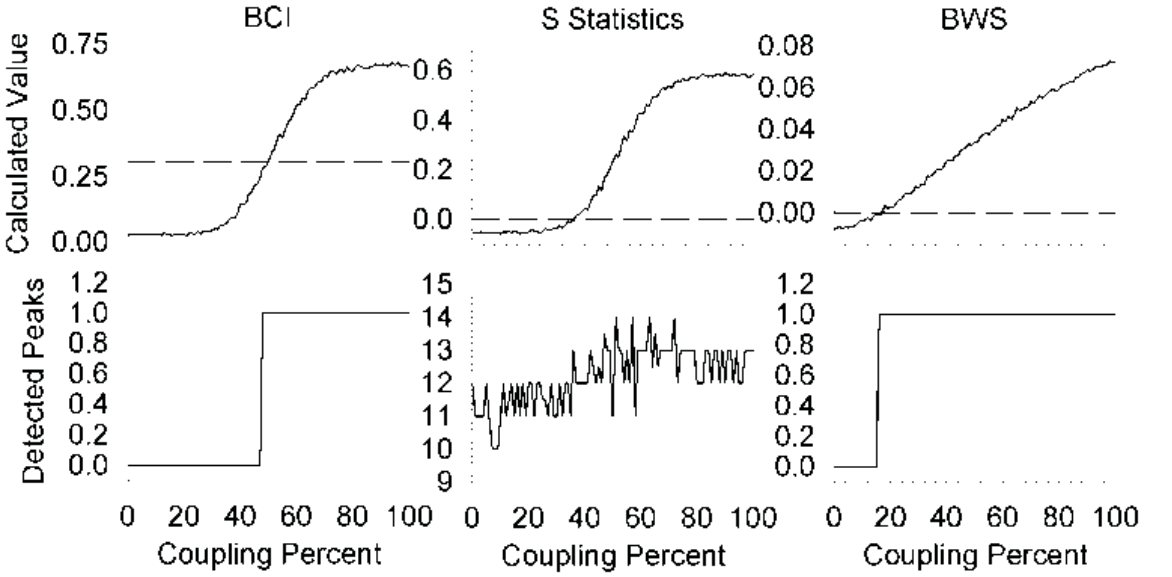

Figure 3.3 – Comparison of three bispectral methods with varying amounts of coupling. Plotted on the top panels are the calculated values at the known phase-coupled frequency for each of the three methods. The dotted lines show the significant threshold levels for each of the three approaches.

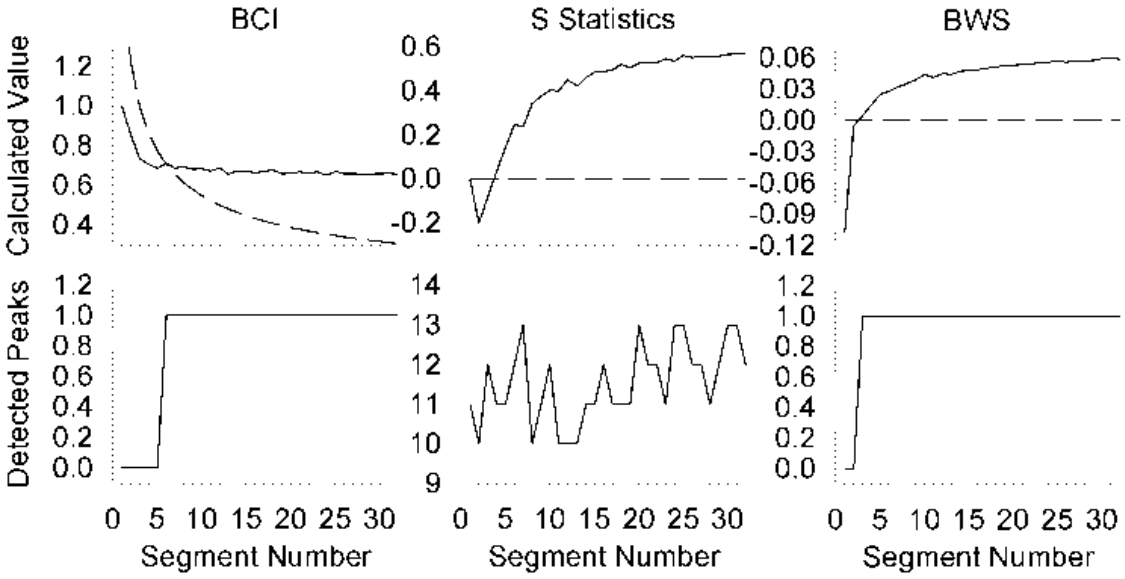

Figure 3.4 – Comparison of three bispectral methods with varying number of segments. The top panels show the calculated value of each method at the known phase-coupled frequency. The dotted lines in the top panels show the threshold levels for each method: 0.5 for the BCI, 2 for the S-statistics, and 0 for the BWS. The bottom panels show the number of detected peaks for the three methods.

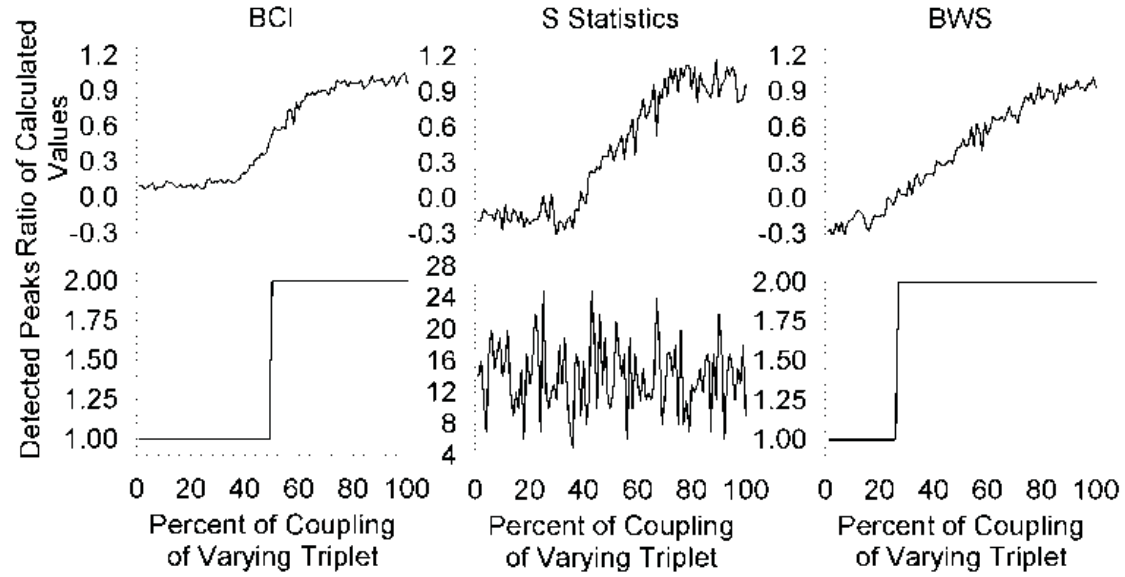

Figure 3.5 - Comparison of three bispectral methods with two triplets of varying amounts of phase coupling. In this simulation, the first triplet was fully phase coupled, while the second triplet had a varying amount of phase coupling ranging from 2 to 100 percent, in 1 percent increments. The calculated values for each method for the two triplets were recorded, and the ratio between the calculated values of the two triplets is shown in the top panels. The bottom panels show the number of detected peaks from the three methods.

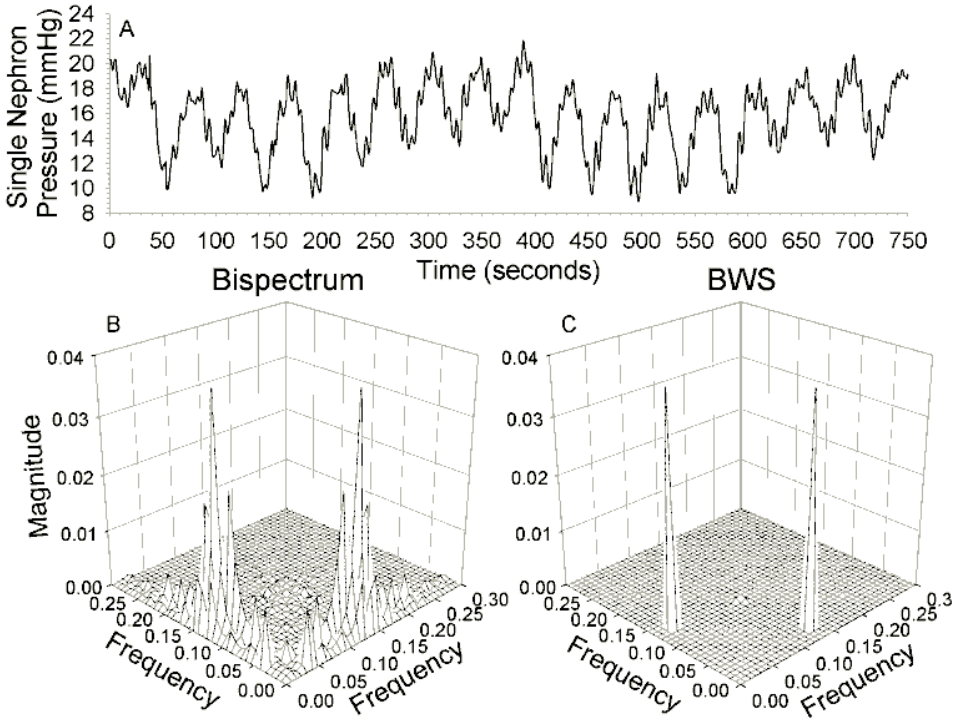

Figure 3.6 - Stop-flow pressure tracing (panel A) and the corresponding bispectrum without (panel B) and with surrogate data (panel C). Note the elimination of many peaks in panel B with the use of the BWS

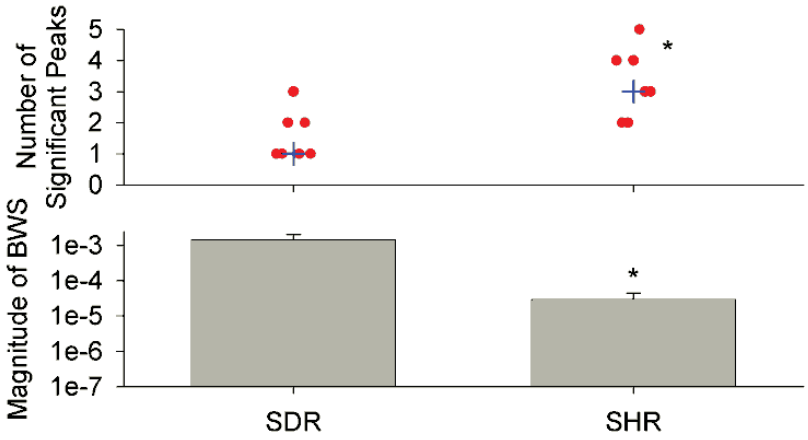

Figure 3.7 – Summary of the application of the BWS on renal stop flow pressure measurements on both SDR (n=7) and SHR (n=7). The top panel shows the number of significant peaks between the two strains, with the blue + representing the median. Both the magnitude and the number of peaks are significantly different ($P<0.05$), with the SHR showing a lower magnitude as well as a greater number of peaks. Bottom panel shows the average BWS magnitude of significant peaks between the TGF and MYO mechanisms in log scale.

	BCI	S-Statistics	BWS
Triplet 1	1.00	0.93	0.0940
Triplet 2	31.92	31.83	0.0029

Table 3.1 – Comparison of the three bispectral methods' abilities to tolerate a small amount of time variance in the data. The simulation used a signal with two frequency triplets, where both of the triplets are both frequency and phase coupled. However, triplet 2 only exists in the last segment of data, whereas triplet 1 exists in all data. Reported here are the calculated values from the three methods for triplet 1 and 2.

Chapter 4

On the Efficacy of the Combined Use of the Cross-Bicoherence with Surrogate Data Technique to Statistically Quantify the Presence of Nonlinear Interactions

4.1 Abstract

The cross-bispectrum is an approach to detect the presence of quadratic phase coupling (QPC) between different components in bivariate signals. Quantification of QPC is by means of the cross-bicoherence index (CBI). The major limitations of the CBI are that it favors only the strongly coupled signals and its accuracy becomes compromised with noise and low coupling strength. To overcome this limitation, a statistical approach which combines CBI with a surrogate data method to determine the statistical significance of the QPC derived from bivariate signals is introduced. The accuracy of the proposed approach was demonstrated using simulation examples which are designed to test its robustness against noise contamination as well as varying levels of phase coupling and data lengths. Comparisons were made to the traditional CBI and the method based on the use of cross-bispectrum followed by a surrogate data technique. The results show that the cross-bicoherence with surrogate data technique outperforms the two other method compared in both sensitivity and specificity and provides an unbiased and statistical approach to determining the presence of quadratic phase coupling in bivariate signals. These results are in contrast to the previous chapter where the auto-bispectrum combined with surrogate data approach had the best performance. Application of this approach to renal hemodynamic data was applied to renal stop flow pressure data obtained in the nephrons of the normotensive (N=18) and hypertensive (N=15) rats. We found significant nonlinear interactions between nephrons only when they are derived from the same cortical renal artery. The accuracy was 100% and verified by comparing the results to the known vascular connectivity between nephrons.

4.2 Introduction

In previous work, nonlinear coupling between tubuloglomerular feedback (TGF) and the myogenic (MYO) mechanisms within a single nephron (95, 111) as well as the whole kidney level (22, 95) was detected for both normotensive and spontaneously hypertensive rats (SHR) using a bispectrum approach. The reason for the interest in the detection of nonlinear interactions is that they can give rise to a number of system properties, including chaos, synchronization, and frequency modulation (116), which may be physiologically important, and which do not occur in linear systems. The bispectrum is an algorithm used to detect both frequency and phase coupling between different components of a signal and bispectral peaks should only appear when these two criteria have been met (88). However, in practice, having only the frequency coupling or insufficient segment averaging can lead to erroneous bispectral peaks. A long held dogma is that these erroneous peaks can be rejected by the use of a bicoherence index, but its determination of significant peaks favors only those with strong coupling. To overcome this limitation, we recently developed an algorithm which combines the bispectrum with surrogate data method to determine the statistical significance of the phase coupling (111). Our approach completely bypasses the use of the bicoherence index. Our method showed far greater sensitivity and specificity than the bicoherence index and paved a way for an unbiased and statistical approach to determine the presence of quadratic phase coupling.

For bivariate signals, the cross-bispectrum can be used to detect quadratic phase coupling (QPC) between dynamic components from two different signals. For example, it will be possible to detect coupling between the autoregulatory mechanisms from different nephrons (111). Our aim is to apply the cross-bispectrum to examine if there are any differences in nephron to nephron interactions between normotensive and hypertensive rats.

Inherent weaknesses of the cross-bispectrum are nearly identical to those of the auto-bispectrum. For example, the cross bispectrum also requires a sufficient number of segments to detect proper phase coupling. If these are not available, non-phase coupled components will appear in the resulting cross-bispectra, confounding the interpretation of

the results. The most widely-used approach to suppress these non-phase coupled peaks is via the cross-bicoherence index. Using multiple realizations of Gaussian white noise signals, Shils et al. (108) provided a quantitative approach to determine a 95% significance level to discriminate between erroneous and true phase coupled peaks, based on the number of segments used. However, the main disadvantage of this approach is that the distribution of white noise is different than the data. In addition, the significance level derived by the white noise is a stringent criterion and may miss weak couplings between two signals, thereby leading to type II error.

Given the aforesaid limitations and the fact that we found a solution to selection of the significance of the determined auto-bispectral peaks based on a surrogate data technique, we initially assumed the same method can be used for cross-bispectrum. That is, first calculate the cross-bispectrum followed by surrogate data to determine the statistical significance of the calculated cross-bispectral peaks. Note that in our recent study, it was found that using the auto-bispectrum followed by surrogate data to determine the statistical significance was more accurate than using either the conventional bicoherence index or bicoherence followed by the surrogate data(111). Similar to the auto-bispectrum case, we expected poor performance of the cross-bicoherence index for quantitative determination of the significance of the cross-bispectrum. To our surprise, the most accurate approach for auto-bispectrum (bispectrum followed by surrogate data) was not as effective for cross-bispectrum. Thus, the aim of the present study was to systematically investigate and compare three different approaches to determine the most accurate way to assess the significance of the estimated cross-bispectral peaks. The three methods compared are: 1) cross-bicoherence index, 2) cross-bispectrum with surrogate data, and 3) cross-bicoherence with surrogate data. We have previously shown that the method of using bicoherence followed by the surrogate data works better than using only the bicoherence but its accuracy was lower than the bispectrum with surrogate data approach (111). Note that the second and third method as defined above differ in that the former method uses cross-bispectral values whereas the latter method uses the cross-bicoherence values to determine the statistical significance.

To quantitatively compare three methods, computer simulations involving their effectiveness against varying levels of noise, coupling and data lengths were investigated.

Unlike the auto-bispectrum, it was found that the approach of cross-bicoherence with surrogate data performed the best for all test conditions considered. The technique of the cross-bicoherence with surrogate data was applied to stop flow pressure measurements obtained from two nephrons simultaneously in both normotensive and hypertensive rats to detect and discern quantitative differences in the quadratic phase coupling between two conditions.

4.3 Methods

4.3.1 Cross Bispectral Analysis

Given two stationary zero mean processes, *x(n)* and *y(n)*, the direct method of computing the cross-bispectrum, B_{XYX}, involves taking the average of triple products of the Fourier transform over *M* segments:

$$B_{xyx}(\omega_1, \omega_2) = \frac{1}{M}\sum_{m=1}^{M} X^m(\omega_1)Y^m(\omega_2)X^{m*}(\omega_1 + \omega_2) \qquad \text{(eq. 4.1)}$$

where $X^m(\omega_1)$ and $Y^m(\omega_2)$are the Fourier transform of the *m-th* segment and * indicates the complex conjugate.

Similar to auto-bispectrum, the cross-bispectrum will reveal peaks when quadratic phase coupling occurs between the two signals. An example of the QPC via the cross-bispectrum is illustrated in Fig. 4.1 using the following example (89):

$$\begin{aligned} x_1(n) &= e^{j\left(2\pi f_x(1)n\Delta + \phi_x(1)\right)} \\ x_2(n) &= e^{j\left(2\pi f_x(2)n\Delta + \phi_x(2)\right)} \\ y_1(n) &= e^{j\left(2\pi f_y(1)n\Delta + \phi_y(1)\right)} \\ y_2(n) &= e^{j\left(2\pi f_y(2)n\Delta + \phi_y(2)\right)} \\ x(n) &= x_1(n) + x_2(n) + x_1(n)x_2(n) \\ y(n) &= y_1(n) + y_2(n) + y_1(n)x_2(n) \end{aligned} \qquad \text{(eq. 4.2)}$$

The signals *x(n)* and *y(n)* are the two composite outputs of the simulation. In this simulation, the frequencies are set to: $f_x(1) = f_y(1) = 0.03$ Hz and $f_x(2) = f_y(2) = 0.12$ Hz to simulate the slow and fast mechanisms of renal autoregulation. 32 segments of 128 data

points of both *x(n)* and *y(n)* were generated (for a total of $n = 4096$ data points and step size $\Delta = 1$ second each), with the initial phase of each segment, ϕ, randomly distributed along 0 and 2π. Phase coupling is unidirectional from *y(n)* to *x(n)*, with the third term in *y(n)* being responsible for the coupling. Note that the simulated signals have imaginary portions. For visualization purposes, only the real portion of the signals is shown in the top two panels of Fig. 4.1. The bottom left panel shows the resulting cross-bispectra for these two simulated signals. Note that a single large peak is shown at the (0.03, 0.12) Hz frequency pair, suggesting significant phase coupling between the signals. The example provided was free of noise. More realistic example is to contaminate the signals as described in Eq. (4.2) with Gaussian white noise (GWN). The signal-to-noise (SNR) ratio was set to -20 dB. The result is shown in the middle panel of Fig. 4.1. While the largest peak is the coupled peak, with such a low SNR, we observe many noise-related peaks in the cross-bispectrum.

To address how one can comb through to find only the significant phase coupled peak, the most widely used approach is a cross-bicoherence index, which is essentially a normalized cross-bispectrum:

$$bic_{xyx}(\omega_1, \omega_2) = \frac{B_{xyx}(\omega_1,\omega_2)}{\sqrt{P_x(\omega_1)P_y(\omega_2)P_x(\omega_1+\omega_2)}} \qquad \text{(eq. 4.3)}$$

where bic_{xyx} denotes the cross-bicoherence and P denotes the power spectrum. Shils et al. (108) introduced a 95% threshold of $\sqrt{3}/\sqrt{N}$, where N is the number of segments. Using this threshold value for the simulation above, we would erroneously reject the true phase coupled peak at (0.03, 0.12) Hz frequency pair, as illustrated in the right panel of Fig. 4.1. This type II error is likely due to the fact that the above defined 95% threshold value is too stringent since it was based on Gaussian white noise simulations, thus, it is not able to discern a phase coupling that is contaminated by significant noise. While not shown, a similar type II error would occur when the magnitude of the phase coupled peak is weak. These issues will be further illustrated in the Simulation Example section.

To circumvent this white noise based 95% threshold value of the cross-bicoherence index, we demonstrate utility of two methods that utilize the concept of surrogate data technique. Specifically, the two methods utilize a surrogate data testing approach to determine the statistical significant threshold value for either the cross-

bispectrum or cross-bicoherence values. Surrogate data technique generates multiple random realizations of signal from real data that contain only the linear characteristics from the original signal. In essence, the surrogate data will not contain the phase couplings that are in the original signals and can therefore be used as the null condition for statistical comparison. We chose the iteratively refined surrogate data technique (IRSDT) (133). The IRSDT will destroy any nonlinearity in the signal, and has been shown to be more accurate than the amplitude adjusted Fourier transform technique (121) because it iteratively corrects for deviations in the spectrum as well as maintains the correct distribution of the signal.

100 realizations of surrogate data pairs were generated and the cross-bispectrum and cross-bicoherence values were calculated for each of the two methods. The mean and standard deviation between the 100 cross-bispectra or cross-bicoherence indices were then calculated, and the threshold was set to be the mean plus 2 standard deviations of the maximum peak in the cross-bispectrum or cross-bicoherence values. The magnitude of coupling is determined to be the difference between the original bispectrum and the calculated threshold. Using this method, the threshold for the cross-bispectrum is statistically determined and not based on arbitrary decision. The surrogate method based on the cross-bispectrum will henceforth be termed cross-bispectrum with surrogate (CBS) and the surrogate method based on the cross-bicoherence will henceforth be called cross-bicoherence with surrogate (CBicS).

4.3.2 Simulation Procedures

Computer generated data were used to compare the efficacy of the three methods. In these simulations, pairs of phase coupled signals were generated, per Eq. (4.2). Each of the bivariate signals contains 4096 data points with zero mean, and unit variance. The calculation of the cross-bispectra and cross-bicoherence is based on FFT resolution of 0.0078125 with the segment length of 128 and 50 percent overlap.

In the first simulation, fully phase coupled signals were generated and a varying level of GWN was added to the signal. In the second simulation, phase coupling was varied from 0 to 100 percent. For the third simulation, the number of data points was

varied in increments of 128. For each simulation, 100 realizations are generated for each condition and an average value was obtained. Further, the specificity of the algorithm was assessed by searching for the total number of significant peaks across each calculation. Theoretically, if the specificity is high, only one peak is shown.

4.3.3 Experimental Procedure

All experiments were performed under protocols approved by The Institutional Animal care and Use Committee at Stony Brook and The University of South Florida. Data were collected from a previous study where stop flow pressure recordings from two nephrons were simultaneously measured in normotensive Sprague-Dawley rats (SDR, 240-300g, n=15) and SHR(weight matched, 12 week old, n=18). Surgical preparation and the stop flow pressure measurements are detailed in our previously published study (23), thus, will only be briefly described here. Animals were anesthetized with halothane administered in an oxygen-nitrogen mixture and artificially ventilated after the administration of a muscle relaxant. Tubular flow was interrupted with bone wax in a selected proximal tubule, and intratubular hydraulic pressure proximal to the wax block was measured via a 1 to 3 um diameter micropipette attached to a servo-nulling pressure circuit. A similar procedure will performed onto a second nephron that is in close proximity to the original. Data from the two nephrons were recorded on a TEAC R-61 4-channel cassette data recorder for off-line analysis. The recorded data were replayed through an electronic low-pass filter with a roll-off frequency of 1.5 Hz and sampled digitally at 4 Hz. Vascular connections between nephrons were confirmed with vascular cast after measurement. Nephron pairs that did not show vascular connections were also analyzed to serve as negative control. In total, 9 of the 15 SDR and 7 of the 18 SHR show vascular connections under vascular cast.

4.3.4 Data Analysis

Data recorded at a sampling rate of 4 Hz were further down-sampled to 1 Hz after an anti-aliasing low pass filter at 0.5 Hz. The data were then zero meaned, detrended, and

normalized to unit variance in order to facilitate comparison. Since the direction of coupling is unknown between the nephrons, the cross-bicoherence with surrogate method was applied in both directions (e.g., B_{xyx} and B_{yxy}) to search for significant phase coupling. The total number and average magnitude of coupling for each data set was recorded. As described earlier, all data sets were analyzed regardless of whether physiological connections were present under vascular cast. Statistical testing was done using student's t-test or Mann-Whitney rank sum test.

4.4 Results and discussion

4.4.1 Test for normality

Both of the surrogate methods introduced in this study make use of the descriptive statistics of mean and standard deviation, which assumes normality. Therefore, it is important to first confirm that the calculated set of 100 surrogate cross-bispectrum and cross-bicoherence values follows a normal distribution. 100 realizations of the test signal were generated according to Eq. (2), and 100 surrogate data realizations were generated from each of the 100 test signals. The cross-bispectrum and cross-bicoherence were calculated for each surrogate data set, and the value at the coupling frequency was recorded. Each of the 100 sets of surrogate data cross-bispectrum and cross-bicoherence were tested for normality using the Kolmogorov-Smirnov goodness of fit test (140). All of the surrogate data sets were statistically confirmed to be from a normally distributed population ($P>0.05$).

4.4.2 Case 1: Noise Contamination Simulation

The three method's ability to correctly detect coupling in the presence of noise was tested. In this simulation, varying levels of Gaussian white noise were used to corrupt the test signal pairs. The noise was varied from 30 dB to -30 dB, in steps of -1 dB. At each noise level, 100 realizations of the test signal pairs according to Eq. (4.2) were generated, and each pair was corrupted by an independent pair of GWN. The

calculated mean value across the 100 test data sets at the true frequency pairs and the median number of detected peaks were recorded. The result from this noise simulation is shown in Fig. 4.2. The top panels show the mean calculated value, while the bottom panels show the median number of detected peaks. The dotted line on the top panels shows the threshold for significance for each method. The columns are arranged with cross-bicoherence results on the left, cross-bispectrum with surrogate (CBS) in the middle, and the cross-bicoherence with surrogate (CBicS) on the right.

The cross-bicoherence is able to discern significant phase coupling up to -18 dB of noise. Both surrogate data methods were able to discern significant phase coupling up to the simulation limit of -30 dB of noise. However, the middle bottom panel shows the CBS loses specificity with increasing noise, detecting a median of 4 peaks at -30 dB. The cross-bicoherence and the CBicS were very specific as both methods never detect more than 1 peak. Therefore, both cross-bicoherence based methods offers great specificity as neither detects erroneous peaks. However, the sensitivity of the cross-bicoherence was less compared to that of the CBS and the CBicS, as it was only able to discern phase coupling up to -11 dB of noise. Taken together, this shows that the CBicS offers the best combination of sensitivity as well as specificity in noise corrupted data.

It is interesting to note that the CBS's behavior with increasing noise is opposite of that of the two cross-bicoherence based methods in that its magnitude of the calculated value increases with increasing noise. A possible explanation for this phenomenon is that since the noise is Gaussian, as the noise level goes up, the magnitude of the cross-bispectra will increase at all frequency pairs, including the magnitude at the frequency of coupling. In contrast, the normalization procedure in the calculation of the cross-bicoherence suppresses this power from non-coupling mechanisms, therefore leading to a decrease in calculated value as the noise increases.

It is important to note that the noise levels used in this simulation are generally much higher than that which is normally experienced in real experiments. However, one must keep in mind that the test signals used in this simulation are all designed to specifically be detected by cross-bispectra techniques. Real signals from experiments are never in this form, and hence the algorithm's efficacy may decrease. Therefore, it is important to keep in mind that the results shown here are purely for comparative purposes

and not to be used as guidelines for noise tolerance for the algorithms in experimental settings.

4.4.3 Case 2: Coupling Percent Simulation

In this simulation, the amount of phase coupling needed to discern significant phase coupling was compared between the three methods. Test signal pairs were generated according to Eq. (4.2), with one part of the signal being phase coupled while the other part having random phases. The amount of the signal that was phase coupled was varied between 1 and 100 percent, in steps of 1 percent. At each percent, 100 realizations of the test signal pairs were generated. Similar to the previous simulation, the mean calculated value and the median number of detected peaks between the 100 realizations for each percent level was recorded. The results are shown in Fig. 4.3 and they are arranged the same way as in Fig. 4.2.

It is important to note that the CBS algorithm was able to detect significant coupling independent of the amount of phase coupling. This highlights a disadvantage of the CBS algorithm in that frequency coupling alone is sufficient for the CBS algorithm to detect as the presence of QPC. The results for the two cross-bicoherence based methods show that the cross-bicoherence requires that the signals be at least 60% phase coupled. The CBicS, on the other hand, requires only 25 percent of the data to be coupled for detection. This gives the CBicS a big advantage in that the algorithm can detect weakly phase coupled signals. Further, physiological systems are often time-varying in nature, which may result in signals that have intermittent coupling. This can be seen as a weakly coupled signal, as the phase coupling only exists in selected portions of the data. Again, the CBicS algorithm is able to detect this time-varying coupling better than either the cross-bicoherence or CBS algorithms.

Taking the noise and percent coupling simulation together points to a weakness in the cross-bicoherence based algorithms. It could be seen that the calculated value goes down regardless of whether it is due to increase in noise levels or decrease in coupling percent. Therefore, when the magnitude of the cross-bicoherence with surrogate between two signals is compared, one can never be sure of whether it is due to differences in noise

levels or the degree of coupling. This is similar to coherence analysis, where noise and the degree of coherence will both affect the magnitude of the result. Although this may be an inherit weakness in the algorithm, in most experimental cases one can usually assume that the noise levels are comparable between experiments and hence, this should not be an issue. One possible way to resolve this weakness would be to use a time-varying bispectral analysis, as a low coupling percent could be viewed as a time-varying process. In theory, the surrogate approaches could be implemented into a time-varying cross-bispectrum algorithm, allowing for statistical quantification.

4.4.4 Case 3: Data Length Simulation

In this simulation, the data length was varied in order to assess the data length requirements for each algorithm. Phase coupled test signals were generated according to Eq. (2). The data length was varied in steps of 128 points from 128 to 4098 in order to keep the segment number constant at 128. At each data point step, 100 realizations of the test signal pairs were generated and analyzed with the three algorithms. The results are shown in Fig. 4.4 and arranged in the same way as previous figures. Note that the threshold for the cross-bicoherence in this simulation changes as the number of segments changes.

The results show that the performance of both the cross-bicoherence and CBicS are similar, where the methods are able to discern significant coupling for 4 and 3 segments, respectively. The CBS algorithm was able to detect significant coupling with as few as 128 points (1 segment), but detected erroneous peaks with fewer than 2176 points (17 segments). Further, the calculated value for the CBS increased with decreasing data length. This points to a weakness in the CBS algorithm: at low segment numbers, the method loses specificity.

The simulation result for the cross-bicoherence points to a weakness in the segment number-based threshold in that at low segment numbers, the threshold becomes extremely high. This leads to a severe drop in sensitivity at low data points. One possible solution to this problem would be to decrease the segment size to increase the number of segments. However, this will lead to a decrease in resolution, as the segment size

determines the frequency resolution. Therefore, one must keep this tradeoff of resolution verses ability to detect significant coupling in mind while choosing segment size.

The simulation for the CBicS here also points to a potential weakness in the algorithm in that the calculated value decreases drastically with data points less than approximately 1000 points, even though it was able to still correctly detect a single coupling peak with low data points. Therefore, when analyzing physiological data one must keep the data length between data sets similarly sized for comparison.

4.4.5 Experimental Data results

The previous simulations show that the CBicS has superior sensitivity and specificity in relation to noise, number of data segments or weakly coupled data. Therefore, it was the chosen method for the analysis of the renal flow data.

To reiterate the importance of a statistical method for the analysis of bispectral results, analysis for a representative data set of anatomically connected nephrons is shown on Fig. 4.5. The top two panels of Fig. 4.5 show the stop flow pressure time traces from two simultaneously measured nephrons. The bottom left panel shows the cross-bispectrum of the data sets. Note the large peak shown at the MYO-TGF frequency range (0.13 Hz and 0.023 Hz, respectively). Further, many other smaller peaks are also present, whose magnitude suggests that they may also be significant peaks, hence complicating the interpretation of data. The bottom right panel shows the result after the application of the cross-bicoherence with surrogate algorithm, which shows a single large peak at the frequencies associated with MYO (0.13 Hz) and TGF (0.023) mechanisms. All of the smaller peaks shown on the cross-bispectrum were eliminated statistically using the CBicS algorithm, therefore allowing for the proper interpretation of data.

None of the nephrons pairs that did not have a physiological connectivity via vascular cast (6 of 15 SDR and 11 of 18 SHR) showed any significant coupling by the CBicS. This further proves the high specificity of the algorithm for the determination of significant phase coupling. It is unlikely to have coupling from pair of nephrons that do not have vascular connectivity.

The summarized results from the analysis of only the nephron pairs that show a physiological vascular connection are shown on Fig. 4.6. The top panel of Fig. 4.6 shows the mean magnitude of coupling between the two animal groups, which was shown to be significantly different from each other ($P<0.05$). The bottom panel of Fig. 4.6 shows the number of significant peaks from the data sets, which was not significantly different from the normotensive and hypertensive rats.

The cross bicoherence with surrogate algorithm is able to discern significant phase coupling between nephrons only if they are located on the same cortical radial artery. The nephrons that do not have vascular connections failed to show any significant phase coupling. This would suggest that synchronization between nephrons is achieved via proximity on the vasculature. One possible mechanism for such coupling was originally observed by Schnermann (101) and modeled later by Moore et al. (85).Basically, the theory is that when one segment of the afferent arteriole undergoes vasoconstriction via renal autoregulatory mechanisms, the pressure in a section of the vasculature upstream of the constriction site will be increased, thereby leading to enhanced response from the autoregulatory mechanisms. If this response is extrapolated to the cortical radial artery, then it may be possible that it is responsible for the coupling observed in this work. Further, this response would naturally decay with increasing distance from the original site of constriction. Therefore, the results here also suggest that the upper limit of distance for this response is at the distance of the cortical radial artery.

Another possible explanation for this coupling phenomenon is that an electrochemical signal is propagated via the vasculature originating from the TGF. Possible methods for this propagation have been proposed as the voltage gated Ca channels (78) or vianitric oxide activity (58, 62).

Although not shown, the coupling detected in this work only existed between TGF-MYO or the self coupling between MYO-MYO itself. Absent was the coupling between TGF-TGF. This may be a result of experimental condition of the stop flow pressure. In essence, since both nephrons' flow was interrupted via a bone wax plug, each of the nephron's own TGF mechanism was unable to sense the other's activity. On the other hand, since the MYO mechanism sense flow at the level of the afferent arteriole, it

is still able to sense and interact with the TGF mechanism. Therefore, this explains the presence of TGF-MYO and MYO-MYO interactions and not TGF-TGF.

Given the fact that a rat's kidney is composed of approximately 30,000 nephrons, it is reasonable to expect that nonlinear interactions observed at the whole kidney (22, 95) arise from coupling between nephrons derived from the same cortical radial artery (19, 64, 138). In a study by Sosnovtseva et al. (118), it was noted that the coupling between nephrons in SHR was shown to be less common in free flow nephrons. While our study differs from them because we used the stop flow pressure data, we still observe decrease in magnitude of coupling in SHR when compared to SDR. A decrease in the degree of coupling can result from intermittent coupling. Indeed, we previously found more intermittent coupling in SHR at the single nephron level (95). Such intermittent coupling may indicates a time-varying system. Thus, implementing a time varying version of the algorithm presented here in the future may yet reveal more information about the nature of the coupling phenomenon.

4.5 Conclusion

In summary, this work presents a surrogate data based approach to statistically quantify quadratic phase coupling based on the cross-bispectrum, adapted from a method we previously developed for the auto-bispectrum. Simulations were used to assess the efficacy of the algorithm along with the traditional method of cross-bicoherence. Simulation results showed that surrogate data technique combined with cross-bicoherence offered the best combination of specificity and sensitivity between the methods compared. These results are in contrast to the results we obtained in an earlier work on the auto-bispectrum, where surrogate data combined with the bispectrum was found to be superior. Application of this method to renal data revealed nephron-to-nephron interactions when they were derived from the same cortical renal artery. Having at hand the information on the connectivity between the nephrons, we were able to validate the accuracy of CBicS results; it was found that the accuracy was 100 percent. The CBicS method is a general purpose algorithm, thus, it can be adapted to many

different physiological signals. For example, quantitative determination of possible loss of coupling during epileptic seizures is an attractive application of the method.

This work has been submitted for review to Annals of Biomedical Engineering.

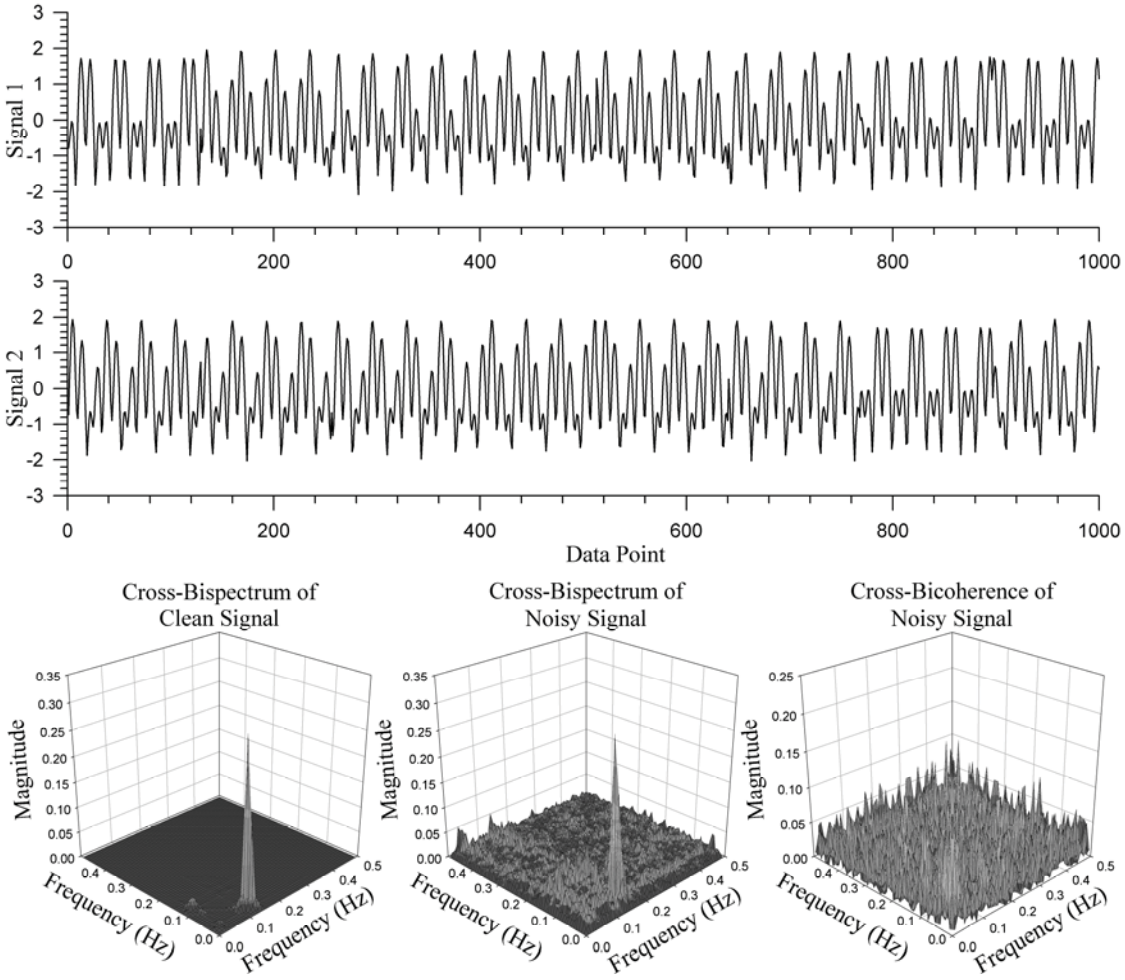

Figure 4.1 – Simulation demonstrating the necessity of a new quantification method for the cross-bispectrum. The top two panels show a pair of simulated signals that are phase coupled with each other. The bottom left and middle panels show the cross-bispectrum of a pair of clean and noisy signals, respectively. Noise confounds interpretation of the results as shown in the bottom right panel even with the use of cross-bicoherence index.

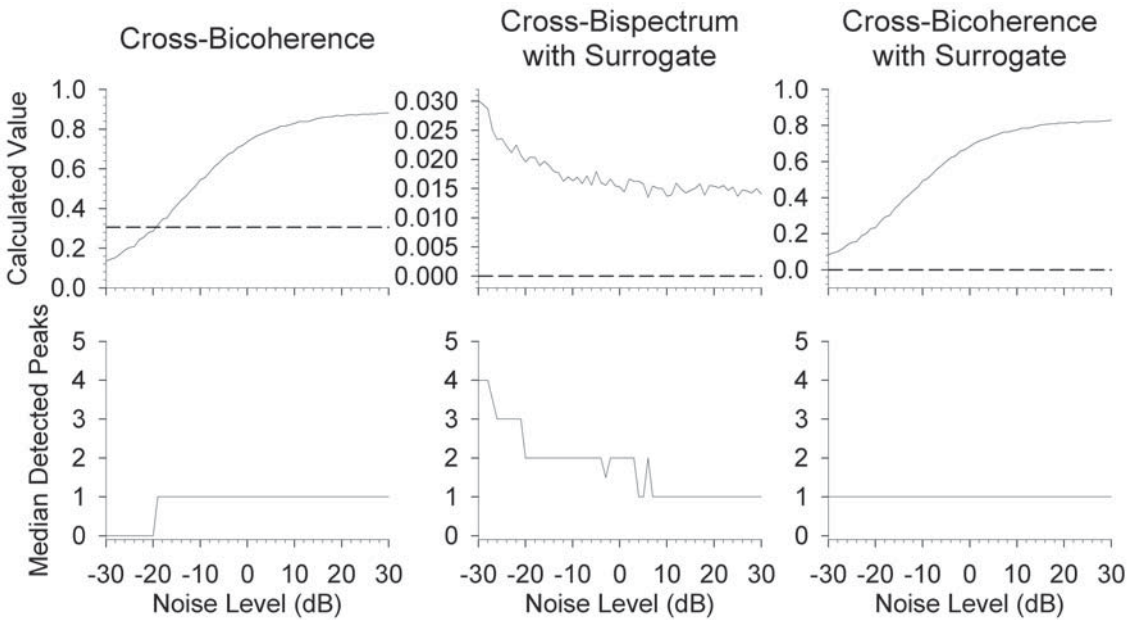

Figure 4.2 – Simulation summary to test the three algorithm's efficacy against varying noise levels. The top panels show the calculated value of the respective methods, while the bottom shows the median number of detected peaks. Simulations were performed in steps of 1dB with 100 realizations at each noise level.

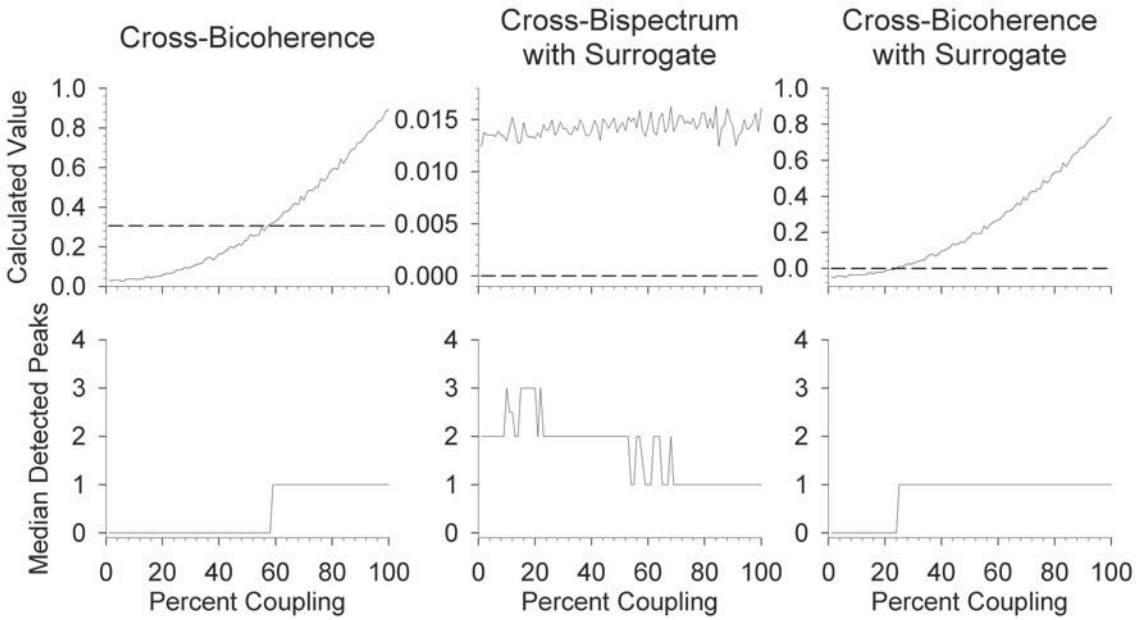

Figure 4.3 – Simulation summary to test the three algorithm's efficacy against different percent of coupling. The top panels show the calculated value of the respective methods, while the bottom shows the median number of detected peaks. Simulations were performed in steps of 1 percent, with 100 realizations at each percent level.

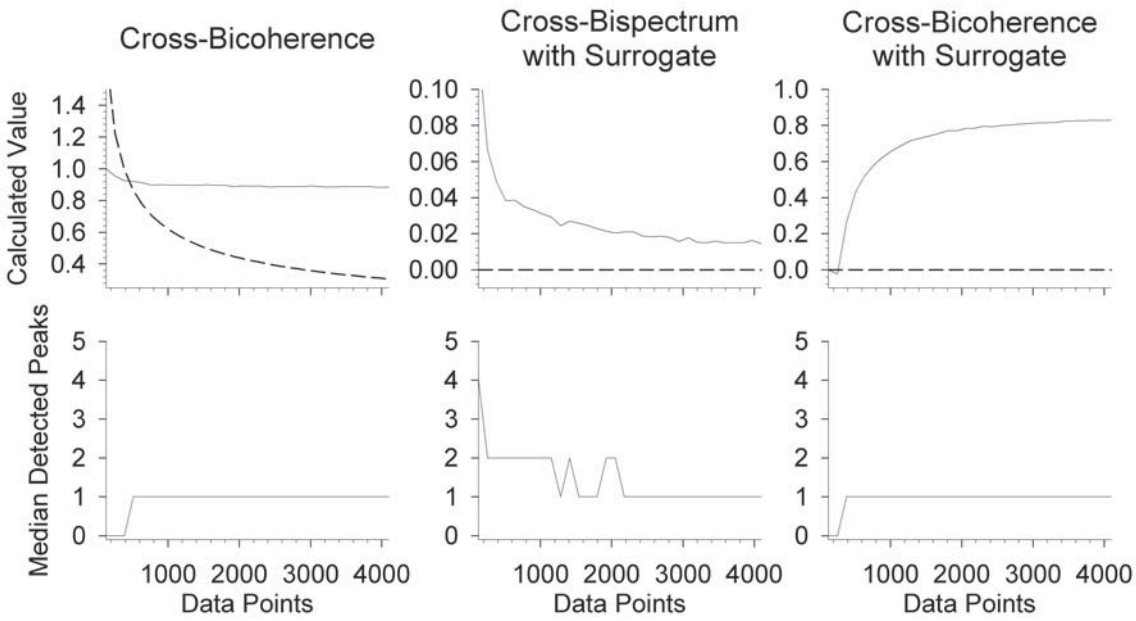

Figure 4.4 – Simulation summary to test the three algorithm's efficacy against different number of data points. The top panels show the calculated value of the respective methods, while the bottom shows the median number of detected peaks. Simulations were performed in steps of 128 points, with 100 realizations at each data length.

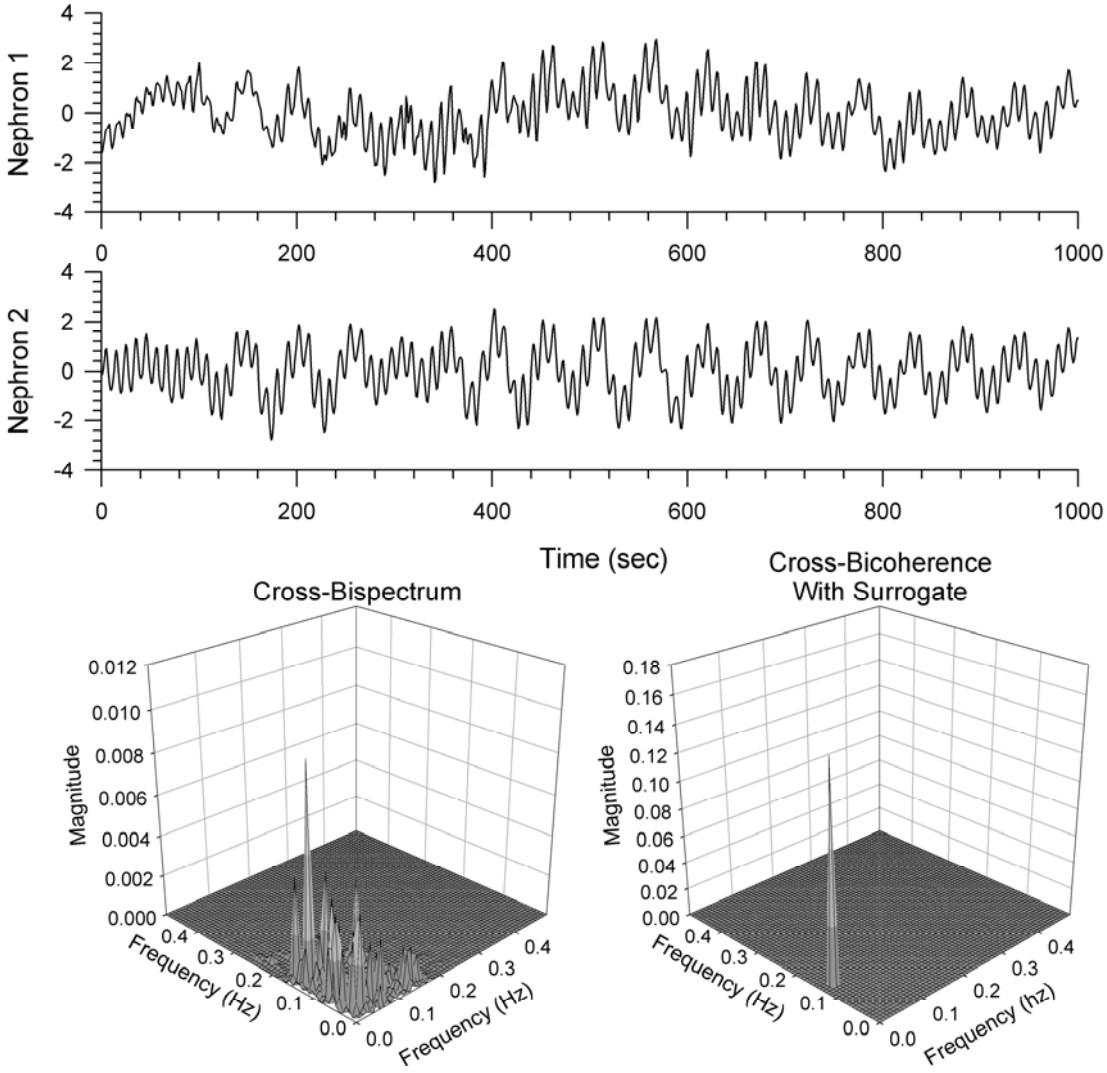

Figure 4.5 – Representative data from the stop flow pressure meansurements. The top two panels show pressure measurements from two simultaneously measured nephrons. The bottom left panel shows the cross bispectrum of this pair of data. Note that in addition to a large peak, many other smaller peaks appear, confounding the interpretation of the cross-bispectrum. The bottom right panel shows the result from the application of the cross-bichoerence with a surrogate method. The non-significant peaks shown in the cross-bispectrum are all removed, leaving only one significant true peak.

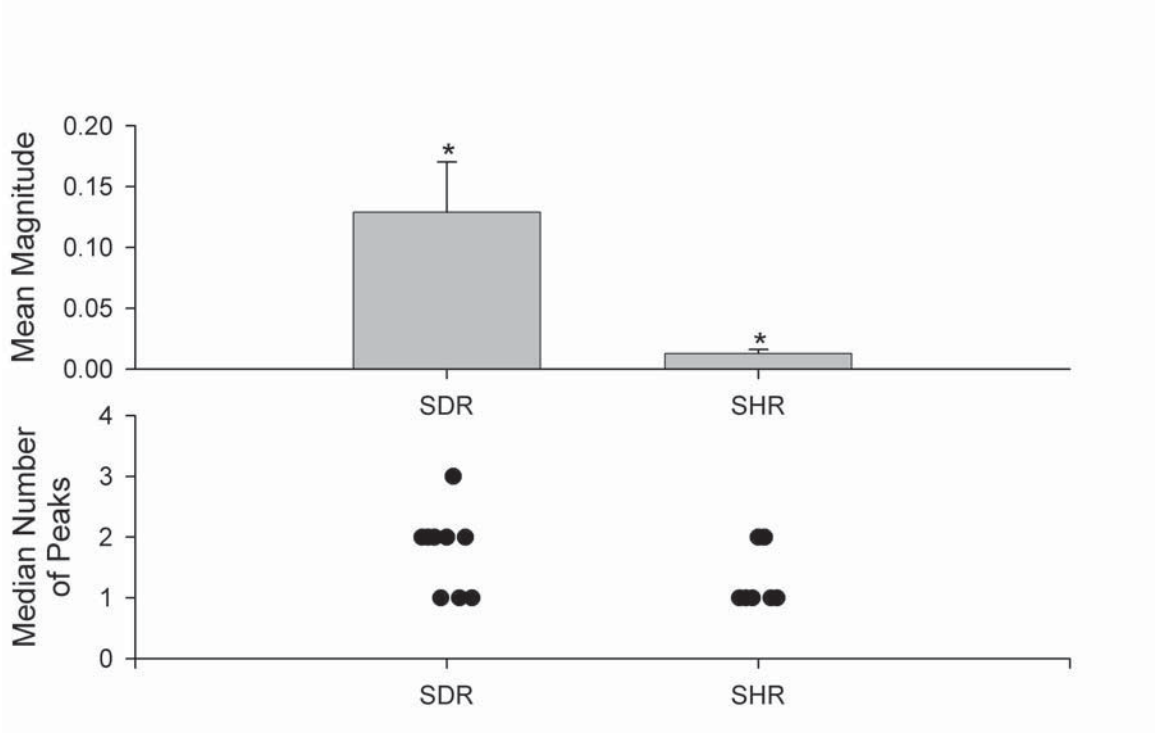

Figure 4.6 – Summary results from the stop flow pressure experiment, with n=9 and n=7 for SDR and SHR, respectively. Statistical significance is shown with * (P<=0.05).

Chapter 5

Detection of Low Frequency Oscillations in Renal Blood Flow

5.1 Abstract

Detection of the low frequency (LF; ~0.01 Hz) component of renal blood flow, which is theorized to reflect the action of a third renal autoregulatory mechanism, has been difficult due to its slow dynamics. In this work, we used three different experimental approaches to detect the presence of the LF component of renal autoregulation using normotensive and spontaneously hypertensive rats (SHR), both anesthetized and unanesthetized. The first experimental approach utilized a blood pressure forcing in the form of a chirp, an oscillating perturbation with linearly increasing frequency, to elicit responses from the LF autoregulatory component in anesthetized normotensive rats. The second experimental approach involved collection and analysis of spontaneous blood flow fluctuation data from anesthetized normotensive rats and SHR to search for evidence of the LF component in the form of either amplitude or frequency modulation of the myogenic and tubuloglomerular feedback mechanisms. The third experiment used telemetric recordings of arterial pressure and renal blood flow from normotensive rats and SHR for the same purpose. Our transfer function analysis of chirp signal data yielded a resonant peak centered at 0.01 Hz that is greater than 0 dB, with the transfer function gain attenuated to lower than 0 dB at lower frequencies, which is a hallmark of autoregulation. Analysis of the data from the second experiments detected the presence of ~0.01 Hz oscillations only with isoflurane albeit the strength was weaker when compared to telemetry recordings. With the third experimental approach, the strength of the LF component was significantly weaker in the SHR than in the normotensive rats. In summary, our detection via the AM approach of interactions between the LF component and both TGF and MYO, with the LF component having an identical frequency to that of the resonant gain peak, provides evidence that 0.01 Hz oscillations may represent the third autoregulatory mechanism.

5.2 Introduction

The long term regulation of systemic blood pressure is one of the major functions of the kidney. The functional unit of the kidney, the nephron, requires a stable input of fluid to perform its function. However, systemic blood pressure fluctuates over a large range of frequencies, which would destabilize renal function without a proper control mechanism to compensate for blood flow variations (45). It is known that the nephron has the ability to regulate its own blood flow, a phenomenon termed autoregulation. Another role of the autoregulatory mechanism is to provide protection for the renal vasculature from large fluctuations in systemic pressure (6, 7). Abnormalities in the autoregulatory mechanisms have been implicated in many diseases, such as hypertension induced renal disease and chronic renal failure (6, 7).

Renal autoregulation is widely accepted to be mediated by two mechanisms. The first is the slower of the two mechanisms, the tubuloglomerular feedback mechanism (TGF), which oscillates between 0.02-0.05 Hz in rats (30, 44). The myogenic mechanism (MYO) is faster than TGF and exhibits oscillations in the frequency range between 0.1-0.3 Hz (58, 131). On the basis of experiments using a step decrease in blood pressure, Just et al. (57, 60) have proposed the existence of a slower, third autoregulatory mechanism which operates at ~0.01 Hz. To date, little is known about its mechanistic origin, but its operating time scale may indicate involvement of angiotensin II (112). The presence of the third mechanism is somewhat controversial because assessments of autoregulation dynamics using broadband blood pressure perturbations have not revealed such a low frequency component (75, 76). However, there are two possible reasons why behaviors consistent with the third mechanism have not been observed in these dynamic autoregulation studies. First, preprocessing of renal blood pressure and blood flow data often involves detrending, which may well have filtered out any ~ 0.01 Hz oscillation. Second, the time interval and, hence, the number of data points analyzed is limited when traditional power spectral methods are used, and this makes it difficult to detect low frequency peaks.

One computational approach to discern the presence of the autoregulatory mechanisms is to look for their interactions. An example is an elegant study by

Schnermann and Briggs which demonstrated that the strength of the TGF response depends on the state of the MYO system at the single nephron level (101). Further, evidence of interactions between the two autoregulatory mechanisms was buttressed by a study in which Chen et al. (19) showed that coupling exists between nephrons that have physiological vascular connections. Consequently, such interaction phenomena were detected in both single nephrons and whole kidneys using a myriad of computational approaches, including the Volterra-Wiener kernel (22), the bispectrum (111), frequency and amplitude modulation (116, 117), and frequency locking via a wavelet method (118).

In this work, we utilized three separate experimental approaches to detect the low frequency (LF) oscillation which is thought to be related to a third autoregulatory mechanism. In the first experimental approach, we used a chirp signal forcing in the blood pressure (BP) of anesthetized normotensive rats to elicit characteristic oscillations associated with the LF component. Given the fact that both TGF and MYO interact, and if the putative third mechanism does indeed exist, it is reasonable to assume that it should also be coupled to the two other autoregulatory mechanisms. Thus, in the second and third experimental approaches, we hypothesize that the putative third autoregulatory mechanism interacts with the MYO and TGF mechanisms, and that the interactions should be evident in the spontaneous blood flow fluctuation data. The computational method we used in this study, complex demodulation (CDM), provides very high resolution of time-frequency spectra, which is required to resolve the low frequency oscillations associated with the operation of the third mechanism (57, 60). Specifically, we used CDM to identify either amplitude modulation (AM) or frequency modulation (FM) in the frequency bands normally associated with the TGF and MYO mechanisms since they would be the result of any interaction phenomenon. Thus, the aim of the study is to verify the presence of the third autoregulatory mechanism by looking for its interactions with the MYO and TGF mechanisms, and to determine if the transfer function gain magnitude on the chirp signal experiment provides the signature of the dynamics of autoregulation.

5.3 Methods

5.3.1 Animal preparation

Experiment 1, as described below, was performed for the present study in the laboratory of Dr. Cupples. Experiments 2 and 3 below were performed for the present study in the laboratory of Dr. Chon.

5.3.2 Experiment 1 – Chirp signal blood pressure perturbation

The first experiment was approved by the Animal Care Committee of the University of Victoria and was conducted under the guidelines promulgated by the Canadian Council on Animal Care. Five adult male Long Evans rats (~300 g) had free access to water and food at all times prior to the acute experiments. These animals are normotensive and we have shown previously that their renal blood flow dynamics are remarkably similar to those of other normotensive strains (130). Twenty min prior to anesthesia each rat received buprenorphine (Temgesic®, 0.01 mg/kg i.p. Reckitt and Colman Pharmaceuticals Inc., Wayne, NJ). Anesthesia was induced by 5% isoflurane in inspired gas (30% O_2, 70% air). After induction the anesthetic concentration was reduced to ~2%. The animal was transferred to a servo-controlled, heated table to maintain body temperature at 37°C, intubated, and ventilated by a respirator (RSP 1002, Kent Scientific Corp., Litchfield, CT). During the 1 hour post-surgical equilibration period inspired anesthetic concentration was titrated to the minimum concentration that precluded a blood pressure response when the tail was pinched (~1%).

Cannulas were placed in the right femoral artery and vein. A constant infusion delivered 1% of body weight per hour throughout the experiment and contained 2% charcoal washed bovine serum albumin in normal saline. The left kidney was approached by a flank incision, immobilized in a plastic cup, and covered with plastic wrap. The flow probe (1PRB, driven by a Transonic Systems Inc model T401 flowmeter) was placed around the renal artery; it was fixed in place and acoustic coupling

assured as recommended by the manufacturer. Femoral arterial pressure was measured by a Kent pressure transducer (TRN050) driven by a TRN005 amplifier.

A motorized clamp was placed on the aorta between the right and left renal arteries and was used to force blood pressure. The motor was driven by a program which operates in a negative-feedback manner to impose chirp forcing of renal perfusion pressure 15-20% below the spontaneous level of blood pressure. Care was taken to ensure that renal perfusion pressure remained within the autoregulatory range at all times. Data were low pass filtered at 40 Hz and digitized with 12 bit resolution at 200 Hz.

5.3.3 Experiment 2 – AM and FM detection in anesthetized animals

For the acute experiments, 24 animals (6 SDR and 6 SHR for each anesthetic) were anesthetized with either inactin (135mg/kg) or isoflurane (3% initial, 1% maintenance). The animals were then placed on a servo-controlled heated table to maintain a body temperature of 37^{o}C. A tracheostomy was performed to aid respiration. The right femoral artery and vein were catheterized (PE-50 and PE-10, respectively) for blood pressure measurement and infusion of isotonic saline to compensate for surgical fluid losses, respectively. The left kidney was isolated and placed in a Lucite cup. An ultrasonic flow probe (Transonic Systems, Inc., Ithaca, NY, series 1PR) was placed around the renal artery for measurement of renal blood flow. The animals were allowed 1 hour to recover from surgical stress before experimental measurements were made.

5.3.4 Experiment 3 – AM and FM detection via telemetric measurement

Male Sprague-Dawley rats (SDR) and spontaneously hypertensive rats (SHR) between 200-250g (Taconic Farms) were used in the experiments. All experimental protocols were approved by the institutional guidelines of animal care and use in research and approved by the Institutional Research Board (IACUC #20081267) on the use of animals for research at the State University of New York at Stony Brook. Prior to surgery, the animals had free access to standard rat chow and tap water, and were housed

individually in a temperature controlled room with a 12 hour light and 12 hour dark cycle. A total of 5 SDRs and 5 SHRs were used.

Animals were anesthetized using sodium pentobarbital (50 mg/Kg, intraperitoneally). After induction of anesthesia, an ultrasonic flow probe (Transonic Systems, Inc., Ithaca, NY, series 1PR) was placed around the left renal artery. The cannula of a blood pressure telemeter (PA-C40, Data Sciences International, Saint Paul, MN) was also implanted into the right femoral artery. After surgery, the animal was placed on a heated pad to facilitate recovery from anesthesia. The animals were studied after a one week period of surgical recovery Animals were monitored for signs of infection on a daily basis.

5.3.5 Experimental Protocol

For the telemetry experiment, each animal was housed individually in a temperature controlled room set on a 12 hour light and 12 hour dark cycle, with free access to standard rat chow and tap water. After the connection of the animal to the blood flow recording equipment, the animal was allowed a 15 minute adjustment period before measurements began. Renal blood flow (RBF) and systemic blood pressure was measured for 2 hours each day starting at 10 am for a period of 1 week. During the recording period, spontaneous activity of the animal was recorded by the investigator. Only data segments collected when the animal was at rest were analyzed in order to avoid movement artifacts. For the acute experiments, performed under anesthesia, spontaneous BP and RBF were recorded for 1 hour after the recovery period.

For the telemetry experiment, data were recorded at a sampling rate of 250 Hz using the Dataquest A.R.T. system (Data Sciences International, St. Paul, MN). For the acute experiment, data were collected at 100 Hz using a Powerlab 16RSP A-to-D converter (ADInstruments, Inc., Colorado Springs, CO). All data were down-sampled to 1 Hz sampling rate following digital low-pass filtering to avoid aliasing.

5.3.6 Chirp blood pressure forcing

The low frequency response characteristics of blood flow fluctuations in anesthetized Long Evans rats were investigated by imposing a sinusoidal forcing with linearly increasing frequency (0.001 – 0.02 Hz) on renal perfusion pressure. The rationale for using a chirp signal on the blood pressure forcing is to excite any autoregulation mechanism that may resonate within the perturbation frequency band. While we were primarily interested in detecting 0.01 Hz oscillations, we used a wide range of frequencies (0.001-0.02 Hz) for the blood pressure forcing in order to avoid introducing bias and to indentify other possible oscillations.

A flow chart of the data processing steps along with a representative data set is shown in Fig. 5.1. The first row shows the chirp signal of the BP forcing and the resultant RBF data. The first step is to calculate the time-frequency spectrum of each signal using a complex demodulation (CDM) approach, as shown on the second row. Note the linearly increasing frequency in BP perturbation and RBF response. Next, the magnitude of the peak frequency was tracked across time, as shown on the third row. Finally, the ratio between the RBF and the BP amplitudes across time was calculated as shown on the fourth row, plotted in log scale. Ratio values above the threshold of 0, shown as the dotted line, indicate characteristic resonance of the autoregulation system. Note that since the frequency increases linearly with time, the x-axis in this figure can also be plotted in terms of frequency.

5.3.7 Amplitude modulation (AM) and frequency modulation (FM) detection algorithm

AM and FM denote that either the amplitude or the frequency of a component in a signal, termed the carrier signal, is changed by another oscillatory mode, termed the modulation signal:

$$m(t) = M * \cos(\omega_m t + \theta_m)$$

Here M is the modulation magnitude, and ω_m and θ_m are the modulation frequency and phase. The un-modulated carrier signal is denoted as:

$$c(t) = C * \cos(\omega_c t + \theta_c)$$

Where C is the carrier magnitude, and ω_c and θ_c are the carrier frequency and phase. For AM, the amplitude of the carrier signal is modulated, such that:

$$c_{modulated}(t) = \big(C + m(t)\big) * \cos(\omega_c t + \theta_c)$$

For FM, the modulating frequency is calculated by an integral, such that:

$$C_{modulated} = C * \cos\left(2\pi f_c t + \int_0^t m(\tau) d\tau\right)$$

Simulated data containing AM were created to illustrate the concepts. In this simulation, components with frequencies to those exhibited by renal autoregulatory mechanisms were used. Specifically, two carrier frequencies, at 0.03 and 0.12 Hz, were modulated by a 0.01 Hz mechanism. The top panels of Fig. 5.2 show AM signals. Panel A shows the higher carrier frequency (0.12 Hz) modulated by 0.01 Hz, while panel B shows the lower carrier frequency (0.03 Hz) modulated by 0.01 Hz. Panel C shows the composite signal that combines both the high and low frequency signals in panels A and B.

The general approach to detecting AM is shown in panels D to H in Figs. 5.2. The first step is to calculate the time-frequency representation (TFR) of the original signal using CDM, shown in panel D in both figures. The CDM was chosen for this calculation as it has been shown to have one of the highest frequency and time resolutions while preserving accurate amplitude information (128). After the calculation of the TFR, the average amplitude at the MYO and TGF frequency bands were extracted (0.1 - 0.3 Hz and 0.02 – 0.05 Hz, respectively), as shown in panels E and F. Next, the frequency spectra of these extracted time traces were calculated to show the frequency and magnitude of modulation, shown as the solid line in panels G and H. For illustration purposes, the maximum magnitude of these spectra is shown to be 1. For this algorithm, only modulation at the low frequency range (0 – 0.02 Hz) was examined. The reason for this is to avoid detecting TGF modulation when the method is used with actual blood flow renal data. Note that the peak of this spectrum is correctly shown to be at a simulated modulation frequency of 0.01 Hz. This simulation illustrates how even a low frequency component (~0.01 Hz) can be reliably detected by looking for AM phenomena with the aid of a high-resolution time-frequency spectral method.

For FM detection, we employed a weighted average method to account for varying MYO frequencies in the 0.1-0.3 Hz band. Specifically, for each time point, any spectral peak that is above Gaussian white noise (GWN)-derived threshold values (as detailed in the proceeding paragraph) is selected. A weighted average frequency was calculated by summing the frequency of all significant peaks multiplied by their own individual magnitude. This sum was then divided by the sum of the magnitudes of the significant peaks (e.g., $\bar{f}_w = \frac{\sum_{i=1}^{N}(f_i A_i)}{\sum_{i=1}^{N} A_i}$). In essence, this calculation provides a weighted frequency average based on the strength of each frequency peak.

In order to assess the significance of this modulation, a statistical threshold based on GWN was calculated; it is shown as the dotted line in panels G and H of Fig. 5.2. To obtain this threshold, 1000 realizations of GWN with the same data length and variance as the original data signal were generated. Each realization of GWN was analyzed with modulation detection algorithm, resulting in 1000 spectra. The mean plus two standard deviations of these 1000 spectra were then taken as the statistical threshold to determine significance of modulation. It is important to note that the averaged white noise spectrum has greater power at low frequencies. This is due to the fact that the GWN data is band-limited, and this results in better representation of low frequencies than higher frequencies. This illustrates the importance of using a statistical threshold to determine significance, as band-limited random signals have a bias towards lower frequencies.

5.3.8 Data analysis

For the chirp forcing experiment, data were collected at 200 Hz, then low-pass filtered with a cutoff frequency of 0.1 Hz and down-sampled to 0.5 Hz. Finally, the data underwent linear trend removal, and were normalized to zero mean and unit variance.

All modulation analyses of data from conscious rats were performed on 10 minutes data segments. All data were filtered with a low-pass anti-aliasing filter followed by down sampling to 1 Hz which resulted in a total of 600 data points. This segment size was chosen because of the need to analyze only telemetric data sets that are free from substantial movement artifacts. The data were then normalized to zero mean and unit-variance to permit comparison between SHR and SDR. The CDM was employed with a

FFT segment size of 1024 points (zero padding included) which yielded a resolution of 0.000976 Hz. Because we collected telemetry data for 7 days, we were able to obtain 16 to 25 data sets of 10 minute duration in each animal that were essentially free of motion artifacts. Analysis was performed on each segment and the final results were averaged for each animal. Further, the percentage of significant (motion-free) segments for each animal was recorded. For the acute data collected for one hour under anesthesia, the percentage of significant segments was not recorded.

Statistical analysis was done using the SigmaStat (Systat Software, Inc., San Jose, CA) software package. We used Student's t-test for 2 groups (e.g., SDR vs. SHR in the telemetry experiments), and one-way ANOVA for multiple groups (e.g., SDR vs. SHR in the anesthesia and telemetry experiments). The significance level was $P < 0.05$.

5.4 Results

For the chirp data, all animals (n=5) showed significant resonance oscillatory peaks in the vicinity of ~0.01 Hz, similar to the results shown in Fig. 5.1. The group average for the 5 animals is shown in Fig. 5.3. The solid line indicates the mean, while the dashed lines indicate the standard deviation. The large solid line shows statistical significance above the zero threshold which is shown as the dotted line. The mean peak frequency was 9.0 ± 0.5 mHz for all animals.

Analysis of all of the data collected from conscious animals via telemetry and from isoflurane anesthetized rats identified only significant amplitude modulation via the modulation detection algorithm; frequency modulation was not significant. A representative time trace, along with its corresponding TFR, extracted AM signal, and its spectrum are shown in Fig. 5.4. The data shown in this figure are from a SDR telemetry experiment. We observed significant modulation frequency peaks at ~0.01 Hz which were derived by extracting AM magnitude values from the MYO (left bottom panels) and TGF (right bottom panels) frequency bands. The assertion of significance is based on the fact that the peaks in panels E and F exceed the critical threshold calculated with band-limited GWN (see methods).

Fig. 5.5 summarizes the results of the analyses of the telemetry data. The left and right columns show the detected AM results obtained from the MYO and TGF frequency bands, respectively. The top row shows the mean percentage of segments that exhibited significant AM. The middle row shows the average magnitude of the AM. The bottom row shows the averaged frequency associated with the detected AM. For both MYO and TGF frequency bands, the percentage of coupled segments are significantly higher ($p < 0.05$ as denoted by *) for SDR than SHR. Further, we observe a greater AM effect on TGF than MYO ($p < 0.05$ as denoted by #) in SHR. As shown in the middle panels, the magnitude of the AM effect on MYO and TGF was significantly greater ($P < 0.05$ as denoted by *) in SDR than SHR. The frequency of AM was found to be ~0.01 Hz in all cases.

For the acute data collected under isoflurane anesthesia, the presence of the ~0.01 Hz autoregulation component was only evident in the form of AM in the MYO frequency band. Further, the data from animals under inactin exhibited no significant AM or FM and are not shown. Fig. 5.6 shows comparison between acute experiments with isoflurane anesthetic and telemetry recordings in which there was clear AM of the MYO frequency band. Note that the two telemetry values are the same as on Fig. 5.5 and are included here to facilitate comparison. The results show that the AM magnitude in the MYO band for SDR telemetry recording was significantly different from the other conditions ($P <= 0.05$, denoted by *).

5.5 Discussion

In this study, we detected the presence of the low frequency (~0.01 Hz) component in spontaneous blood flow recordings from both conscious and unconscious normotensive and hypertensive rats. Specifically, we found evidence of LF that modulates the amplitudes of the MYO and TGF oscillations, which is consistent with significant interactions of these autoregulatory systems with a LF component. Further, we found a greater number of data segments that exhibit LF modulation of the TGF and MYO mechanisms in SDR than in SHR. In addition, the magnitude of the LF modulation of the MYO and TGF systems was greater in SDR than in SHR with

telemetry recordings. With anesthetic agents, the magnitude of the LF modulation of the MYO and TGF components, when compared to telemetry recordings, was suppressed by isoflurane, and abolished by inactin. These observations were reinforced by separate experiments where a chirp forcing signal in BP was used to elicit resonant spectral peaks in the low frequency band. These results showed that there was, indeed, an active autoregulatory component in RBF in the low frequency range.

In previous studies, random blood pressure forcings were used to examine the dynamic properties of the renal autoregulation (75, 76). However, no LF components were observed in these studies. One possible explanation for this may be that in the past studies, the data segments were relatively short, which would limit the frequency resolution and, hence, the ability to resolve any LF component. In contrast, we analyzed much longer time records. Further, our chirp signal forcing was specifically designed to elicit BP fluctuations in the LF range, whereas a random forcing does not guarantee that BP fluctuations in the LF range are well represented. Thus, the chirp signal forcing is a more appropriate approach than random forcing to resolve LF components.

Work by Just and Arendshorst (57) identified a putative third renal autoregulatory mechanism with a response time and resonant frequency that coincides with the LF component we identified. Our approach to identification of the LF component is based on the hypothesis that if it does exists, it should interact with the MYO and TGF mechanisms. The support for our hypothesis stems from previous studies in which there is ample evidence of interactions between the MYO and TGF via experimental (101) and computational approaches (22, 95, 117). Further, a study by Sosnovtseva et al. found interactions between the MYO and TGF by searching for AM and FM phenomena between the two mechanisms using wavelet analysis (116). In the cardiovascular system, we found interactions between the sympathetic and parasympathetic nervous systems by obtaining evidence of AM and FM phenomena in heart rate variability signal (141). Thus, the presence of AM and FM phenomena in biological signals is ubiquitous, and this has led us to look for the presence of the LF oscillation in renal hemodynamics by these means.

Identification of the third mechanism in the study of Just and Arendshorst is based on time-domain measurements that examine the transition between steady-states in renal

blood flow elicited by step changes in blood pressure in rats under the influence of anesthesia (57). Our study differs from that of Just and Arendshorst (57) in several ways. First, identification of the LF component is not based on inducing step changes in blood pressure, but directly from the spontaneous recordings of RBF data. Thus, we were able to use telemetric data from conscious rats for our analysis. The results show that anesthetics significantly suppress the interaction of the LF component. Therefore, the use of conscious recording is important in assessing the true dynamics of the putative LF autoregulatory component. Second, our method involves discrimination of the LF component in both time and frequency domains by searching for the presence of AM or FM dynamics, not just time-domain analysis as was employed by Just and Arendshorst (57). We have previously shown that accurate identification of renal autoregulatory dynamics such as interactions between the MYO and TGF requires time-varying approaches (95). In addition, the AM or FM phenomena are often difficult to resolve partly because they are time-varying. Thus, our successful identification of AM was predicated on the use of one of the highest resolution time-frequency spectral techniques available (128). We have shown that our CDM time-frequency method performs better than the wavelet approach, and in some cases, it outperforms the parametric time-varying autoregressive model based spectrum (128).

It is important to note that the third mechanism of renal autoregulation proposed by Just and Arendshorst (57) and our two approaches leading to the detection of the LF (LF gain peak via chirp forcing and LF amplitude modulation of the MYO and TGF)in the present study operate on a similar time scales The use of a chirp signal as BP fluctuations resulted in a significant resonant gain peak centered at 0.01 Hz when we calculated the ratio between RBF and BP spectra. The gain magnitude values decreasing below 0 dB in Fig. 5.3 at frequencies lower than 0.01 Hz is hallmark of dynamic autoregulation. Previous time-invariant (26, 75) and time-varying (24) transfer function analyses show such characteristics at the MYO and TGF frequency ranges, thereby leading to our assertion that they are autoregulatory mechanisms. The LF component detected via AM phenomenon being related to the possible third autoregulatory mechanism is less direct than the chirp signal forcing experiment. However, having found evidence of interactions between LF to both TGF and MYO, and the fact that this

LF is identical to the frequency of the resonant gain peak, we can surmise that 0.01 Hz detection via the AM is also related to the autoregulatory dynamics. Although not shown, it should be noted that we also observed significant interactions between the MYO and TGF in the form of the latter mechanism amplitude and frequency modulating the former. This is not surprising, as previous studies have shown evidence of both AM and FM of the MYO by the TGF (118).

The results of the telemetry data show that the magnitude of AM is reduced in the SHR when compared to SDR. This finding is consistent with previous studies. Sosnovtseva et al. showed that synchronization between the two traditional modes of renal autoregulation is reduced in SHR (118). In our own laboratory, we also observed a decrease in coupling between the MYO and TGF mechanisms in SHR using a bispectrum approach (111). However, it is important to note that where the past studies showed evidence of frequency modulation, our study only detected a significant amplitude modulation. This may suggest that the slow modulation mechanism interacts with the two established modes of renal autoregulation differently.

The presence of FM of the LF on either TGF or MYO was not detected in this work. The presence of FM was searched by tracking frequencies associated with the significant amplitudes in the MYO and TGF frequency bands across time. As shown in Fig. 5.4, searching for the presence of FM is difficult in the MYO frequency band because frequencies tend to vacillate over time. To circumvent an objective selection of which frequency to select at each time point, we used a weighted frequency average technique as described in the Methods section. While we did not detect LF component frequency modulating either the MYO or TGF, we did find evidence of FM of the MYO by the TGF. This is in agreement with a previously reported study which also found such FM phenomenon using a double wavelet approach (116).

Fig. 5.6 shows that the use of isoflurane anesthetic reduced the magnitude of the low frequency modulation in the MYO frequency range. This is in general not surprising, as anesthetics tend to suppress physiological dynamics. Of more importance is the difference between isoflurane and inactin, where the presence of the LF modulation is abolished with inactin.

The time scale of the LF component also suggests possible involvement of ANG II (25). Resetting of autoregulation to operate at a new mean arterial pressure in response to sustained reductions of renal perfusion pressure has been shown to involve ANG II (114, 115). Certainly, ample evidence indicates that ANG II strongly influences the dynamics of TGF (12, 49, 82, 102). Thus, the fact that we observe AM of TGF by a LF component, and given that ANG II acts on a similar time scale (25), suggests that the LF phenomena we have identified may involve ANG II. Further studies will be needed to confirm this possibility.

In summary, the present study used two novel approaches to detect the presence of a low frequency component in RBF signals: 1) via a chirp signal forcing and 2) via a signal processing approach in which we specifically searched for the presence of the LF component by quantifying its effect to modulate the amplitude of oscillations of the TGF and MYO mechanisms. Our results suggest that one discriminator between the SHR and SDR is the lower magnitude of amplitude modulation with the latter. We see that isoflurane diminished the magnitude of the LF component whereas inactin abolished our detection of either the AM or FM phenomenon of the LF component. Our transfer function analysis of chirp signal data yielded a resonant peak centered at 0.01 Hz that is greater than 0 dB, whereas at lower frequencies the transfer function gain diminished to smaller than 0 dB, providing direct evidence of the LF being one of the autoregulatory mechanisms. Further, our detection via the AM approach of interactions between the LF component and both TGF and MYO, with the LF component having an identical frequency to that of the resonant gain peak, provides more evidence that 0.01 Hz oscillations may represent the third autoregulatory mechanism.

This work has been submitted for review to American Journal of Physiology, Renal Physiology.

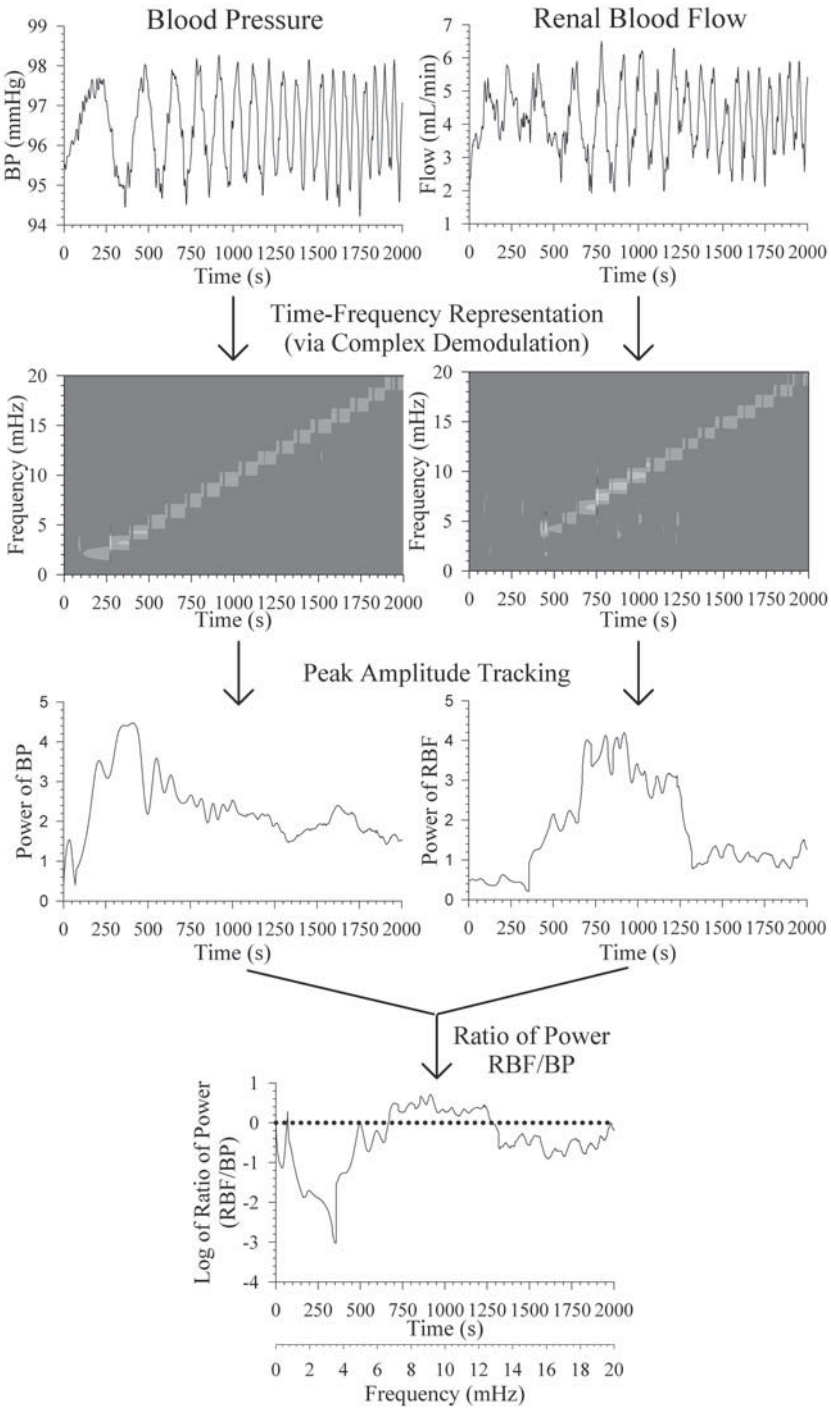

Figure 5.1 – Flow chart showing the data analysis procedures used for the chirp forcing experiment (n=5). The top row shows the representative blood flow data. The second row shows the time-varying spectrums calculated via complex demodulation method. The third row shows time traces of the peak amplitude across time for each spectrum. The bottom panel shows the ratio between the two amplitude tracking time traces. The dotted line in the bottom panel shows the threshold of zero, where ratios above zero indicates the presence of a resonant component.

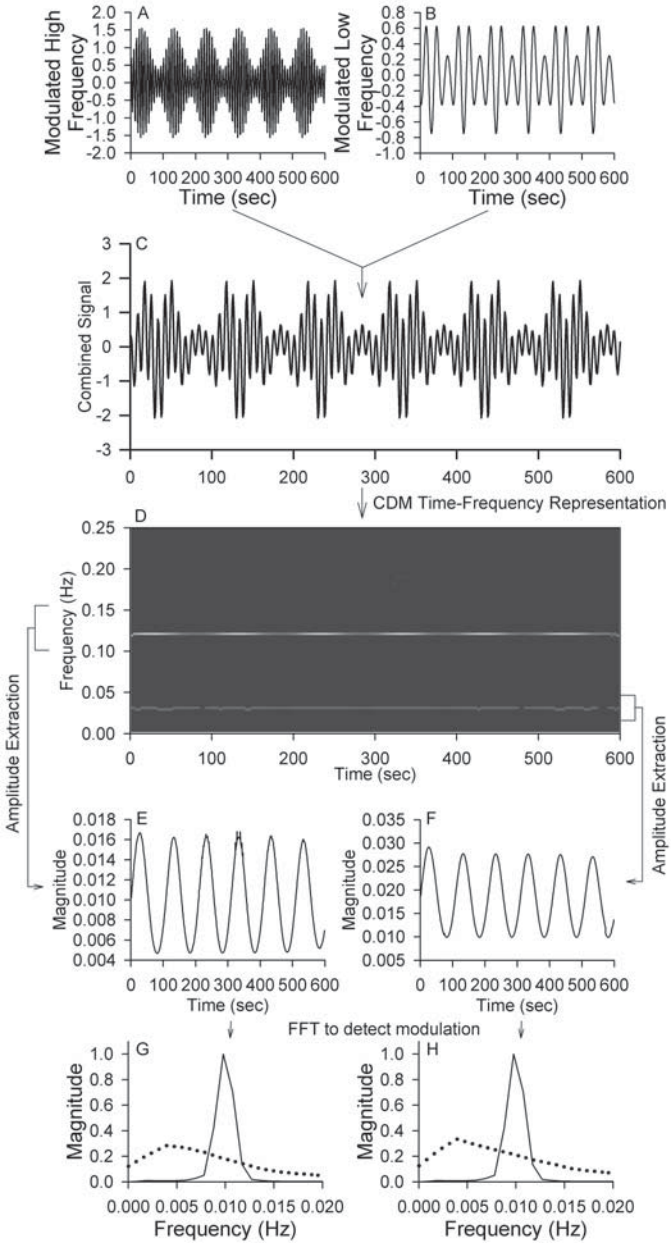

Figure 5.2 – Flowchart of the amplitude modulation detection algorithm using simulated data. Panels A and B shows two simulated signals amplitude modulated by a LF component. Panel C shows the summation of those two signals. This was done to simulate the conditions of the two renal autoregulatory mechanisms. Panel D shows the CDM time frequency representation of the simulated data in panel C. Panel E and F shows the average amplitude of the MYO and TGF frequency range across time, at 0.01-0.03 and 0.02-0.05 Hz, respectively. Panels G and H are the FFT of the time traces from panels E and F, respectively, which shows the amplitude modulation peak. The dotted line in G and H shows the result from 1000 random simulations of Gaussian white noise which underwent the same algorithm. This shows the statistical threshold for significant amplitude modulation.

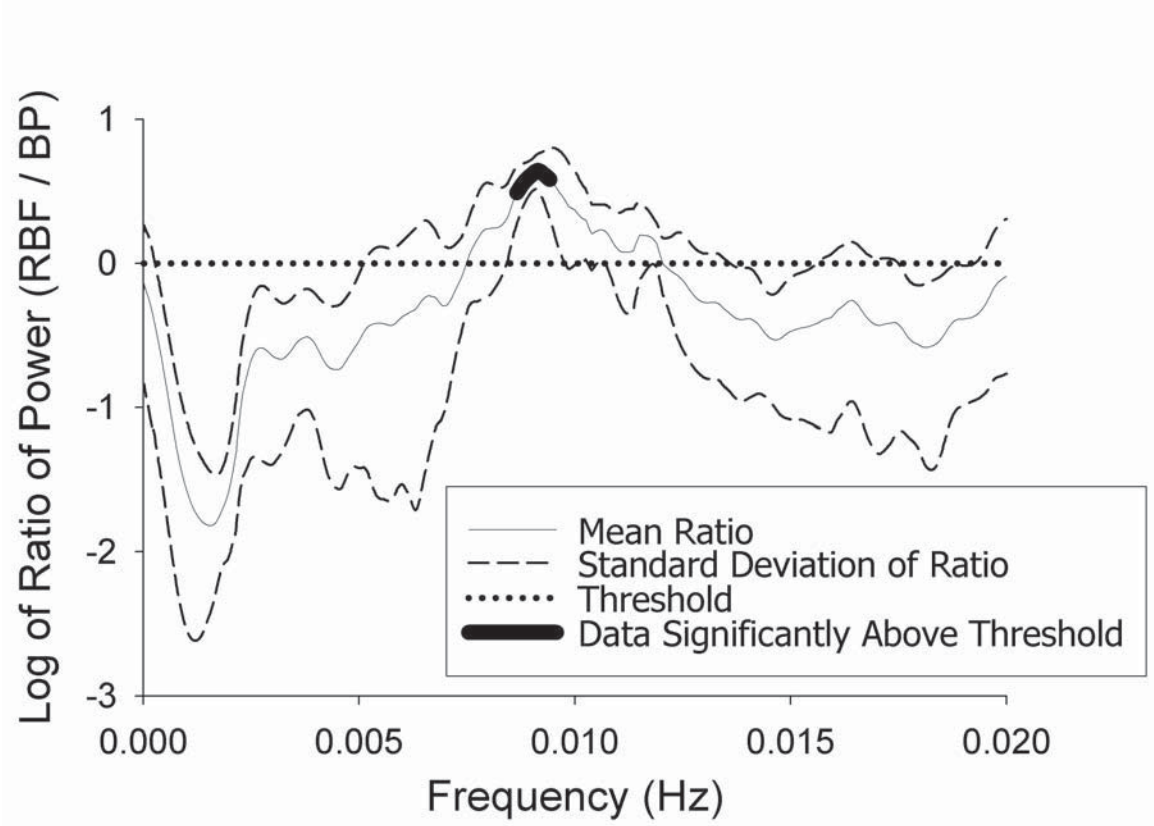

Figure 5.3 – Plot of the average of the ratio between the power of the RBF verses the BP, plotted in log scale (n=5). The solid line shows the mean of the 5 animals, while the dashed line shows the standard deviation. The dotted line shows the threshold of 0, where above this value indicates an active mechanism. The thick area in the mean ratio indicates statistical significant difference from the threshold line.

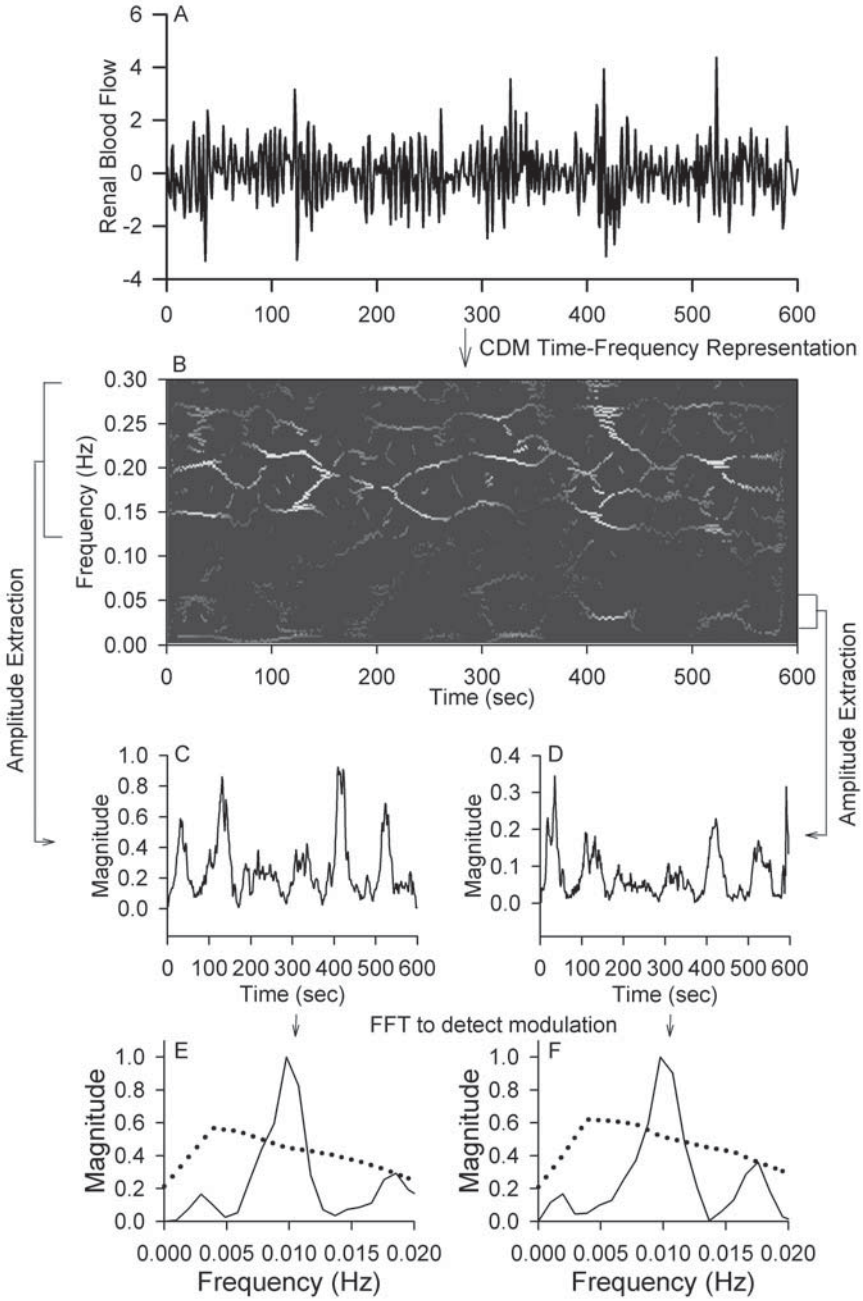

Figure 5.4 – Representative data set showing significant amplitude modulation. The particular data set shown is a recording from a telemetry experiment in an SDR. The calculation of the amplitude modulation is the same as that shown in figure 5.3.

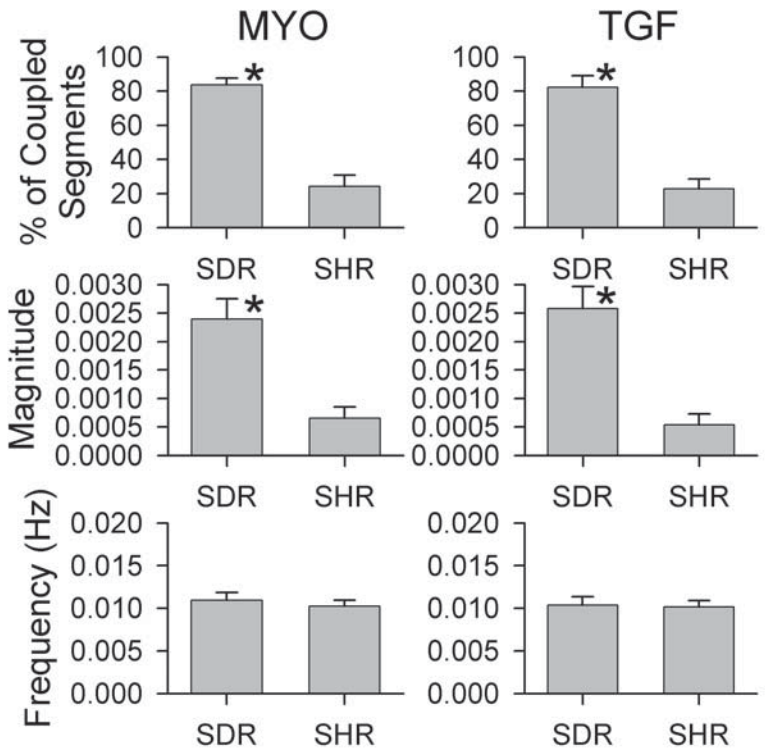

Figure 5.5 – Summary data for the telemetry experiments. Note that only the results for amplitude modulation are shown as frequency modulation was not found to be significant. Statistical significance between SDR and SHR is denoted by "*" (P<=0.05).

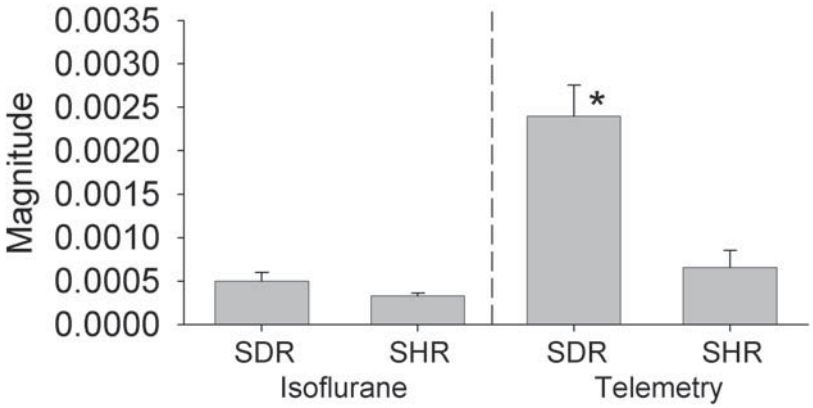

Figure 5.6 – Summary data from the acute experiments. Results from the telemetry experiments are also shown, to facilitate comparison. Note that only data from MYO amplitude modulation is shown, as TGF did not show significant modulation in acute experiments. Further, the results from inactin anesthetized animals are not shown as they were also not significant. The "*" denote data sets that were significantly different from all others.

Chapter 6

Electrohydraulic pump-driven closed-loop blood pressure regulatory system

6.1 ABSTRACT

In this work, a design for a new electrohydraulic (EH) pump-driven renal perfusion pressure (RPP) regulatory system capable of implementing precise and rapid RPP regulation in experimental animals is proposed. Without this automated system, RPP is manually controlled via a blood pressure clamp, and the imprecision in this method leads to compromised RPP data. This motivated us to develop an EH pump-driven closed-loop blood pressure regulatory system based on flow-mediated occlusion using the vascular occlusive cuff technique. A closed-loop servo-controller system based on a proportional plus integral (PI) controller was designed using the dynamic feedback RPP signal from animals. *In vivo* performance was evaluated via flow-mediated RPP occlusion, maintenance, and release responses during baseline and angiotensin II infused conditions. A step change of -30 mmHg, referenced to normal RPP, was applied to Sprague-Dawley rats with the proposed system to assess the performance of the PI controller. The PI's performance was compared against manual control of blood pressure clamp to regulate RPP. Rapid RPP occlusion (within 3 seconds) and a release time of approximately 0.3 seconds were obtained for the PI controller for both baseline and Ang II infusion conditions in which the former condition was significantly better than manual control. We concluded that the proposed EH RPP regulatory system could fulfill *in vivo* needs to study various pressure-flow relationships in diverse fields of physiology, in particular, studying the dynamics of the renal autoregulatory mechanisms.

6.2 INTRODUCTION

It is widely accepted that renal autoregulation plays a key role in maintaining relatively constant blood flow despite large variations in arterial pressure over many time scales (77). There are at least two mechanisms responsible for autoregulation (21, 46, 99), and recent works suggest a possible role of the third mechanism (56). The two

originally-recognized autoregulatory mechanisms, the myogenic mechanism (MYO) and tubuloglomerular feedback (TGF), have been extensively studied (17, 22, 46, 56, 63, 84, 104). The MYO is believed to respond to changes in wall tension induced by changes in local vascular pressures whereas TGF is governed by flow-rate dependent concentration changes in tubular fluid (17, 22, 46, 56, 63, 84, 104).

Understanding the kinetics and dynamic properties of autoregulatory mechanisms often requires the induction of a pressure step that is effectively instantaneous. This requirement is marginally met *in vitro* (3) with a feedback controller system but it has been a difficult feat to master under *in vivo* conditions. Obtaining results *in vivo* is the necessary precursor for telemetric recordings, which are the ultimate goal as it has been shown that anesthetics depress dynamics of the autoregulatory mechanisms (4).

Many attempts have been made to maintain renal perfusion pressure (RPP) in a desired pressure range and these include a pneumatic servo-control system (87), a bidirectional DC motor syringe pump system (41), and a unidirectional occlusive mechanical system (86). There are, however, limitations with these approaches as their effectiveness is reduced due to slow dynamic response, inaccurate maintenance of steady-state blood pressure fluctuations, and a bulky hardware system which precludes practical implementation for telemetric usage. A more recent study by Xia et al. (136) used a vascular occluder to servo control RPP in a telemetric setting. However, this system suffers from a slow (~45-50 seconds) response time to bring the increased RPP back to preset ranges, thus, making it less useful for evaluating renal autoregulatory dynamics.

To overcome the aforesaid limitations, we present the development of an electrohydraulic (EH) pump-driven closed-loop blood pressure regulatory system that can be used *in vivo*. The novelty in the EH pump system stems from the software developed, as it utilizes a commercially-available motor and data acquisition system. The controller software is a user-friendly monitoring program designed to be easily adapted to interested investigators' laboratories, and was programmed using a commercially-available software tool known as the Labview 8.0 program (National Instruments, Austin, TX, USA). The software is available free for interested investigators upon request. Our system can be adopted for telemetric use since we use an aortic occluder that is constructed entirely of silicon rubber. The system can occlude and release RPP in

approximately 3 seconds and 0.3 seconds respectively, and maintain desired RPP, based on the designed proportional and integral (PI) feedback controller. These response times indicate that this is a robust controller that results in a rapid step induction of blood pressure signals.

6.3 METHODS

6.3.1 Configuring the Electrohydraulic (EH) pump

We configured an electrohydraulic (EH) pump to maintain a desired RPP with minimum deviations as well as to deliver a step like change in RPP in a near instantaneous manner. The system consists of a commercially available EH peristaltic pump (LS brushless computer-programmable drive, Cole-Parmer Instrument Co., Vernon Hills, IL, USA) with double pump heads with each head having four rollers (LS Easy-Load II pump head 77201-60, Cole-Parmer Instrument Co., Vernon Hills, IL, USA). These double pump heads are directly coupled to a drive shaft which can rotate at speeds from 10 to 600 rpm. We used double Y pump tubing (L/S 16, ID=3.2 mm, Cole-Parmer Instrument Co., Vernon Hills, IL, USA) for generating hydraulic pressure, which allows rapid filling and emptying of the silicon occluder. The larger the size of the Y-tube, the faster the transfer of fluid to the occluder, but it should be noted that a consequence is greater difficulty in achieving fine adjustments. In this study, we selected the inner diameter of the Y-tube to be 3.2 mm because this allows the best compromise between delivering fluid in a relatively short time and still being able to make fine adjustments.

Panel A of Fig. 6.1 shows the EH configuration. The pump operation is activated by a monitor program we developed using the Labview 8.0 software tool. The communication between the EH pump and the software is via an RS-232C serial communication port located in the back of the EH pump. Occlusion of RPP is achieved by a mechanical vascular occluder (OC4, In Vivo Metric Co., Healdsburg, CA, USA) with the following specifications: cuff's width, thickness, and lumen diameter are 5 mm, 2 mm, and 4 mm, respectively. The double Y tubing described above is directly connected to the vascular occluder. It is our experience that the vascular occluder's cuff

must be inflated at least 50 mmHg more than the systolic pressure for complete occlusion.

The RPP signal was acquired using an analog-to-digital converter (DT9800 series, Data Translation Inc., Marlboro, MA, USA) controlled by the Labview program. The sampling time of the A/D converter was 5 ms. The Labview program was implemented on a computer running the Windows XP operating system.

6.3.2 Proportional plus Integral (PI) Controller Design

The PI controller to decrease, maintain and release the RPP at a predetermined pressure level using the EH pump motor was implemented in Labview 8.0. The PI controller is a closed-loop feedback system which is designed to track the desired reference signal in near real time and with a minimum amount of error at each time step. In general, the proportional controller is designed to provide a fast and large step compensation to achieve the desired level based on the reference signal. The integral controller is the fine tuner system designed to eliminate an offset error caused by the over- or under-shooting of the desired pressure level caused by the proportional controller. Without the integral controller, the offset error cannot be eliminated. Thus, the integral controller is a slow process and this fine tuning process can lend itself to slow oscillations as it tries to minimize the tracking of the target error values.

Panel B of Fig. 6.1 illustrates how the PI controller can be used to control RPP based on the EH pump system. The RPP is the reference signal and subtraction of the output blood pressure (U(s)) signal produces an error signal (E(s)) which is essentially an input to the PI controller. Given the input and output signal, a continuous-time transfer function can be derived below for the PI controller:

$$\frac{U(s)}{E(s)} = K_P + \frac{K_I}{s} \qquad \text{(eq. 6.1)}$$

which can be simplified to:

$$U(s) = K_P \cdot \left(1 + \frac{K_I}{K_P} \cdot \frac{1}{s}\right) \cdot E(s) = K_P \cdot \omega_{PI} \cdot \left(\frac{s/\omega_{PI} + 1}{s}\right) \cdot E(s) \qquad \text{(eq. 6.2)}$$

Where $\omega_{PI} = \frac{K_I}{K_P}$ (expressed in radians/s). In these equations, K_p and K_I denote constant gain values associated with the proportional and integrator controller. The 1/s term can be implemented as an integrator. One problem with an integrator is that with time, this value increases to a large value which can lead to instability. Thus, we used an anti-windup algorithm with saturation value set at 200. Eq. (6.2) above needs to be discretized since we use an analog-to-digital converter to control the EH pump. The discretized version of Eq. (6.2) becomes:

$$U(z) = K_P \cdot \left(1 + \omega_{PI} \cdot \frac{T_{sample}}{z-1}\right) \cdot E(z) = \frac{K_P z + K_P \cdot (\omega_{PI} \cdot T_{sample} - 1)}{z-1} E(z) \quad \text{(eq. 6.3)}$$

where T is the sampling time of the PI controller and it is limited by the 4800 baud rate of the serial communication of the EH motor. Equation (6.3) can be further modified to a difference equation form:

$$U_{k+1} = K_P \cdot E_{k+1} + K_P \cdot (\omega_{PI} \cdot T_{sample} - 1) \cdot E_k + U_k \quad \text{(eq. 6.4)}$$

The unknown gains, K_p and K_I (note $\omega_{PI} = \frac{K_I}{K_P}$) were tuned using the Ziegler-Nichols criteria to reduce oscillatory effects and yet generate an appropriately fast reactive pump motor speed. Using a series of animal experiments, the following parameters were derived:

$K_P = 3$, $K_I = 30$

where $\omega_{PI} = 0.1\ rad/s$ $= K_I/K_p$ and $T_{sample} = 10ms$, which was based on the baud rate of the serial communication board of the EH motor.

6.3.3 Animal preparation for an in vivo performance evaluation

We performed a series of experiments on 10 male Sprague-Dawley rats, weighing 200 to 300 g, in accordance with the guidelines and practices established for the care and use of research animals at the State University of New York at Stony Brook. The rats were initially anesthetized with 3% isoflurane anesthesia and their body temperature was maintained at 37 ^{o}C by placing the animals on a temperature-controlled surgery table. We cannulated the trachea, and a stream of 50/50 oxygen/nitrogen mix flowed into their

tracheal tube mixed with 1% isoflurane throughout the experiment to maintain the anesthetic state. The right femoral artery was catheterized (PE-50) for the measurement of hind limb pressure, which is reflective of the RPP. An incision was made on the left flank. The hydraulic vascular occluder was placed around the supra-renal aorta. In some experiments, an ultrasonic flow probe (Transonic Systems, Inc., Ithaca, NY, series 1PR) was placed around the left renal artery for the measurement of renal blood flow (RBF). Measurements began 1 hour after completion of surgery to allow for the recovery from post-surgical stress.

6.3.4 Experimental protocol

In the first set of experiments, the efficacy of the PI controller was compared to manual control (n=5). RPP was first clamped approximately 30 mmHg below baseline levels for 1 minute, after which the clamp was rapidly released. After release, the animal was allowed to recover for 5 minutes. Typical time traces of the RPP for this clamping protocol are shown in Fig. 6.3. This clamp and release process was repeated for a total of 3 trials. After the trials, the occluder was connected to a water filled syringe for manually controlled hand clamps. This protocol is similar to the PI controlled clamps except that the clamping was controlled manually by a syringe. A series of 3 clamps were also performed.

Fig. 6.2 shows a user interface programmed using the Labview tool. The result is a user-friendly application in which the operator inputs a desired reduction in the RPP values and then the software automatically adjusts the pressure using the PI controller. In addition, there are some useful real-time data analysis capabilities including filtering of the data as well as estimation of the power spectrum.

A second set of experiments were performed to assess the system's ability to function at different RPP set points (n=5). The protocol is similar to the first set of experiments except that manually controlled clamps were not performed. After a baseline measurement of 3 PI controlled clamps, angiotensin II (Ang II, Sigma-Aldrich, St. Louis, MO, 30 ng kg^{-1} min^{-1}) mixed with 2% albumin and saline solution was infused into the femoral vein to raise baseline RPP. After allowing the RPP and RBF to stabilize

(~10 minutes), a second series of 3 PI controlled clamps were performed. Ang II infusion was terminated after this second series of clamps and RPP was allowed to return to baseline levels.

To further test the system's ability to maintain steady RPP despite pharmacological manipulations to alter RPP, the PI controller was set and engaged at baseline RPP levels, Ang II was then infused into the animal at the previous flow rate in an attempt to raise RPP. This response was compared with the Ang II response without engaging the PI controller.

6.3.5 Data analysis

The collected data was low-pass filtered at 0.5 Hz to remove the cardiac signal from the time traces before analysis.

For each clamp, the linear slope and the standard deviation of the RPP fluctuations during the maintenance phase of the PI controller were calculated. Further, the times for the blood pressure to reach desired blood pressure levels as well as the time to reach baseline values were recorded. Trials for each animal for both the PI controller and manual clamping methods were averaged for comparison. Variance was compared using Levene's test for equality of variances.

Renal autoregulatory compensation parameters were calculated from RBF for each RPP clamp session. The top and bottom panels of Fig. 6.4 show typical RBF clamp response time traces under baseline and Ang II infusion conditions, respectively. Note that the RBF traces were plotted as a percent, where 100 percent is the mean baseline RBF level. This was done to facilitate comparison between animals and two conditions. This figure has been annotated to detail approaches we have used to calculate various renal autoregulatory compensatory parameters. Four autoregulatory compensatory parameters were calculated from each trace: percent MYO compensation from the clamp release, percent MYO compensation from the clamp engagement, slope of the slower clamp response, and percent compensation of the slower component. The percent MYO compensation from the clamp release was defined as the MYO release response divided by the complete release compensation, then multiplied by 100. The percent MYO

compensation from the clamp engagement is defined as the MYO clamp response divided by the complete clamp compensation, then multiplied by 100. The slope of the slower clamp response was defined as the linear slope between the points immediately after the MYO clamp response to immediately before the clamp release. Finally, the percent compensation of the slower component was defined as the slow clamp response divided by the complete clamp compensation, and then multiplied by 100.

The statistical significance for the averaged data was obtained using the student's t-test or the Mann-Whitney rank sum test when the data did not have equal variance. Difference in variance was tested using the Levenne's test for equal variance. The paired t-test was used for comparison between baseline and Ang II infused data from the same animals. In all cases, the statistical significance was set to P<=0.05.

6.4 RESULTS

Table 6.1 summarizes the RPP and RBF values for the animals. The numbers are reported as mean ± standard error.

Fig. 6.3 shows representative RPP time traces for the different clamping methods. The top panel shows a clamping trial using the PI controller. The middle and bottom panels show two different manually clamped results. The middle panel is an instance where the RPP was clamped to the desired pressure level at the first drop. The bottom panel shows an over-clamped trial followed by subsequent adjustments.

Summarized data of RPP from the experiments comparing the performance of the PI controlled clamps verses the manually controlled clamps are shown in Fig. 6.5. Data are shown as the mean plus standard error across the 5 animals. Panel A shows the mean linear slope during the RPP maintenance phase of the clamp using the PI controller and manual approaches, which were -0.0094±0.005 and 0.277±0.064 mmHg/sec, respectively. Panel B shows the standard deviations of the signal RPP during the maintenance of RPP phase, which were 1.48±0.176 and 1.154±0.218 mmHg for the PI controlled and manual clamps, respectively. Panel C shows the times needed from the start of clamp to when the RPP attained the desired RPP level, which were 3.26±0.29 and 10.59±3.75 seconds for the PI controlled and manual clamps, respectively. Panel D

shows the times for the RPP to return to baseline levels after the release of the clamp, which were 0.24±0.05 and 0.28±0.04 seconds for the PI controlled and manual clamps, respectively. Significant difference in the mean or median and the variance (P<=0.05) were found between the slope and the time to desired RPP between the PI controller and the manual approach.

Although not shown, the same parameters that were measured in Fig. 6.5 were also measured in the second experiment for the comparison of Ang II infused animals. Comparison between baseline and Ang II infused animals showed no statistical significance (P>0.05). This shows that the PI controller performs consistently even with different RPP set points.

Fig. 6.6 shows the typical result for testing the PI controller's ability to compensate for increases in RPP from pharmacological manipulations. In this figure, Ang II infusion began at 0 minutes. Ang II infusion resulted in a quick rise in RPP within 1 minute to 170±3.70 mmHg and then slowly reached a steady-state within 10 minutes to 139±1.02 mmHg. This rise in RPP was not observed in the PI controlled trace. The results shown demonstrate that the system was able to compensate for relatively large, sudden increases in RPP. The standard deviation of the RPP for 2 minutes before and after the Ang II infusion was found to be insignificantly different (P>0.05), at 1.51±0.17 and 1.61±0.21 mmHg, respectively.

Summary results from the RBF data calculated according to Fig 6.4 between baseline and Ang II clamps are shown on Fig 6.7. Statistically significant difference was found in all cases (P<=0.05).

6.5 CONCLUSIONS

We demonstrated an effective and yet simple PI servo-controller that can quickly and automatically reduce RPP to desired levels, and maintain the pressure despite the opposing compensatory effects. The PI controller was designed to send fluid as quickly as possible to the vascular occluder cuff using an EH pump motor and then fine tune itself to maintain the desired pressure. Using the LabVIEW tool, we designed a user friendly interface in which the operator simply inputs the desired pressure value with the

appropriate PI controller gain settings. The program has the ability to filter and estimate the power spectrum of the data in real time. The efficacy of this system was demonstrated by comparing the proposed PI controller to a person who already has had experience in manually controlling the blood pressure using a syringe. Our results indicate that the PI controller provided significantly faster time to a desired RPP level, and maintained its value with significantly less variation than human interventions. Further, the system was tested against RPP changes with Ang II infusion, and the results showed that the system performed consistently well even at different set points.

One of the key advantages of the proposed PI controlled system is the maintenance of the desired RPP, as demonstrated in the top panel of Fig. 6.3 and quantitatively illustrated in Fig 6.5A. As compared to human interventions to maintain the desired RPP, shown in the remaining panels of Fig. 6.3 and Fig. 6.5, the PI controller does a significantly better job. Even with human intervention, there is a monotonic increase in RPP, as shown in the two bottom panels of Fig. 6.5, and quantitatively illustrated as a rise in slope value as compared to no rise in slope with the PI controller in Fig. 6.5A.

The maintenance of the steady RPP levels during the pressure clamp was achieved by the PI controller using small adjustments on the occluder. With many fine adjustments, there is a concern that they may lead to a greater variance in RPP fluctuation than in normal conditions. However, as shown in Fig. 6.5B, while the average standard deviation values of the PI controlled clamps were slightly larger than those of the manually-induced clamps, it was not found to be significantly different.

The variance of the time to desired RPP level was found to be significantly lower in the PI controlled clamps than with human intervention. This was mainly due to over-clamping and subsequent readjustment of the clamps via manual trials, as shown in the bottom panel of Fig. 6.3. It should be noted that the chance of overshooting the desired RPP decreased with experience. For the PI-controlled clamps, the speed to achieve the desired RPP was consistent across all animals.

Ang II infusion raised the RPP by a maximum of ~65 mmHg and steady state value by ~35 mmHg. Fig 6.6 shows that the proposed PI controller was able to fully compensate for this change with no significant change in the RBF's variance. Further,

RPP clamps performed under the effects of Ang II infusion also yielded no significant difference when compared to the baseline. Taken together, this shows that the PI controller system proposed in this work can operate under different physiological conditions.

The representative time traces of RBF clamping experiments shown in Fig. 6.4 shows that Ang II infusion shifted the distribution of renal autoregulation from a balance of MYO and TGF to a more MYO dominant behavior. This trend was further seen from the summary data in Fig. 6.7, where MYO compensation with Ang II infusion was higher than under baseline conditions. This is not surprising, as Ang II has been shown in the past to increase excitability of vessels (61). Of more interesting observation is the slower compensatory mechanism during step reduction in RPP. The slow rise in RBF has been noted in several other studies (70), but due to the use of manually controlled clamps, which is not able to curtail rise in RPP, it was difficult to ascertain if the rise was due to the RPP itself or the action of the autoregulatory mechanism. With the use of the PI controlled clamp, RPP was held at a constant level, therefore, we can rule out the possibility of RPP. Thus, the slow rise is most likely the action of the TGF.

A previous study by Xia et al. (136) made use of an automatic RPP control system. The response time for that system was approximately 45-50 seconds. Further, because the system does not utilize a robust feedback controller, initial 1-2 minutes of the controller results in wide variations in RPP. For characterizing renal autoregulatory dynamics where fast control of RRP is required, the controller by Xia et al. (17) would not be applicable. However, this system is useful for studies that involve the control of RPP for long duration experiments (e.g., telemetry applications).

Although this study was performed in non-survival conditions, the occluder used is biocompatible and could be theoretically implanted and used in telemetric survival studies. This PI controller-based occluder has the potential to be especially useful in the application of renal autoregulation studies, where one could take advantage of the fast response time of this system to study the step response of the autoregulation system under the conscious state.

In conclusion, we have shown that the proposed PI controller offers advantages over the traditional manual clamps. They include consistency in the data and the ability

to adjust for small rises in RPP caused by physiological responses to abrupt drops in pressure. Altering the animal condition by the use of Ang II did not significantly alter the performance of the system, suggesting that it can perform under different physiological conditions.

This work has been submitted for review to American Journal of Physiology, Renal Physiology.

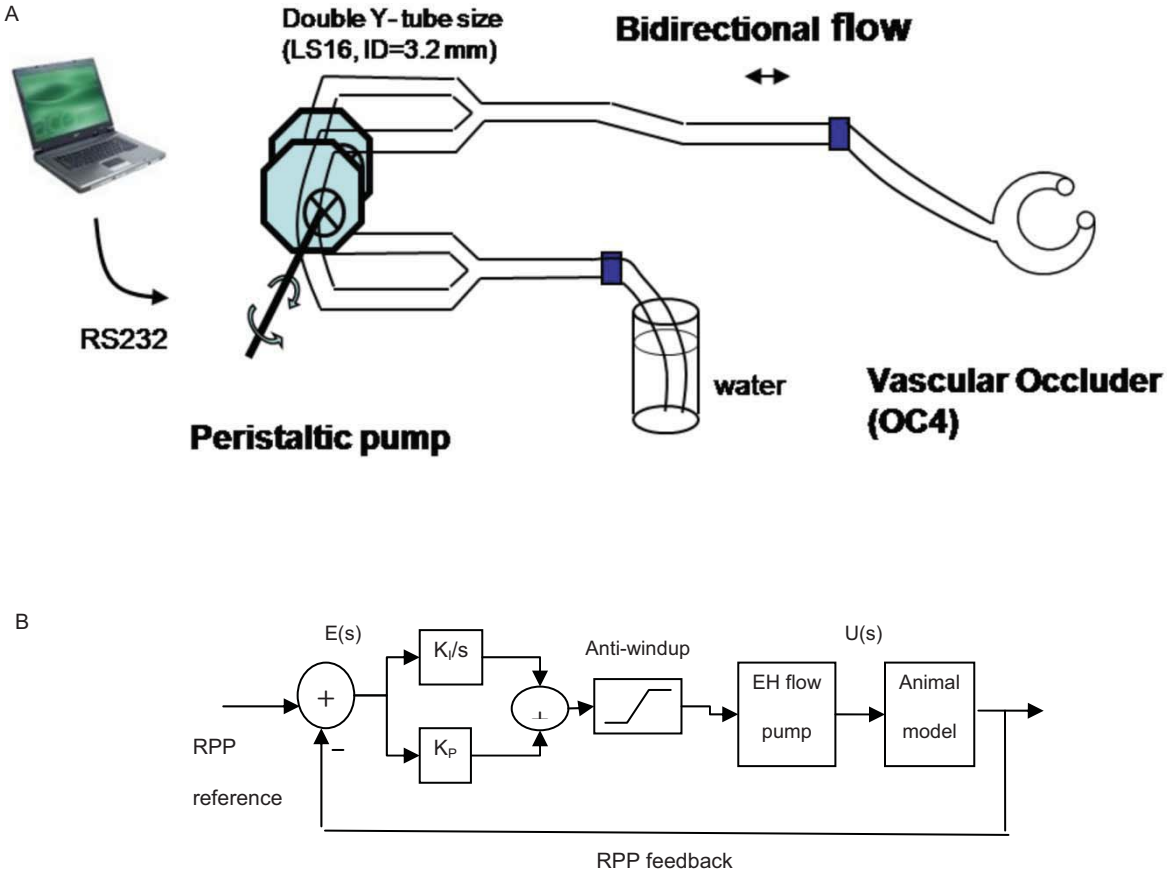

Figure 6.1 - Schematic diagram of the PI control system. Panel A shows the optimized electrohydraulic (EH) pump configuration. Panel B shows the diagram for the servo control system.

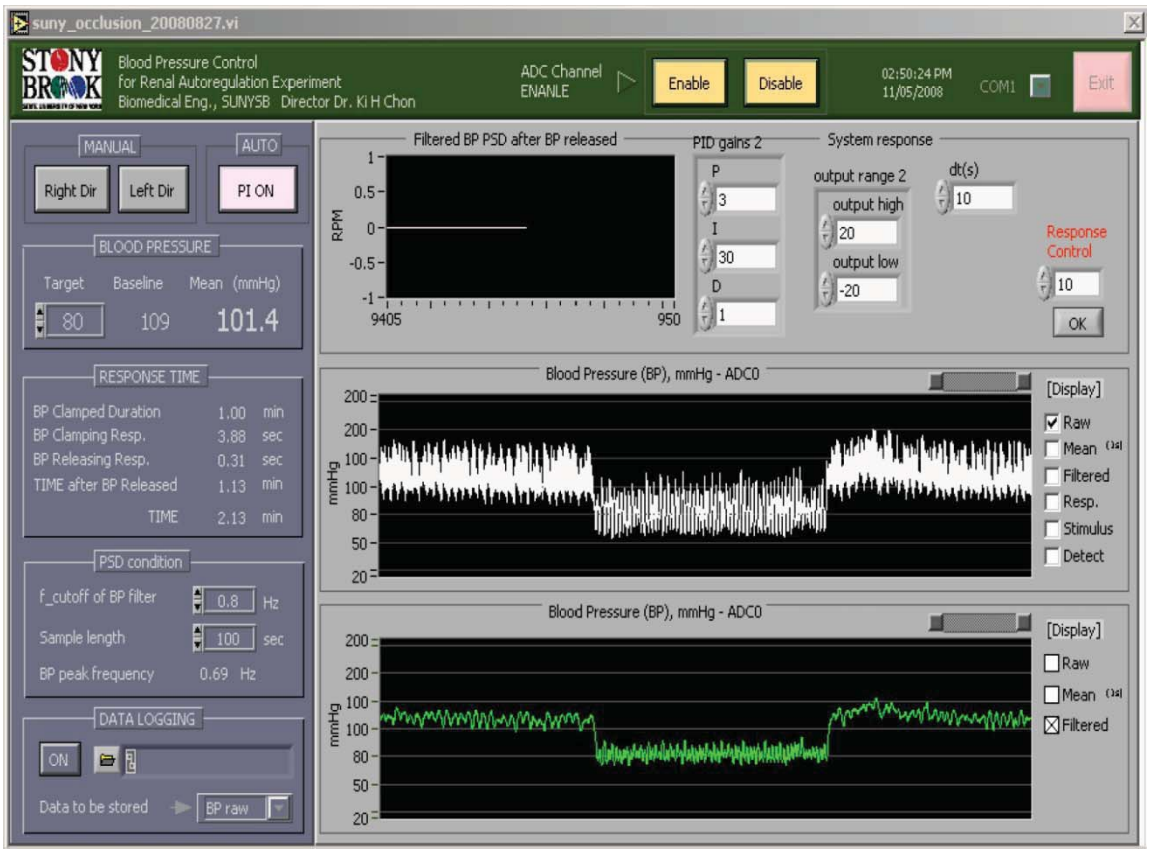

Figure 6.2 - A user-interface via Labview software. The input required is the target or desired RPP level in the upper left box.

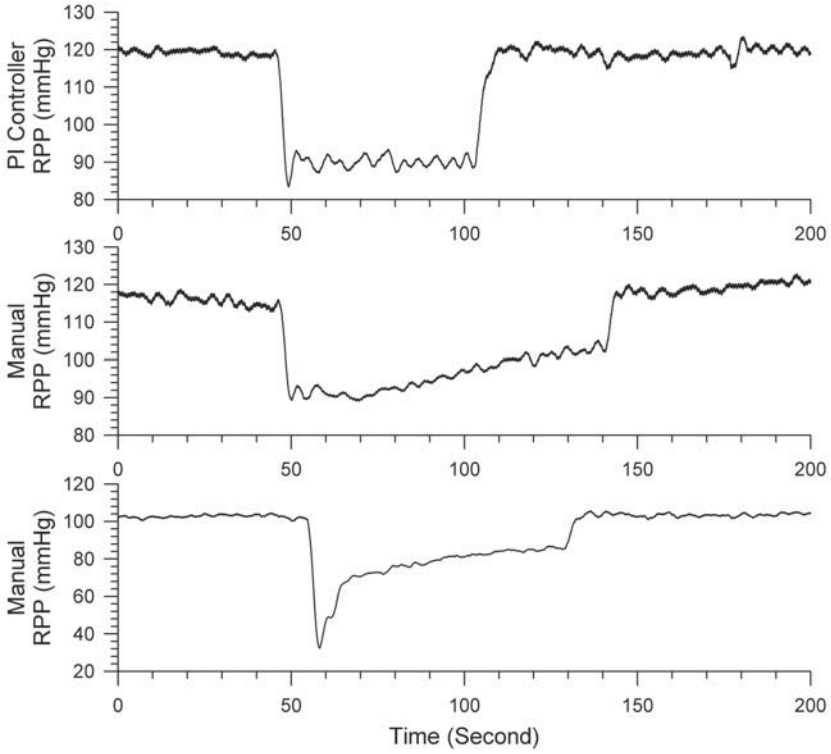

Figure 6.3. - Representative blood pressure data using the different clamp methods. The top panel shows the PI controlled clamp. The middle and bottom panels show two investigator-controlled clamps. The middle panel shows a clamp in which the clamp was successful on the initial clamp. The bottom panel shows a clamp in which there was initial overshoot, followed by a small release of the clamp to bring the blood pressure to desired levels.

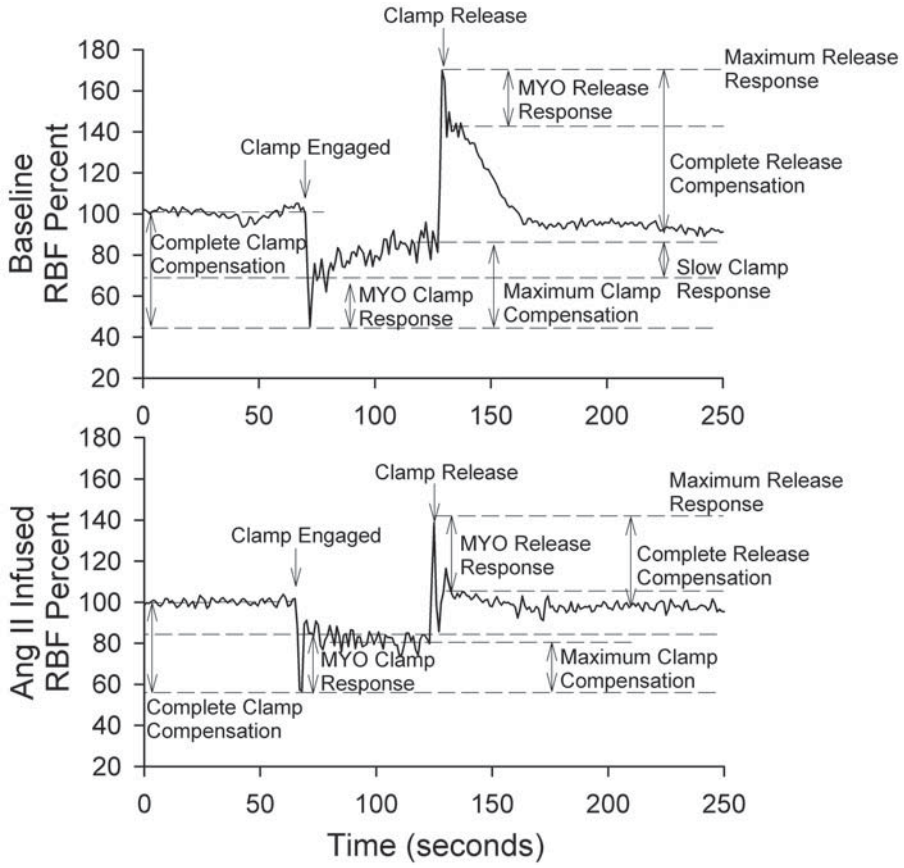

Figure 6.4 - Representative RBF traces are annotated to illustrate how autoregulatory compensation parameters are calculated.

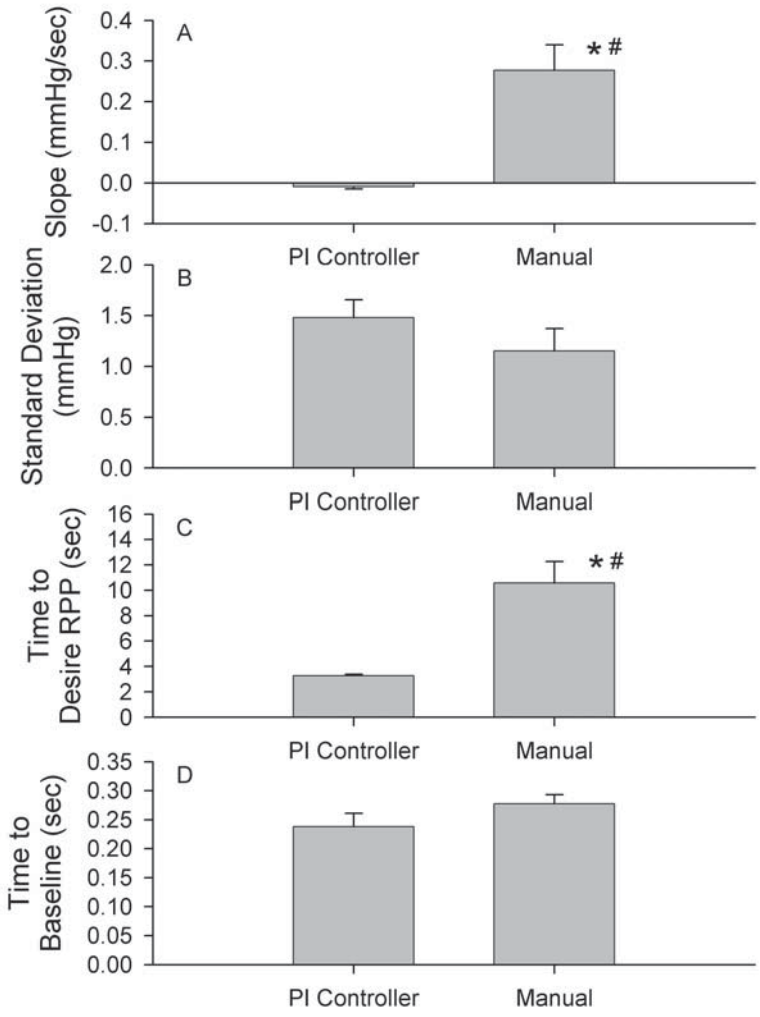

Figure 6.5 - Summarized data from the clamping experiments. Panel A shows the average linear slope during clamping. Panel B shows the standard deviation of the trace during clamping. Panel C shows the time needed to achieve the desired RPP level from the start of the clamp. Panel D shows the time needed for the RPP to return to baseline levels after release of occlusion. Data shown here as mean ± standard error.Statistical significance is indicated by "*". Statistically difference in variance is shown as "#".

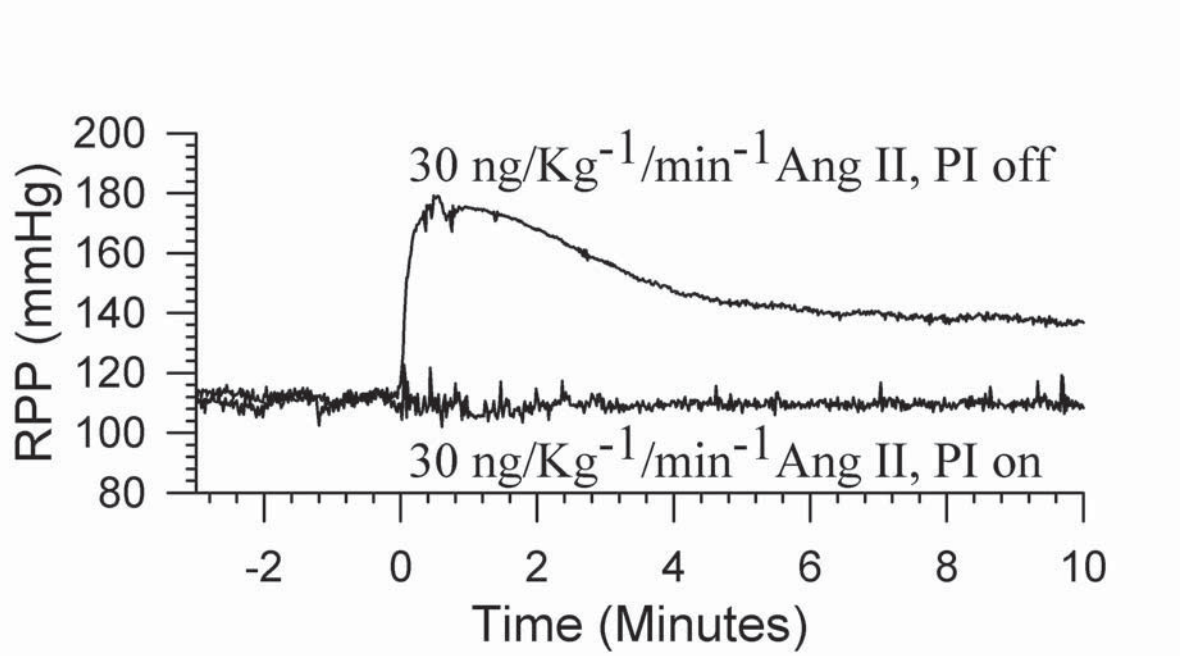

Figure 6.6 - Time traces showing the effect of the PI controller on Ang II infusion. Note that the RPP rise was abolished by the use of the PI controller (lower trace).

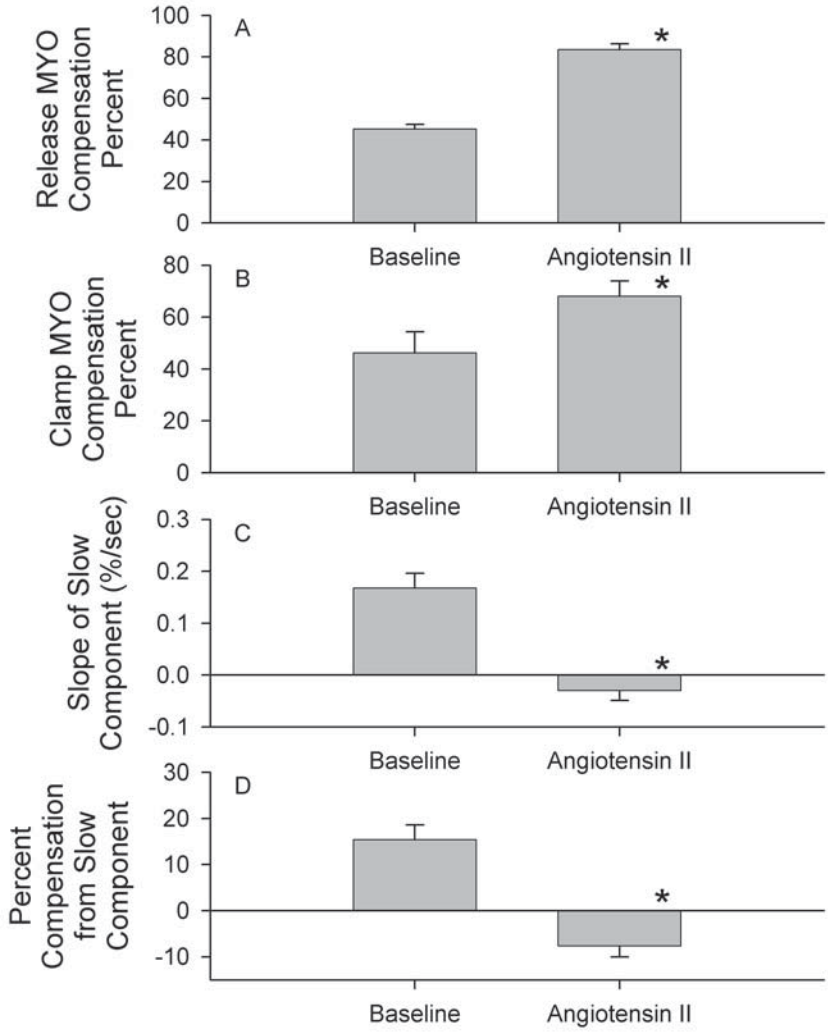

Figure 6.7 - Summarized RBF parameter data between baseline and Ang II infused animals. Panel A shows the percent of MYO compensation for the clamp release response. Panel B shows the percent of MYO compensation for the clamp engaged response. Panel C shows the slope of the slow component of RBF compensation during RPP clamping. Panel D shows the percent compensation from this slow component. Data shown as mean ± standard error. Statistical significance is indicated by "*" (P<=0.05).

Baseline RPP	Angiotensin II RPP Maximum	Angiotensin II RPP Steady	Baseline RBF	Angiotensin II RBF
105±2.87 mmHg	170±3.70 mmHg	139±1.02 mmHg	5.01±0.20 mL/min	1.49±0.137 mL/min

Table 6.1 - Average values for RPP and RBF under baseline and Ang II infusion.

Chapter 7
Conclusion

This work was designed to study the subtle characteristics of the renal autoregulatory system that previous works may have missed. Specifically, algorithms were designed to study the nonlinearity and time variance in the renal autoregulatory mechanisms. Further, a blood pressure control device was designed so that step responses can be used to study the renal autoregulatory system in a conscious, anesthetic free condition. The results show that rich nonlinear and time varying dynamics are present in the renal autoregulatory system. These results offer a more complete picture of renal autoregulation that was overlooked in the past. The differences that were observed between normotensive and hypertensive animals offers new insight into a disease that afflicts a large portions of the industrialized world. Further, the algorithms and techniques presented here are general techniques that can be adopted to be used in other fields of research.

BIBLIOGRAPHY

1. K/DOQI clinical practice guidelines on hypertension and antihypertensive agents in chronic kidney disease. *Am J Kidney Dis* 43: S1-290, 2004.
2. **Abu-Amarah I, Bidani AK, Hacioglu R, Williamson GA, and Griffin KA**. Differential effects of salt on renal hemodynamics and potential pressure transmission in stroke-prone and stroke-resistant spontaneously hypertensive rats. *Am J Physiol Renal Physiol* 289: F305-313, 2005.
3. **Ajikobi DO, and Cupples WA**. In vitro response of rat renal artery to perfusion pressure. *Canadian journal of physiology and pharmacology* 72: 794-800, 1994.
4. **Ajikobi DO, Novak P, Salevsky FC, and Cupples WA**. Pharmacological modulation of spontaneous renal blood flow dynamics. *Canadian journal of physiology and pharmacology* 74: 964-972, 1996.
5. **Al-Fahoum A, and Khadra L**. Combined Bispectral and Bicoherency approach for Catastrophic Arrhythmia Classification. *Conf Proc IEEE Eng Med Biol Soc* 1: 332-336, 2005.
6. **Bidani AK, and Griffin KA**. Long-term renal consequences of hypertension for normal and diseased kidneys. *Curr Opin Nephrol Hypertens* 11: 73-80, 2002.
7. **Bidani AK, and Griffin KA**. Pathophysiology of hypertensive renal damage: implications for therapy. *Hypertension* 44: 595-601, 2004.
8. **Bidani AK, Griffin KA, Picken M, and Lansky DM**. Continuous telemetric blood pressure monitoring and glomerular injury in the rat remnant kidney model. *Am J Physiol* 265: F391-398, 1993.
9. **Bidani AK, Hacioglu R, Abu-Amarah I, Williamson GA, Loutzenhiser R, and Griffin KA**. "Step" vs. "dynamic" autoregulation: implications for susceptibility to hypertensive injury. *Am J Physiol Renal Physiol* 285: F113-120, 2003.
10. **Bidani AK, Mitchell KD, Schwartz MM, Navar LG, and Lewis EJ**. Absence of glomerular injury or nephron loss in a normotensive rat remnant kidney model. *Kidney Int* 38: 28-38, 1990.
11. **Bidani AK, Schwartz MM, and Lewis EJ**. Renal autoregulation and vulnerability to hypertensive injury in remnant kidney. *Am J Physiol* 252: F1003-1010, 1987.
12. **Braam B, and Koomans HA**. Nitric oxide antagonizes the actions of angiotensin II to enhance tubuloglomerular feedback responsiveness. *Kidney Int* 48: 1406-1411, 1995.
13. **Briggs JP, and Schnermann J**. Hypertension: Pathophysiology, Diagnosis, and Management. In: *The tubuloglomerular feedback mechanism*, edited by JH L, and Brenner B. New York: Raven Press, 1995, p. 1359-1383.
14. **Bullock TH, Achimowicz JZ, Duckrow RB, Spencer SS, and Iragui-Madoz VJ**. Bicoherence of intracranial EEG in sleep, wakefulness and seizures. *Electroencephalogr Clin Neurophysiol* 103: 661-678, 1997.
15. **Carmines PK, Inscho EW, and Gensure RC**. Arterial pressure effects on preglomerular microvasculature of juxtamedullary nephrons. *Am J Physiol* 258: F94-102, 1990.
16. **Casellas D, and Moore LC**. Autoregulation and tubuloglomerular feedback in juxtamedullary glomerular arterioles. *Am J Physiol* 258: F660-669, 1990.
17. **Casellas D, and Moore LC**. Autoregulation and tubuloglomerular feedback in juxtamedullary glomerular arterioles. *Am J Physiol* 258: F660-F669, 1990.
18. **Casellas D, and Moore LC**. Autoregulation of intravascular pressure in preglomerular juxtamedullary vessels. *Am J Physiol* 264: F315-321, 1993.

19. **Chen YM, Yip KP, Marsh DJ, and Holstein-Rathlou NH**. Magnitude of TGF-initiated nephron-nephron interactions is increased in SHR. *Am J Physiol* 269: F198-204, 1995.
20. **Chobanian AV, Bakris GL, Black HR, Cushman WC, Green LA, Izzo JL, Jr., Jones DW, Materson BJ, Oparil S, Wright JT, Jr., and Roccella EJ**. Seventh report of the Joint National Committee on Prevention, Detection, Evaluation, and Treatment of High Blood Pressure. *Hypertension* 42: 1206-1252, 2003.
21. **Chon KH, Chen YM, Holstein-Rathlou NH, Marsh DJ, and Marmarelis VZ**. On the efficacy of linear system analysis of renal autoregulation in rats. *IEEE Trans Biomed Eng* 40: 8-20, 1993.
22. **Chon KH, Chen YM, Marmarelis VZ, Marsh DJ, and Holstein-Rathlou NH**. Detection of interactions between myogenic and TGF mechanisms using nonlinear analysis. *Am J Physiol* 267: F160-173, 1994.
23. **Chon KH, Raghavan R, Chen YM, Marsh DJ, and Yip KP**. Interactions of TGF-dependent and myogenic oscillations in tubular pressure. *Am J Physiol Renal Physiol* 288: F298-307, 2005.
24. **Chon KH, Zhong Y, Moore LC, Holstein-Rathlou NH, and Cupples WA**. Analysis of nonstationarity in renal autoregulation mechanisms using time-varying transfer and coherence functions. *Am J Physiol Regul Integr Comp Physiol* 295: R821-828, 2008.
25. **Cupples WA**. Angiotensin II conditions the slow component of autoregulation of renal blood flow. *Am J Physiol* 264: F515-522, 1993.
26. **Cupples WA, and Braam B**. Assessment of renal autoregulation. *Am J Physiol Renal Physiol* 292: F1105-1123, 2007.
27. **Cupples WA, and Loutzenhiser RD**. Dynamic autoregulation in the in vitro perfused hydronephrotic rat kidney. *Am J Physiol* 275: F126-130, 1998.
28. **Cupples WA, Novak P, Novak V, and Salevsky FC**. Spontaneous blood pressure fluctuations and renal blood flow dynamics. *Am J Physiol* 270: F82-89, 1996.
29. **Cupples WA, Wexler AS, and Marsh DJ**. Model of TGF-proximal tubule interactions in renal autoregulation. *Am J Physiol* 259: F715-726, 1990.
30. **Daniels FH, and Arendshorst WJ**. Tubuloglomerular feedback kinetics in spontaneously hypertensive and Wistar-Kyoto rats. *Am J Physiol* 259: F529-534, 1990.
31. **Davis MJ, and Hill MA**. Signaling mechanisms underlying the vascular myogenic response. *Physiol Rev* 79: 387-423, 1999.
32. **Duchin KL, Peterson LN, and Burke TJ**. Effect of furosemide on renal autoregulation. *Kidney Int* 12: 379-386, 1977.
33. **Elgar S, and Guza RT**. Statistics of Bicoherence. *IEEE Trans on Acoustics, Speech and Signal Processing* 36: 1667-1668, 1988.
34. **Feng L, Siu K, Moore LC, Marsh DJ, and Chon KH**. A robust method for detection of linear and nonlinear interactions: application to renal blood flow dynamics. *Ann Biomed Eng* 34: 339-353, 2006.
35. **Griffin KA, Hacioglu R, Abu-Amarah I, Loutzenhiser R, Williamson GA, and Bidani AK**. Effects of calcium channel blockers on "dynamic" and "steady-state step" renal autoregulation. *Am J Physiol Renal Physiol* 286: F1136-1143, 2004.
36. **Harder DR, Gilbert R, and Lombard JH**. Vascular muscle cell depolarization and activation in renal arteries on elevation of transmural pressure. *Am J Physiol* 253: F778-781, 1987.
37. **Harrison-Bernard LM, and Navar LG**. Renal cortical and medullary microvascular blood flow autoregulation in rat. *Kidney Int Suppl* 57: S23-29, 1996.
38. **Harsing L, Fonyodi S, Kabat M, and Kover G**. Effect of phlorizin and of mercurial diuretics on renal haemodynamics. *Acta Physiol Hung* 12: 363-371, 1957.

39. **Hayashi K, Epstein M, and Loutzenhiser R**. Pressure-induced vasoconstriction of renal microvessels in normotensive and hypertensive rats. Studies in the isolated perfused hydronephrotic kidney. *Circ Res* 65: 1475-1484, 1989.
40. **Hegger R, Kantz H, and Schreiber T**. Practical implementation of nonlinear time series methods: The TISEAN package. *Chaos* 9: 413-435, 1999.
41. **Hester RL, Granger JP, Williams J, and Hall JE**. Acute and chronic servo-control of renal perfusion pressure. *The American journal of physiology* 244: F455-460, 1983.
42. **Heyeraas KJ, and Aukland K**. Interlobular arterial resistance: influence of renal arterial pressure and angiotensin II. *Kidney Int* 31: 1291-1298, 1987.
43. **Holstein-Rathlou NH, He J, Wagner AJ, and Marsh DJ**. Patterns of blood pressure variability in normotensive and hypertensive rats. *Am J Physiol* 269: R1230-1239, 1995.
44. **Holstein-Rathlou NH, and Leyssac PP**. TGF-mediated oscillations in the proximal intratubular pressure: differences between spontaneously hypertensive rats and Wistar-Kyoto rats. *Acta Physiol Scand* 126: 333-339, 1986.
45. **Holstein-Rathlou NH, and Marsh DJ**. Renal blood flow regulation and arterial pressure fluctuations: a case study in nonlinear dynamics. *Physiol Rev* 74: 637-681, 1994.
46. **Holstein-Rathlou NH, Wagner AJ, and Marsh DJ**. Tubuloglomerular feedback dynamics and renal blood flow autoregulation in rats. *Am J Physiol* 260: F53-F68, 1991.
47. **Holstein-Rathlou NH, Wagner AJ, and Marsh DJ**. Tubuloglomerular feedback dynamics and renal blood flow autoregulation in rats. *Am J Physiol* 260: F53-68, 1991.
48. **Huang L, Wang Y, Liu J, and Wang J**. Evaluation of ischemic states using bispectrum parameters of EEG and neural networks. *Conf Proc IEEE Eng Med Biol Soc* 1: 582-585, 2004.
49. **Huang WC, and Navar LG**. Tubuloglomerular feedback-dependent influence of angiotensin II on the kidney in rats. *Proc Natl Sci Counc Repub China B* 12: 180-185, 1988.
50. **Inscho EW**. P2 receptors in regulation of renal microvascular function. *Am J Physiol Renal Physiol* 280: F927-944, 2001.
51. **Inscho EW, Cook AK, and Navar LG**. Pressure-mediated vasoconstriction of juxtamedullary afferent arterioles involves P2-purinoceptor activation. *Am J Physiol* 271: F1077-1085, 1996.
52. **Iversen BM, Amann K, Kvam FI, Wang X, and Ofstad J**. Increased glomerular capillary pressure and size mediate glomerulosclerosis in SHR juxtamedullary cortex. *Am J Physiol* 274: F365-373, 1998.
53. **Jamsek J, Stefanovska A, and McClintock PV**. Nonlinear cardio-respiratory interactions revealed by time-phase bispectral analysis. *Phys Med Biol* 49: 4407-4425, 2004.
54. **Johnson PC**. Autoregulation of blood flow. *Circ Res* 59: 483-495, 1986.
55. **Juncos LA, Garvin J, Carretero OA, and Ito S**. Flow modulates myogenic responses in isolated microperfused rabbit afferent arterioles via endothelium-derived nitric oxide. *J Clin Invest* 95: 2741-2748, 1995.
56. **Just A**. Mechanisms of renal blood flow autoregulation: dynamics and contributions. *Am J Physiol Regul Integr Comp Physiol* 292: R1-17, 2007.
57. **Just A, and Arendshorst WJ**. Dynamics and contribution of mechanisms mediating renal blood flow autoregulation. *Am J Physiol Regul Integr Comp Physiol* 285: R619-631, 2003.
58. **Just A, and Arendshorst WJ**. Nitric oxide blunts myogenic autoregulation in rat renal but not skeletal muscle circulation via tubuloglomerular feedback. *J Physiol* 569: 959-974, 2005.
59. **Just A, and Arendshorst WJ**. A novel mechanism of renal blood flow autoregulation and the autoregulatory role of A1 adenosine receptors in mice. *Am J Physiol Renal Physiol* 293: F1489-1500, 2007.

60. **Just A, Ehmke H, Toktomambetova L, and Kirchheim HR**. Dynamic characteristics and underlying mechanisms of renal blood flow autoregulation in the conscious dog. *Am J Physiol Renal Physiol* 280: F1062-1071, 2001.
61. **Just A, Ehmke H, Wittmann U, and Kirchheim HR**. Role of angiotensin II in dynamic renal blood flow autoregulation of the conscious dog. *The Journal of physiology* 538: 167-177, 2002.
62. **Just A, Ehmke H, Wittmann U, and Kirchheim HR**. Tonic and phasic influences of nitric oxide on renal blood flow autoregulation in conscious dogs. *Am J Physiol* 276: F442-449, 1999.
63. **Just A, Wittmann U, Ehmke H, and Kirchheim HR**. Autoregulation of renal blood flow in the conscious dog and the contribution of the tubuloglomerular feedback. *J Physiol* 506 (Pt 1): 275-290, 1998.
64. **Kallskog O, and Marsh DJ**. TGF-initiated vascular interactions between adjacent nephrons in the rat kidney. *Am J Physiol* 259: F60-64, 1990.
65. **Kantz H**. A robust method to estimate the maximal Lyapunov exponent of a time series. *Phys Lett A* 185: 77, 1994.
66. **Karlsen FM, Andersen CB, Leyssac PP, and Holstein-Rathlou NH**. Dynamic autoregulation and renal injury in Dahl rats. *Hypertension* 30: 975-983, 1997.
67. **Komlosi P, Fintha A, and Bell PD**. Renal cell-to-cell communication via extracellular ATP. *Physiology (Bethesda)* 20: 86-90, 2005.
68. **Layton AT, Moore LC, and Layton HE**. Multistability in tubuloglomerular feedback and spectral complexity in spontaneously hypertensive rats. *Am J Physiol Renal Physiol* 291: F79-97, 2006.
69. **Leyssac PP, and Baumbach L**. An oscillating intratubular pressure response to alterations in Henle loop flow in the rat kidney. *Acta Physiol Scand* 117: 415-419, 1983.
70. **Loutzenhiser R, Bidani A, and Chilton L**. Renal myogenic response: kinetic attributes and physiological role. *Circ Res* 90: 1316-1324, 2002.
71. **Loutzenhiser R, Chilton L, and Trottier G**. Membrane potential measurements in renal afferent and efferent arterioles: actions of angiotensin II. *Am J Physiol* 273: F307-314, 1997.
72. **Loutzenhiser R, Griffin K, Williamson G, and Bidani A**. Renal autoregulation: new perspectives regarding the protective and regulatory roles of the underlying mechanisms. *Am J Physiol Regul Integr Comp Physiol* 290: R1153-1167, 2006.
73. **Mailloux LU**. Hypertension in chronic renal failure and ESRD: prevalence, pathophysiology, and outcomes. *Semin Nephrol* 21: 146-156, 2001.
74. **Majid DS, Inscho EW, and Navar LG**. P2 purinoceptor saturation by adenosine triphosphate impairs renal autoregulation in dogs. *J Am Soc Nephrol* 10: 492-498, 1999.
75. **Marmarelis VZ, Chon KH, Chen YM, Marsh DJ, and Holstein-Rathlou NH**. Nonlinear analysis of renal autoregulation under broadband forcing conditions. *Ann Biomed Eng* 21: 591-603, 1993.
76. **Marmarelis VZ, Chon KH, Holstein-Rathlou NH, and Marsh DJ**. Nonlinear analysis of renal autoregulation in rats using principal dynamic modes. *Ann Biomed Eng* 27: 23-31, 1999.
77. **Marsh DJ, Osborn JL, and Cowley AW, Jr.** 1/f fluctuations in arterial pressure and regulation of renal blood flow in dogs. *The American journal of physiology* 258: F1394-1400, 1990.
78. **Marsh DJ, Sosnovtseva OV, Chon KH, and Holstein-Rathlou NH**. Nonlinear interactions in renal blood flow regulation. *Am J Physiol Regul Integr Comp Physiol* 288: R1143-1159, 2005.
79. **Marsh DJ, Sosnovtseva OV, Pavlov AN, Yip KP, and Holstein-Rathlou NH**. Frequency encoding in renal blood flow regulation. *Am J Physiol Regul Integr Comp Physiol* 288: R1160-1167, 2005.

80. **Marsh DJ, Toma I, Sosnovtseva OV, Peti-Peterdi J, and Holstein-Rathlou NH**. Electrotonic vascular signal conduction and nephron synchronization. *Am J Physiol Renal Physiol* 2008.
81. **Mason J, Kain H, Welsch J, and Schnermann J**. The early phase of experimental acute renal failure. VI. The influence of furosemide. *Pflugers Arch* 392: 125-133, 1981.
82. **Mitchell KD, and Navar LG**. Enhanced tubuloglomerular feedback during peritubular infusions of angiotensins I and II. *Am J Physiol* 255: F383-390, 1988.
83. **Moore LC, and Casellas D**. Tubuloglomerular feedback dependence of autoregulation in rat juxtamedullary afferent arterioles. *Kidney Int* 37: 1402-1408, 1990.
84. **Moore LC, and Casellas D**. Tubuloglomerular feedback dependence of autoregulation in rat juxtamedullary afferent arterioles. *Kidney Int* 37: 1402-1408, 1990.
85. **Moore LC, Rich A, and Casellas D**. Ascending myogenic autoregulation: interactions between tubuloglomerular feedback and myogenic mechanisms. *Bull Math Biol* 56: 391-410, 1994.
86. **Morff RJ, and Granger HJ**. An inexpensive servo-control system for regulating microvascular perfusion pressures in small animals. *Microvascular research* 22: 367-371, 1981.
87. **Nafz B, Persson PB, Ehmke H, and Kirchheim HR**. A servo-control system for open- and closed-loop blood pressure regulation. *The American journal of physiology* 262: F320-325, 1992.
88. **Nikias CL, and Petropulu AP**. *Higher-order spectral analysis : a nonlinear signal processing framework*. Englewood Cliffs, N.J.: PTR Prentice Hall, 1993, p. xxii, 537.
89. **Ning T, and Bronzino JD**. Nonlinear analysis of the hippocampal subfields of CA1 and the dentate gyrus. *IEEE Trans Biomed Eng* 40: 870-876, 1993.
90. **Osswald H, Hermes HH, and Nabakowski G**. Role of adenosine in signal transmission of tubuloglomerular feedback. *Kidney Int Suppl* 12: S136-142, 1982.
91. **Ostchega Y, Yoon S, Hughes JP, and Louis T**. Hypertension awareness, treatment, and control -- continued disparities in adults: United States, 2005-2006. NCHS data brief no Hyattsville, MD: National Center for Health Statistics. 2008.
92. **Pfurtscheller G, Stancak A, Jr., and Edlinger G**. On the existence of different types of central beta rhythms below 30 Hz. *Electroencephalogr Clin Neurophysiol* 102: 316-325, 1997.
93. **Pinhas I, Toledo E, Aravot D, and Akselrod S**. Bicoherence analysis of new cardiovascular spectral components observed in heart-transplant patients: statistical approach for bicoherence thresholding. *IEEE Trans Biomed Eng* 51: 1774-1783, 2004.
94. **Pires SL, Barres C, Sassard J, and Julien C**. Renal blood flow dynamics and arterial pressure lability in the conscious rat. *Hypertension* 38: 147-152, 2001.
95. **Raghavan R, Chen X, Yip KP, Marsh DJ, and Chon KH**. Interactions between TGF-dependent and myogenic oscillations in tubular pressure and whole kidney blood flow in both SDR and SHR. *Am J Physiol Renal Physiol* 290: F720-732, 2006.
96. **Roustan JP, Valette S, Aubas P, Rondouin G, and Capdevila X**. Can electroencephalographic analysis be used to determine sedation levels in critically ill patients? *Anesth Analg* 101: 1141-1151, table of contents, 2005.
97. **Sanchez-Ferrer CF, Roman RJ, and Harder DR**. Pressure-dependent contraction of rat juxtamedullary afferent arterioles. *Circ Res* 64: 790-798, 1989.
98. **Schack B, Vath N, Petsche H, Geissler HG, and Moller E**. Phase-coupling of theta-gamma EEG rhythms during short-term memory processing. *Int J Psychophysiol* 44: 143-163, 2002.
99. **Schnerman JaBJ**. Function of the Juxtaglomerular Apparatus: control of glomerular hemodynamics and renin secretion. . In: *The Kidney: Physiology & Pathophysiology*, edited by G SDaG. New York: Raven Press, 1992, p. 1053-1068.

100. **Schnermann J, and Briggs J**. Concentration-dependent sodium chloride transport as the signal in feedback control of glomerular filtration rate. *Kidney Int Suppl* 12: S82-89, 1982.
101. **Schnermann J, and Briggs JP**. Interaction between loop of Henle flow and arterial pressure as determinants of glomerular pressure. *Am J Physiol* 256: F421-429, 1989.
102. **Schnermann J, and Briggs JP**. Single nephron comparison of the effect of loop of Henle flow on filtration rate and pressure in control and angiotensin II-infused rats. *Miner Electrolyte Metab* 15: 103-107, 1989.
103. **Schnermann J, and Levine DZ**. Paracrine factors in tubuloglomerular feedback: adenosine, ATP, and nitric oxide. *Annu Rev Physiol* 65: 501-529, 2003.
104. **Schnermann J, Traynor T, Yang T, Arend L, Huang YG, Smart A, and Briggs JP**. Tubuloglomerular feedback: new concepts and developments. *Kidney Int Suppl* 67: S40-S45, 1998.
105. **Schnermann J, Traynor T, Yang T, Arend L, Huang YG, Smart A, and Briggs JP**. Tubuloglomerular feedback: new concepts and developments. *Kidney Int Suppl* 67: S40-45, 1998.
106. **Schwab K, Eiselt M, Schelenz C, and Witte H**. Time-variant parametric estimation of transient quadratic phase couplings during electroencephalographic burst activity. *Methods Inf Med* 44: 374-383, 2005.
107. **Sherwood L**. *Human physiology : from cells to systems*. Pacific Grove, Calif.: Brooks/Cole, 2001, p. xx, (various pagings).
108. **Shils JL, Litt M, Skolnick BE, and Stecker MM**. Bispectral analysis of visual interactions in humans. *Electroencephalogr Clin Neurophysiol* 98: 113-125, 1996.
109. **Shipley RE, and Study RS**. Changes in renal blood flow, extraction of inulin, glomerular filtration rate, tissue pressure and urine flow with acute alterations of renal artery blood pressure. *Am J Physiol* 167: 676-688, 1951.
110. **Silverthorn D**. *Human Physiology: An Integrated Approach*. Pearson Benjamin Cummings, 2007.
111. **Siu KL, Ahn JM, Ju K, Lee M, Shin K, and Chon KH**. Statistical approach to quantify the presence of phase coupling using the bispectrum. *IEEE Trans Biomed Eng* 55: 1512-1520, 2008.
112. **Skinner SL, McCubbin JW, and Page IH**. Angiotensin in Blood and Lymph Following Reduction in Renal Arterial Perfusion Pressure in Dogs. *Circ Res* 13: 336-345, 1963.
113. **Somlyo AP, and Somlyo AV**. Ca2+ sensitivity of smooth muscle and nonmuscle myosin II: modulated by G proteins, kinases, and myosin phosphatase. *Physiol Rev* 83: 1325-1358, 2003.
114. **Sorensen CM, Leyssac PP, Salomonsson M, Skott O, and Holstein-Rathlou NH**. ANG II-induced downregulation of RBF after a prolonged reduction of renal perfusion pressure is due to pre- and postglomerular constriction. *Am J Physiol Regul Integr Comp Physiol* 286: R865-873, 2004.
115. **Sorensen CM, Leyssac PP, Skott O, and Holstein-Rathlou NH**. Role of the renin-angiotensin system in regulation and autoregulation of renal blood flow. *Am J Physiol Regul Integr Comp Physiol* 279: R1017-1024, 2000.
116. **Sosnovtseva OV, Pavlov AN, Mosekilde E, Holstein-Rathlou NH, and Marsh DJ**. Double-wavelet approach to study frequency and amplitude modulation in renal autoregulation. *Phys Rev E Stat Nonlin Soft Matter Phys* 70: 031915, 2004.
117. **Sosnovtseva OV, Pavlov AN, Mosekilde E, Holstein-Rathlou NH, and Marsh DJ**. Double-wavelet approach to studying the modulation properties of nonstationary multimode dynamics. *Physiol Meas* 26: 351-362, 2005.

118. **Sosnovtseva OV, Pavlov AN, Mosekilde E, Yip KP, Holstein-Rathlou NH, and Marsh DJ**. Synchronization among mechanisms of renal autoregulation is reduced in hypertensive rats. *Am J Physiol Renal Physiol* 293: F1545-1555, 2007.
119. **Steinhausen M, Blum M, Fleming JT, Holz FG, Parekh N, and Wiegman DL**. Visualization of renal autoregulation in the split hydronephrotic kidney of rats. *Kidney Int* 35: 1151-1160, 1989.
120. **Takenaka T, Forster H, De Micheli A, and Epstein M**. Impaired myogenic responsiveness of renal microvessels in Dahl salt-sensitive rats. *Circ Res* 71: 471-480, 1992.
121. **Theiler J, Eubank S, Longtin A, Galdrikian B, and Farmer JD**. Testing for nonlinearity in time series: the method of surrogate data. In: *Interpretation of time series from nonlinear mechanical systems*. Warwick, United Kingdom: Elsevier North-Holland, Inc. New York, NY, USA, 1992, p. 77-94.
122. **Thomson S, Bao D, Deng A, and Vallon V**. Adenosine formed by 5'-nucleotidase mediates tubuloglomerular feedback. *J Clin Invest* 106: 289-298, 2000.
123. **Thurau K**. Renal Hemodynamics. *Am J Med* 36: 698-719, 1964.
124. **Tolins JP, Shultz P, and Raij L**. Mechanisms of hypertensive glomerular injury. *Am J Cardiol* 62: 54G-58G, 1988.
125. **Vallon V**. Tubuloglomerular feedback and the control of glomerular filtration rate. *News Physiol Sci* 18: 169-174, 2003.
126. **Vallon V**. Tubuloglomerular feedback in the kidney: insights from gene-targeted mice. *Pflugers Arch* 445: 470-476, 2003.
127. **Walker M, 3rd, Harrison-Bernard LM, Cook AK, and Navar LG**. Dynamic interaction between myogenic and TGF mechanisms in afferent arteriolar blood flow autoregulation. *Am J Physiol Renal Physiol* 279: F858-865, 2000.
128. **Wang H, Siu K, Ju K, and Chon KH**. A high resolution approach to estimating time-frequency spectra and their amplitudes. *Ann Biomed Eng* 34: 326-338, 2006.
129. **Wang H, Siu K, Ju K, Moore LC, and Chon KH**. Identification of transient renal autoregulatory mechanisms using time-frequency spectral techniques. *IEEE Trans Biomed Eng* 52: 1033-1039, 2005.
130. **Wang X, and Cupples WA**. Interaction between nitric oxide and renal myogenic autoregulation in normotensive and hypertensive rats. *Can J Physiol Pharmacol* 79: 238-245, 2001.
131. **Wang X, Loutzenhiser RD, and Cupples WA**. Frequency modulation of renal myogenic autoregulation by perfusion pressure. *Am J Physiol Regul Integr Comp Physiol* 293: R1199-1204, 2007.
132. **Wenzel RR**. Renal protection in hypertensive patients: selection of antihypertensive therapy. *Drugs* 65 Suppl 2: 29-39, 2005.
133. **Widman G, Schreiber T, Rehberg B, Hoeft A, and Elger CE**. Quantification of depth of anesthesia by nonlinear time series analysis of brain electrical activity. *Phys Rev E Stat Phys Plasmas Fluids Relat Interdiscip Topics* 62: 4898-4903, 2000.
134. **Wodey E, Tirel O, Bansard JY, Terrier A, Chanavaz C, Harris R, Ecoffey C, and Senhadji L**. Impact of age on both BIS values and EEG bispectrum during anaesthesia with sevoflurane in children. *Br J Anaesth* 94: 810-820, 2005.
135. **Wright FS, and Schnermann J**. Interference with feedback control of glomerular filtration rate by furosemide, triflocin, and cyanide. *J Clin Invest* 53: 1695-1708, 1974.
136. **Xia M, Li PL, and Li N**. Telemetric signal-driven servocontrol of renal perfusion pressure in acute and chronic rat experiments. *Am J Physiol Regul Integr Comp Physiol* 295: R1494-1501, 2008.

137. **Yip KP, Holstein-Rathlou NH, and Marsh DJ**. Chaos in blood flow control in genetic and renovascular hypertensive rats. *Am J Physiol* 261: F400-408, 1991.
138. **Yip KP, Holstein-Rathlou NH, and Marsh DJ**. Dynamics of TGF-initiated nephron-nephron interactions in normotensive rats and SHR. *Am J Physiol* 262: F980-988, 1992.
139. **Yip KP, Holstein-Rathlou NH, and Marsh DJ**. Mechanisms of temporal variation in single-nephron blood flow in rats. *Am J Physiol* 264: F427-434, 1993.
140. **Zar JH**. *Biostatistical analysis*. Upper Saddle River, N.J.: Prentice Hall, 1999, p. 1 v. (various pagings).
141. **Zhong Y, Bai Y, Yang B, Ju K, Shin K, Lee M, Jan KM, and Chon KH**. Autonomic nervous nonlinear interactions lead to frequency modulation between low- and high-frequency bands of the heart rate variability spectrum. *Am J Physiol Regul Integr Comp Physiol* 293: R1961-1968, 2007.